Quantifying microphone array directivity

The quantification and improvement of the acoustic camera of the TU Delft

S. Doljé

Technische Universiteit Delft

TU Delft Delft University of Technology

Challenge the future

QUANTIFYING MICROPHONE ARRAY DIRECTIVITY

THE QUANTIFICATION AND IMPROVEMENT OF THE ACOUSTIC CAMERA OF THE TU DELFT

by

S. Doljé

in partial fulfillment of the requirements for the degree of

Master of Science
in Aerospace Engineering

at the Delft University of Technology,
to be defended publicly on 22 December 2017.

Student number:	4142381	
Supervisor:	Dr. ir. M. Snellen	TU Delft
	ir. A. N. M. Malgoezar	TU Delft
Thesis committee:	Prof. dr. D. G. Simons	TU Delft
	Dr. ir. M. Snellen	TU Delft
	Ir. J. A. Melkert	TU Delft

An electronic version of this thesis is available at http://repository.tudelft.nl/.

TU Delft Delft University of Technology

SUMMARY

The growing demand of air travel results in an increase in flights and thus an increase in noise pollution. Solutions for decreasing this noise pollution can be designed, but it requires data on the strength and position of the noise sources on the aircraft. An acoustic camera is a device which can identify and visualise these aircraft noise sources. The performance of the acoustic camera must be quantified after which it can be optimised to have the most accurate mapping of the noise sources. The quantification and optimisation are the focus of this research. The research is carried out at the Aircraft Noise and Climate Effects (ANCE) section of the TU Delft and can be divided in three parts: the quantification, optimisation and verification. The main goal of the research is to gain more information on the acoustic camera of the ANCE section and design and build an optimised acoustic camera which can be used for fly-over measurements.

The quantification starts with measurements at the anechoic chamber of the TU Delft. The directivity performance of an acoustic camera is examined by placing a sound source under specified angles. Preferably there is no effect of the location of the sound source relative to the array on the estimates obtained on source position and source strength. However, measuring the sound under an angle resulted in a position deviation in the source plots. More accurate position readings could be achieved by adapting the weight factor used for beamforming. The sound pressure level (SPL) also deviated with increasing measurement angle. However, no correlation could be found between the change in SPL and measurement angle. As a next step, focus was on the development of a new acoustic camera for fly-over measurements. In order to resolve also for small aircraft (B737) between the main landing gear and the engines, an aperture of 3.4 m was selected. The reflection of sound on the ground was given particular attention to avoid effects from this phenomenon in the optimised design. First, the possibility of sound waves passing through the construction and influencing the measurement results is examined. It appeared only low frequencies could penetrate the construction for the lay-out selected in the past and the influence on the measurements was minimal. Further investigation on the influence of the ground effect was carried out through a spectrogram analysis using data of a Boeing B737 measured with the previous fly-over camera. Fringes of Lloyd's mirror reflection are present in the spectrograms. These fringes are not equal for all microphones, but are dependent on the microphone position in the construction and the flight direction of the aircraft. The microphones positioned near the edge of the array and in the flight direction were found to be affected most. It was concluded that this is due to edge diffraction and can be avoided by placing the microphones at least 30 cm from the edge.

The optimisation of the camera starts with a decision on the general lay-out of the acoustic camera. Three common configurations used for fly-over measurements are considered. After a trade-off, the configuration with all microphones attached to a plate is chosen as the best configuration to use, due to the low costs, good manufacturability and high microphone position accuracy. The microphone array of the optimised design is the Underbrink spiral array, due to its good overall performances which are required when measuring fly-over aircraft. The array contains 64 microphones, placed in an 8-arm configuration, with an aperture of 3.4 m. The aperture is doubled with respect to a previous camera to obtain an increase in resolution. The microphones are placed 30 cm from the edge to avoid interference of the edge diffracted sound waves. The construction must be at least 4 x 4 m to be able to fit an array with these specifications. It is divided in 16 plates of 1 x 1 m to keep it easy to handle and transport. The big plates are attached through support plates with bolts and winged nuts. Adjustable legs are placed below the support plates to make sure the camera can be set level. The main plates are made out of multiplex with Flamex GU foam placed on top to absorb reflections and decrease the signal interference. Clothes pins are used to clip the microphones and assure their exact positioning. A structure holding the optical camera is made in the middle of the acoustic camera to obtain clear images required for the data analysis. Rough foam is placed over the microphones to serve as wind shield.

The optimised acoustic camera was built and verified with fly-over aircraft at Schiphol Airport. Aircraft flyovers were recorded for three days, resulting in 161 measurements. Information on the fly-over aircraft was obtained through an ADS-B receiver and verified with the optical camera. The measured data was corrected for background noise, the effects of forward motion, the Doppler effect and the atmospheric effects.

When evaluating the ground effect, it became apparent that the fringes of Lloyd's mirror reflection were not detectable. This means that the interference of the edge diffraction is resolved by placing the microphones at least 30 cm from the edge. Another point of improvement was the resolution. A comparison in beamform plots, made with the previous and the optimised acoustic camera, shows an increase in resolution due to the increased aperture of the array. The engines and main landing gear could now be distinguished for all aircraft.

The goal of the research is achieved by the quantification of the directivity performance and the optimisation of the previous acoustic camera. The accuracy of the microphone positions is increased by using a rigid structure, clamping the microphones and using adjustable legs. The resolution is improved by doubling the aperture of the array. Lloyd's mirror reflection caused by edge diffraction is solved by placing the microphones at least 30 cm from the edge.

PREFACE

During my studies at aerospace engineering, I never was the specialist. I liked the broad study program and wanted to know something about all aspects in the aircraft industry. The whole world was at my feet due to the general knowledge gained in design strategies, complicated mathematics and optimisations. I liked testing the boundaries and applying my knowledge not only to the field of aerospace engineering but also by designing a (flying) car during my bachelor thesis and a sailing yacht in my minor. For my master thesis I wanted something besides a detailed optimisation and more than sitting at my desk the whole year. Going through various thesis subjects I stumbled upon the footprint of an aircraft. During my masters I had already chosen courses on aircraft noise and emissions to broaden my view on aircraft design. I really enjoyed this and when hearing about a thesis on aircraft noise combined with outdoor experiments, I needed to know more. In the end I started a thesis about the noise mapping of Teuge Airport. Unfortunately there were some miscommunications between the municipality, which had hired me, and the airport. This eventually resulted in a full stop of my thesis. Luckily Mirjam Snellen and Dick Simons quickly helped me out and proposed another thesis on aircraft noise combined with experiments. This was the master thesis presented in this report: The quantification and improvement of the acoustic camera of the TU Delft.

During my thesis there were plenty of difficulties, as always with large projects. Many people helped me through the whole process, till the point I can proudly present my research. In this section I would like to thank all the people that helped with the creation of this research. First of all I would like to thank Mirjam Snellen and Anwar Malgoezar. They were the main supervisors of my project and helped me with my daily problems. Furthermore I would like to thank Dick Simons, which is the head of the department and who gave detailed feedback at the main meetings to improve the overall research. Within the department I would also like to thank Roberto Merino-Martinez and Ana Alves Vieira, who helped out on specified areas when needed. I needed to work with an ADS-B system for the fly-over measurements, of which was no knowledge within the department. Luckily, Junzi Sun provided me with the programs and helped with the installation and data conversion. Apart from help on the content of the research, there were people who helped with more organisational issues. Special thanks have to go to Lisette Vollmer who, as secretary of the department, helped with all required documents, declarations and equipment and room issues. Last but not least I would like to thank my boyfriend and all my friends and family to give support, distractions and encouragements during the complete process.

S. Doljé
Delft, December 4, 2017

Contents

List of Figures

List of Tables

NOMENCLATURE

ACRONYMS

ADS-B	Automatic Dependent Surveillance Broadcast
ANCE	Aircraft Noise and Climate Effects
B & K	Brüel and Kjaer
DAQ	Data Acquisition System
DSE	Design Synthesis Exercise
FLTR	From Left To Right
ICAO	International Civil Aviation Organization
ILS	Instrumentation Landing System
ISO	International Organization for Standardization
KNMI	Royal Netherlands Meteorological Institute
Max	Maximum
Mic	Microphone
NASA	National Aeronautics and Space Administration
NLR	National Aerospace Laboratory
OSPL	Overall Sound Pressure Level
PSD	Power Spectral Density
SPL	Sound Pressure Level
TU Delft	Delft University of Technology

LATIN SYMBOLS

A	Source auto power	Pa^2
Ac	Intrinsic parameter matrix	-
a	Complex source amplitude	-
b	Width	m
C	Covariance matrix	Pa^2
c	Speed of sound	m/s
D	Diameter	m
d	Thickness	m
dl	Distance between the aircraft when overhead and when the sound is received	m
dr	Distance between the aircraft when overhead and when the sound is emitted	m
dt	Time span	sec
dX	Pixel to meter ratio in the x-direction	-
dY	Pixel to meter ratio in the y-direction	-
E	Young's modulus	N/m^2
F	Scaled frequency	Hz/Pa
$F_{r,N}$	Scaled relaxation frequency of Nitrogen	Hz/Pa
$F_{r,O}$	Scaled relaxation frequency of Oxygen	Hz/Pa
FL	Focal length	pixels
f	(Observed) Frequency	Hz
f'	Emitted frequency	Hz
g_j	Steering vector	m^{-1}
H	Height of the aircraft with respect to the ground	m
h	Height of the aircraft with respect to the microphone array	m
h_m	Height of the microphones	m
J	Objection function	-

K	Constant	-
k	Wave number	rad/m
L	Humidity	%
L_r	Relative humidity	%
l	Length	m
M	Mach number	-
N	Number of microphones	-
N_a	Number of spiral arms	-
N_m	Number of microphones per spiral	Pa
p	Pressure	Pa
p_s	Atmospheric pressure	Pa
p_{sat}	Saturated vapour pressure	Pa
PSD	Power Spectral Density	Pa^2/Hz
Q_p	Plane wave reflection coefficient	-
R	Rayleigh criterion	m
Rd	Radius	m
r	Distance from microphone to the source	m
$r_{j,0}$	Distance from the mid of the array to the grid point	m
$r_{j,n}$	Distance from the microphone to the grid point	m
r_e	Distance from microphone to the source when the sound is emitted	m
s	Mass per unit area	kg/m^2
SPL	Sound pressure level	dB
ΔSPL	Difference in Sound Pressure Level	dB
T	Temperature	K
TC	Transmission coefficient	-
TL	Transmission loss	dB
t_e	Time at which the sound is emitted	sec
t_o	Time at which the aircraft is overhead	sec
t_r	Time at which the sound is received	sec
$\Delta t_{j,n}$	Time delay	sec.
u_0	1st coordinate of the principal point	pixels
v_0	2nd coordinate of the principal point	pixels
V	Velocity	m/s
w_j	Weight vector	m^{-1}
x_0	Initial position vector	m
x_n	Distance from the microphone to the reference system	m
x_r	Distance from microphone to the source when the sound is received	m
Z_n	Normal surface impedance	$N \cdot s/m^3$

GREEK SYMBOLS

α	Sound attenuation coefficient	dB/m
β	Prandtl-Glauert compressibility correction factor	-
γ	Skew coefficient	-
δ_{max}	Maximum deflection	m
η	Phase change	-
θ	Angle between the flight path of the aircraft and the direct path of the sound	rad
θ_s	Steering angle	rad
θ_b	Beam width	rad
λ	Wavelength	m
μ	Angle of the microphones w.r.t the middle of the array	rad
ν	Spiral angle	rad
ξ_j	Distance from the reference system to the grid point	m
ρ	Density	kg/m^3
σ	Flow resistivity	$kPa \cdot s/m^2$
ϕ	Angular distance of the Rayleigh limit	rad
ψ	Incidence angle of the reflected sound	rad
ω	Angular velocity	rad/sec

1

INTRODUCTION

In today's society, people are more and more aware of the impact they are causing on their environment. To maximize the living comfort, this impact should be minimal. The aircraft industry is an industry which has a large impact on its environment. Not only in the sense of air pollution, but also by creating noise. Solutions for decreasing this noise pollution can be designed, but it requires data on the source strength and the position of the sound sources on the aircraft. Acoustic cameras and beamforming algorithms are powerful tools for identifying noise sources on an aircraft. One characteristic of acoustic cameras is their capability to estimate the levels of individual sound sources contributing to the total sound level. Its performance is however dependent on the cameras geometry. For example, by putting the microphones on a hard plate, the pressures of the microphones will double due to the constructive interference of the direct signal and the reflected signal. In addition, the sides of the plate result in diffracted waves that can affect the measurements. As a result, sound sources could be presented with a different sound pressure level or placed at the incorrect position. The performance of an acoustic camera has to be quantified to make sure the noise measurements give accurate results. This is done in a research with the research objective: To design an acoustic camera and quantify its performance by the use of controlled and outdoor measurements.

The research is carried out in the ANCE (Aircraft Noise and Climate Effects) section of the TU Delft. The main goal is to build an optimised camera which can be used for fly-over measurements. It is important to know what knowledge on the subject is already available to avoid re-inventing the wheel. An in depth literature research is carried out, of which the most important information is presented in Chapter 2. A gap in the research field is determined from this study and used as a focus for the research presented in this report. The main area of interest is within the optimisation of the acoustic camera. Many papers have been written on the data-analysis and the array configuration. However, the construction holding the microphones is taken for granted. This means the optimization of the construction will be an area of interest. Apart from the construction, information is missing on the angle of the sound source and its effect on the recorded data. This gives the influence of the angle between the sound source and the array as another area of interest. Next to the general knowledge, the TU Delft likes to have an optimised acoustic camera for fly-over measurements.

1.1. RESEARCH OBJECTIVE AND QUESTIONS

With the defined area of interest, a research objective can be determined. This objective is: To design an acoustic camera and quantify its performance by the use of controlled and outdoor measurements. The main research question follows from the objective: What is the performance of the current acoustic camera used by the TU Delft and how can it be improved?

To be able to answer the main research question, the research can be divided into three parts with their own sub-questions displayed in Table 1.1. By going through the three parts, the sub-questions will be answered, which eventually results in an answer to the main research question. The parts are defined as follows:

- Quantification: The project starts with gathering information on the current situation specified to the directivity of an acoustic camera. Directivity is the sensitivity of the array to the resolution precision of the sound source measurements focussed on sources directly overhead the camera. However, it is of interest to know how sensitive the camera is to the relative source position, e.g. when studying the

directionality of the aircraft noise sources. The quantification is carried out through measurements in a controlled environment. Furthermore, knowledge on the previous fly-over camera is gathered and its performance is examined.

- Optimization: The directivity performance and insights in the performance of the previous fly-over camera are used to design an optimised acoustic camera. For the optimization, it is convenient to know more about configurations used in the past, material performances and the influence of the microphone array. Parts of the optimized design will be tested in a controlled environment for verification. A detailed design can be made with all this knowledge.
- Verification: The optimised design of the acoustic camera will be built and tested on fly-overs of aircraft with an outdoor measurement campaign at Schiphol Airport. To know what results to expect, preliminary knowledge on aircraft noise sources is required.

Table 1.1: The main goals and sub-questions of the MSc thesis

Goals	**Sub-questions**
Quantification	1. What are the current measurement difficulties of acoustic cameras with respect to their directivity performance? 2. What is the quantification of the TU Delft acoustic camera directivity performance in a controlled environment? 3. What are the main disadvantages of the previous fly-over camera?
Optimization	4. What are the different constructions for acoustic cameras used in the past? 5. What is the effect of the materials selected on the performance of the acoustic camera? 6. What is the influence of the microphone array on the measurement results? 7. What is the best design for the optimised acoustic camera used for fly-over measurements?
Verification	8. What are the most common noise sources of a modern-day aircraft? 9. What is the performance of the optimized acoustic camera for fly-over measurements?

1.2. METHODOLOGY AND REPORT OUTLINE

The research begins with a literature study, from which the most important results are presented in Chapter 2. It is a desk research and performed to get insight in the research field. The chapter contains information on the acoustic camera, the data analysis method, the microphone array, edge diffraction, the ground effect and the main noise sources of an aircraft. After the literature study, the acoustic camera used by the TU Delft is quantified. The quantification is carried out through experimental research in a controlled environment. The controlled environment is the anechoic chamber of the TU Delft. During the experiment a sound source is placed under an angle to be able to check the array directivity. The experiment is described in Chapter 3. The data obtained is analysed to investigate the microphone performance and the estimation of the strength and position of the sound source in Chapter 4. Chapter 5 presents information on the previous fly-over camera with emphasis on its flaws. The information is gathered from the design report of the camera [31], a conversation with one of the designers and a research on the ground effect. With the gathered information, an improved version of the acoustic camera is designed, which is described in Chapter 6. A trade-off for the general configuration is made, a microphone array is chosen and the detailed design is presented with information on the material properties and construction decisions. Having a clear picture on the new design, the optimised acoustic camera can be built. An outdoor measurement campaign is carried out to verify the optimised camera. The campaign is performed at Schiphol Airport and data is collected on the noise of landing aircraft. The complete experiment with information on the location, equipment, aircraft information and the measurements itself is described in Chapter 7. The data obtained is corrected for background noise, the effects of forward motion, the Doppler effect and atmospheric effects as described in Chapter 8. The corrections are paired with a spectrogram analysis on the ground effect. Chapter 9 gives a beamform analysis with emphasis on the resolution of the acoustic camera. The report closes with conclusions on the complete research and recommendations for future research in Chapter 10.

2

RELEVANT RESEARCH

This chapter presents relevant knowledge required for the research described in this report. It starts with a short explanation on acoustic cameras in Section 2.1. Next, the data processing method beamforming is explained in Section 2.2. Section 2.3 gives information about microphone arrays including its configuration, the aperture and the influence of the amount of microphones. After this, two characteristics of sound waves are presented. The edge diffraction in Section 2.4 and the ground effect in Section 2.5. The chapter ends with information on general aircraft noise sources in Section 2.6.

2.1. ACOUSTIC CAMERA

An acoustic camera is an imaging device which can locate and visualize noise sources. It consists out of a group of microphones and therefore it is also called a microphone array. The array captures the sound which can be analysed through beamforming algorithms to get a mapping of the noise sources. A picture of an example configuration of an acoustic camera is shown in Figure 2.1. The microphones are placed in a certain configuration with the help of any kind of construction. The microphones record the sound waves and pass them through to a data acquisition system. This system samples and converts the data, so it can be manipulated by a computer. [1] The data acquisition system is wired to a computer which contains a software program to control the devices, show the incoming data real time and save the data files. External sensors can be added to the configuration for a smoother data analysis. An optical camera can for instance be used to record images, which can be coupled to the sound files to visualise the noise sources on the aircraft.

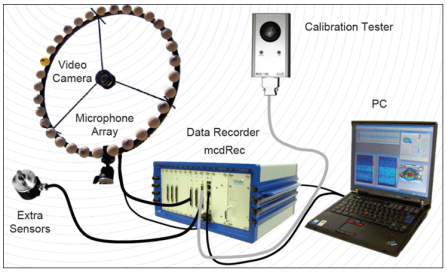

Figure 2.1: An acoustic camera configuration [2]

2.2. BEAMFORMING

Beamforming is a signal processing technique for directional signal transmission or reception [3]. Each microphone in the array receives a specific sound at a specific time. To focus on a certain direction, the sound at a part of the microphones needs to be delayed. This is visualized in Figure 2.2 where a wave front of sound hits two microphones of one array at different moments in time. If the signals at the two receivers are summed, the travel time differences between the source and the two receivers will result in a sum of two signals which are shifted in time relative to each other. Delaying the signal from the lower microphone, such that the delay corrects for the difference in travel time, and adding the two resulting signals will result in complete constructive interference and therefore maximum output. In general a focus plane consisting of all potential source

locations is generated to get an acoustic image. By knowing the speed of sound and the distance of each microphone in the array to the focus plane, the time delays can be determined. When all signals are shifted such to obtain constructive interference for the scan points considered, they can be added and averaged to obtain one signal. Figure 2.3 shows in a schematic way how the individual signals of each microphone are delayed/shifted, summed and averaged over the number of microphones used [5]. This method is called Delay-and-Sum beamforming.

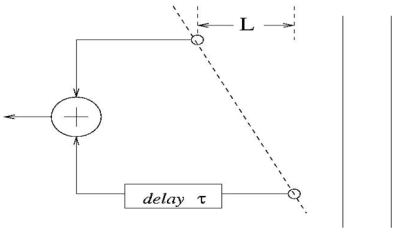

Figure 2.2: A wave front of sound approaching a microphone array [4]

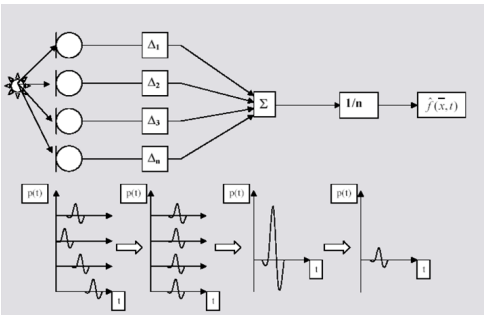

Figure 2.3: An overview of Delay-and-Sum beamforming [5]

2.2.1. CONVENTIONAL BEAMFORMING

Beamforming on fly-over measurements is usually carried out in the frequency domain. In this subsection a description is given to get from sampled microphone data to an acoustic image by means of conventional beamforming. The equations given are obtained from Reference [4] and [6].

A microphone array with N microphones is considered. The pressures as received by each microphone are Fourier transformed to get an N-dimensional vector $\vec{p}$ as displayed in Equation 2.1.

$$\vec{p}(f) = \begin{pmatrix} p_1(f) \\ : \\ p_N(f) \end{pmatrix} \tag{2.1}$$

Steering vectors represent the model for the received pressures at the N microphones for a source at the j^{th} potential source location [4]. For a moving source this gives Equation 2.2 for the n^{th} element of the steering vector. In this equation the Mach number can be computed as $\vec{M} = \frac{\vec{V}}{c}$ and the distance from the microphone to the grid point is $r_{j,n} = || \vec{x}_n - \vec{\xi}_j ||$. The distance is visualised in Figure 2.4. The time delay can be calculated with Equation 2.3 in which $\beta = \sqrt{1 - || \vec{M} ||^2}$.

$$\vec{g}_{j,n} = \frac{-exp(-2\pi i f \Delta \vec{t}_{j,n})}{4\pi r_{j,n}(1 - || \vec{M} || cos\theta_s)^2} \tag{2.2}$$

$$\Delta \vec{t}_{j,n} = \frac{-\vec{M} \cdot (\vec{x}_n - \vec{\xi}_j) + \sqrt{(\vec{M} \cdot (\vec{x}_n - \vec{\xi}_j))^2 + \beta^2 || \vec{x}_n - \vec{\xi}_j ||^2}}{c\beta^2} \tag{2.3}$$

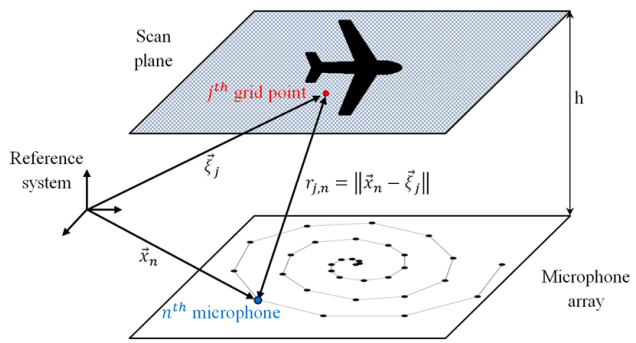

Figure 2.4: Schematic of the distances between microphones and scan plane [4]

The purpose of beamforming is to determine complex amplitudes (a_j) of sources in $\vec{\xi}_j$. This can be achieved by comparing the measured vector $\vec{p}$ with the steering vector $\vec{g_j}$, for instance through minimisation of $J = || \vec{p} - \vec{g_j} a_j ||^2$. Applying the least-squares minimization gives the source auto power: $A = \frac{1}{2} || a_j ||^2$. This can be rewritten as shown in Equation 2.4, with the weight vector $\vec{w}_j$ and the covariance matrix $\vec{C}$ given in Equation 2.5 and 2.6. Equation 2.4 is known as 'Conventional beamforming' and plotting the source auto power as a function of grid position gives the acoustic image.

$$A(\vec{\xi}_j) = \frac{1}{2} \frac{\vec{g}_j^* \vec{p} \vec{p}^* \vec{g}_j}{|| \vec{g}_j ||^4} = \vec{w}_j^* \vec{C} \vec{w}_j \tag{2.4}$$

$$\vec{w}_j = \frac{\vec{g}_j}{\vec{g}_j \vec{g}_j^*} = \frac{\vec{g}_j}{|| \vec{g}_j ||^2} \tag{2.5}$$

$$\vec{C} = \frac{1}{2} \vec{p} \vec{p}^* \tag{2.6}$$

2.3. MICROPHONE ARRAY

The microphone array has a large influence on the measurement results and the eventual beamform pictures. In general, any planar array can be described by the number of microphones, the aperture and the pattern of the arrangement [7]. To be able to choose an optimal array design these parameters are researched and discussed in the sections below.

2.3.1. ARRAY CONFIGURATION

The most popular array configurations are the traditional, the spiral and the random arrays. Two well-known traditional array configurations are the grid and the circle array, which have a regular spacing between their microphones. However, they display many side lobes. When beamforming is applied to a traditional array, side- and grating lobes may show up in the source map as false sources, so called ghost images [8]. The higher the level of the lobes, the harder it is to distinguish the real from the false sources. Grating lobes are a sort of side lobes which appear in a uniformly spaced array when the microphone spacing is greater than a half wavelength. The grating lobes have a larger amplitude then the side lobes and approach the level of the main lobe. Figure 2.5 displays two traditional arrays with their beamform plots. The beamform plots are of the same source, but the images are different. This shows that the array configuration has a big influence on the eventual beamform picture. However, none of them display a clean source without lobes. Reference [9] explains that this is due to the regular spacing of the traditional arrays, which results in spatial aliasing. To diminish spatial aliasing irregular microphone spacing can be used, as is the case for most spiral arrays.

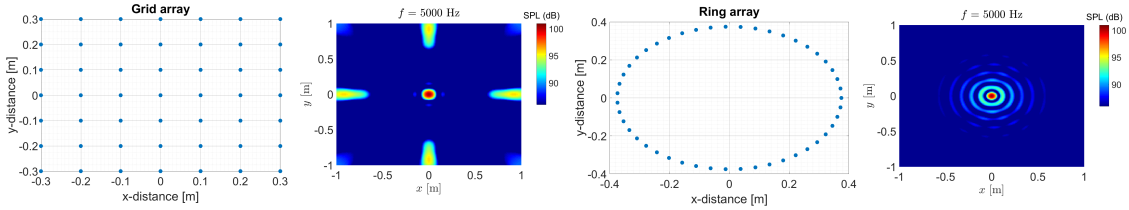

Figure 2.5: Two traditional array configurations with their beamform plots [10]

Microphone arrays with a spiral configuration have lower side lobe levels than the traditional configuration [7–13]. Six popular spiral designs are the Archimedean spiral, the Dougherty log-spiral, the Arcondoulis spiral, the Multi-spiral, the Underbrink array and the Brüel and Kjaer style array. All configurations are displayed in Figure 2.6. These spirals are compared for far-field (planar propagation) and near-field (spherical propagation) performances in Reference [9]. When a beamforming array is used with a near-field source, such that the pressure waves propagate spherically, the evaluation of the array performance is less general, and must be performed at the expected array operating conditions [9]. For the far-field measurements, the Underbrink and B&K array had the best resolution and the single spiral designs the worst. The lowest side lobe levels were obtained with the Multi-spiral, Underbrink and Arcondoulis array. For the near-field measurements the Underbrink and B&K array had again the best resolution. The results for the minimum side lobe level are highly dependent on the position of the sound source. This dependency is due to the distri-

bution of the microphones over the array. The single-arm arrays most often have more microphones placed close to the origin of the array resulting in lower side lobe levels if the source is at the origin. However the multi-arm spirals have a more evenly distribution, giving better performances over a large area. This makes that the Underbrink and the Multi-spiral design have the lowest overall side lobe level. The best array for all-around performances is the Underbrink spiral array [9].

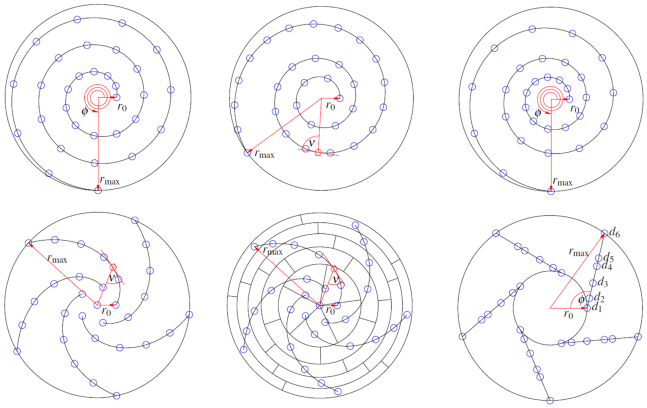

Figure 2.6: Spiral array configurations (from left to right): the Archimedean spiral, the Dougherty log-spiral, the Arcondoulis spiral, the Multi-spiral, the Underbrink array and the Brüel and Kjaer style array [9]

Apart from the spiral arrays, random arrays are popular non-redundant arrays. Their irregular (non-redundant) geometry outperforms the traditional regular array designs [8]. To have a random array with excellent performances, the spacing between all microphones needs to be optimised. If the random array is not optimised, the performance with regards to side lobe can be worse than the traditional configurations [11, 13]. A random optimised array most often performs as good or even better than a spiral array configuration [7, 8]. A disadvantage of the random array is the more difficult manufacturing process and operation due to its complicated geometry. Its optimisation is numerically demanding because of the large number of free variables. [8] An array optimisation performed in Reference [14] shows a correlation between the microphone spacing, the side lobe levels and the width of the main lobe. When the microphones are distributed at a sparse part of the array, the width of the main lobe will increase. Another correlation was found between the microphone distance and the frequency. The distance between the microphones decreases with increasing frequency in almost a linear way to have the least amount of side lobes. For an optimum design a compromise has to be made between the beam width of the main lobe and the number of side lobes. This results in an optimised array configuration with a regular behaviour and with the microphones distributed at almost constant distance as displayed in Figure 2.7. However, the regular pattern gives rise to side lobes. This indicates the need for small variations of the microphone distances [14].

An optimized array has the best performance. However this is often only for certain demands. The optimal array design depends on parameters like the investigated noise frequencies, the size of the investigated area, the dimensions of the array, the distance to the noise source, the distance in between the investigated noise sources, the maximum allowable side lobe level and the budget [15]. If an array configuration with a good overall performance is required it is best to use a spiral array instead of a specified random array.

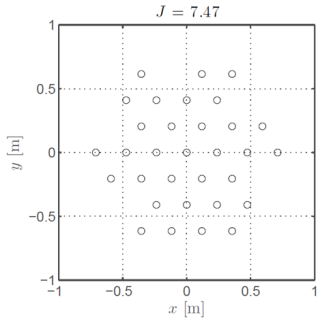

Figure 2.7: A hexagonal configuration obtained by optimizing the objective function of Reference [14]

2.3.2. APERTURE

The aperture of the microphone array determines the lowest frequency at which the array is effective and the resolution which can be measured. To have an idea about resolution, the Rayleigh (diffraction) limit can be used [4]. This Rayleigh criterion (R) is the minimum angular distance (ϕ) at which two different sources can still be distinguished as separate sources, using a circular aperture. The criterion is based on the diffraction of waves by the finite aperture and is given by Equation 2.7, with h as the altitude of the aircraft with respect to the microphone array and $\phi = 1.22\frac{\lambda}{D} = 1.22\frac{c}{fD}$. Figure 2.8 shows a schematic picture of the scan plane and the microphone array and an indication of the Rayleigh criterion.

$$R = h \cdot tan\phi \tag{2.7}$$

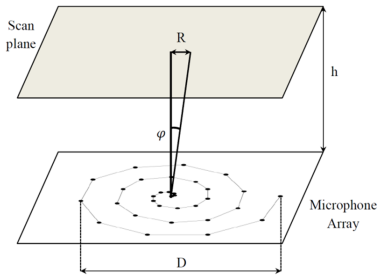

Figure 2.8: A schematic picture explaining the Rayleigh criterion [4]

A larger aperture (D) or a smaller distance between the array and the scan plane (h) results in an increase in resolution. This means the best resolution will be obtained if the distance to the source over the aperture (h/D) is the smallest [16]. When the distance to the source is large, a big aperture can resolve sources down to a low frequency and improves the resolution. However, when using the same large aperture for sources nearby, it will result in a narrow source width at a given frequency. This means the grid points used for beamforming need to be denser to find the wanted noise sources, or if possible a smaller scan grid can be used. When a denser grid has to be used, it will result in increased processing time, so a balance is required. [16] The budget, manufacturing and the operation of the array have to be kept in mind. The larger the aperture, the more difficult it would be to transport, set-up and manufacture and thus the higher the costs. This means the aperture of the microphone array must be adapted to the demands of the experiment.

2.3.3. NUMBER OF MICROPHONES

The number of microphones used in an array is dependent on various parameters. In general it can be said that the more microphones used, the better the beamforming pictures will be [5, 9, 12, 14]. However, more microphones will also result in higher costs. An optimisation for the amount of microphones is often made to avoid this. Another factor influencing the number of microphones is the data-acquisition system. The system has a certain amount of input channels, limiting the amount of microphones which can be used [16]. The array configuration also influences the number of microphones. The maximum side lobe level can be decreased by increasing the amount of microphones or by optimising the array configuration [7]. This means that an optimised array configuration can make the same beamform picture as a non-optimised array with extra microphones. There is no perfect amount of microphones to use, this is dependent on the application.

2.4. EDGE DIFFRACTION

When a sound wave passes an obstacle it will be diffracted as is displayed in Figure 2.9. The properties of the wave stay the same, only the direction changes [17]. When a sound source is placed directly in front of the acoustic camera the sound wave will directly be measured by the microphones without the wave being diffracted. However, when measuring a sound source under an angle, the wave will change its path when hitting the edge of the plate. This change in path of the sound wave can influence the measurement data. The waves will diffract after hitting the edge according to the Huygens-Fresnel principle [2]. The extent of diffraction depends on the side of the object relative to the wavelength. The longer the wavelength (the lower the frequency) compared to the width of the edge, the more the wave spreads out after hitting the edge. This is displayed in Figure 2.10. The arrows in the figure give an indication of the path of a sound wave of various frequencies when hitting an edge.

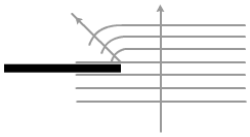

Figure 2.9: Diffraction of a wave caused by passing an edge [17]

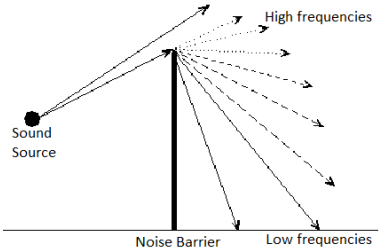

Figure 2.10: Diffraction around an edge for different frequencies [17]

2.5. GROUND EFFECT

Sound emitted from a source will be transmitted to a receiver in a direct and an indirect way. When a sound wave goes straight from the source to the receiver, this is called the direct path. For the indirect path, the sound wave leaves sound source, reflects off a surface, and then arrives at the receiver. This is visualised in Figure 2.11. During the reflection, part of the sound will be absorbed depending on the type of surface. Soft surfaces have relatively low impedance, which leads to a high ground attenuation. Hard surfaces have high impedance and will reflect most of the signal. The reflectivity of surfaces can be calculated with the Delany and Bazley model [2, 19]. Within this model the plane wave reflection coefficient is calculated with Equation 2.8, in which $\frac{Z_n}{\rho_\infty c}$ is the specific surface impedance, ψ the incidence angle of the reflected sound with the ground surface and η is the phase change [2, 19].

$$Q_p = |Q_p|e^{i\eta} = \frac{\frac{Z_n}{\rho_\infty c} sin\psi - 1}{\frac{Z_n}{\rho_\infty c} sin\psi + 1} \tag{2.8}$$

The specific surface impedance can be calculated with Equation 2.9 and is dependent on the frequency and the flow resistivity of the ground material [2, 19].

$$\frac{Z_n}{\rho_\infty c} = [1 + 9.08(\frac{f}{\sigma})^{-0.75}] + i[11.9(\frac{f}{\sigma})^{-0.73}] \tag{2.9}$$

Due to the ground reflection, the sound pressure level measured near the ground will be different than the sound pressure level which would occur in the free field. This difference is called the ground effect [19]. The receiver picks up a direct and an indirect sound wave with different path lengths. This path length difference will result in a phase shift and thus constructive and destructive interference of both sound signals. The sound level at the receiver will be increased by maximum 6 dB. In this case the sound pressure is doubled and the receiver sees two sources, the actual source and a reflected source [20]. Constructive interference of the direct and indirect signal is dependent on the frequency and geometry and is visible in a spectrogram by parabolic lines (Figure 2.12). These parabolic lines are called Lloyd's mirror reflection. The frequencies at which the signal is reinforced ($f_{reinforce}$) and cancelled (f_{cancel}) can be calculated with Equations 2.10 and 2.11 in which K is a constant representing $K = 0, 1, 2, 3, ...$, h_m is the height of the microphone, c the speed of sound and ψ the incidence angle of the reflected sound with the ground surface.

$$f_{reinforce} = \frac{cK}{2h_m sin\psi} \tag{2.10}$$

$$f_{cancel} = \frac{c(K+0.5)}{2h_m sin\psi} \tag{2.11}$$

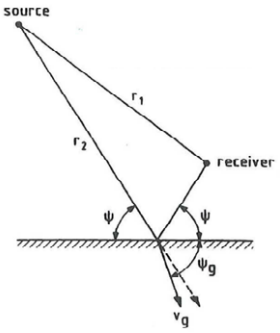

Figure 2.11: Ground reflection [2]

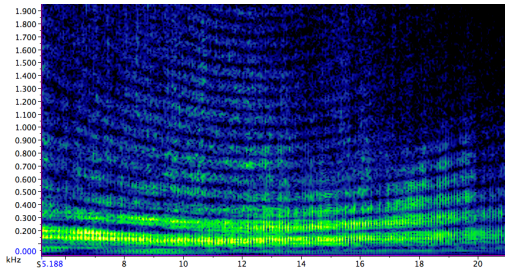

Figure 2.12: Constructive acoustic interference in the spectrogram of a Chinook recording [21]

The height of the receiver influences Lloyd's mirror reflection . When the distance between the receiver and the ground is lowered, the location of the first cancellation is moved to higher frequencies. Moving the receiver away from the ground moves the location of the first cancellation to lower frequencies [22, 23]. This effect is visualised in Figure 2.13 for a microphone height of 0.1 m and 0.3 m.

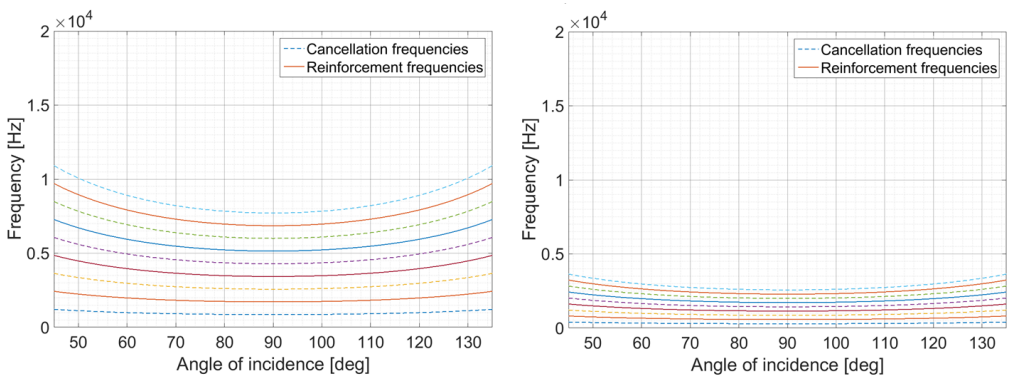

Figure 2.13: Theoretical ground interference for a microphone at a height of 0.1 m (left) and 0.3 m (right)

To avoid the ground interference effects in the noise spectra, the microphones should be placed at ground level. This way the direct and the reflected waves have the same path length and will arrive in phase for all frequencies. The sound pressure measured will be twice as high as the free field measurements and can be corrected by subtracting 6 dB for all frequencies [23, 24]. Flush mounted microphones can be used to obtain this condition, but they can be difficult to install. For this reason three other configurations with the microphone placed close to the ground are examined. These are the inverted, horizontal mounted and surface microphones and are displayed in Figure 2.14.

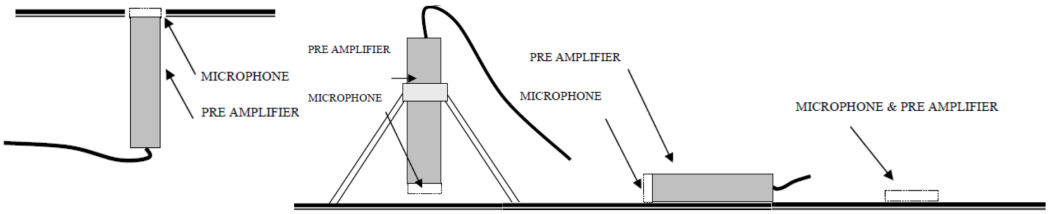

Figure 2.14: Near ground microphone configurations. FLTR: Flush mounted, inverted, horizontal mounted and surface microphone [24]

The inverted microphone can be placed with varying height to the ground. According to Reference [25] the inverted microphone shows the most resemblance with the flush mounted microphone at a height of 0.5 times the diameter of the microphone. According to the experiment in Reference [25], it is in good agreement with the flush mounted microphone till 4 kHz. Above this frequency there are systematic deviations due to the interference of the direct and indirect sound waves. In the research of Reference [23] it was found that the direct and reflected waves are almost in phase at low and mid frequencies, but deviate at the higher frequencies. The horizontal mounted microphones react approximately the same as the inverted microphones [23, 25].

The surface microphone is a microphone placed on a ground plate. The size and model of this ground plate can deviate. Research of NLR [24] mentions that the signals will arrive in phase (have a 6 dB increase) when a large ground plate is used (D=3 m). When the microphone is placed on a smaller ground plate (D=0.4 m), there is no optimal pressure doubling. Reference [23] uses a circular flush disk of 1.524 m to hold the microphone. This configuration was found to be free from ground effects, except for angles within 15 degrees of the overhead position (in between the red solid lines of Figure). In this region there is an interaction between direct and edge diffracted waves. Reference [25] also measures a 6 dB increase for all incidence angles, except for angles within 20 degrees of the overhead position (in between the blue striped lines of Figure). For these angles, deviations caused by the diffraction of the sound field by the plate are observed. To avoid this edge diffraction, the edges should be shaped to match the impedance between the dish and the ground gradually [23]. When this is done in a right way, the measurements should be free from ground effects and edge diffrac-

tion. The benefit of this configuration over the flush mounted microphones is the easy installation and the fact that it can be placed on a hard surface and natural terrain [23].

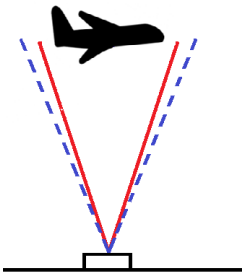

Figure 2.15: Aircraft overhead the microphone array with indication of 15 (red solid lines) and 20 (blue striped lines) degrees within the overhead position

2.6. AIRCRAFT NOISE

When operating an aircraft there are different flight phases, depending on its mission. The typical mission profile of a transport aircraft has three flight phases: departure, cruise and landing. The departure and the landing phase are the most important when measuring aircraft noise, due to the close distance to the population [18]. Both phases have different dominant noise sources depending on their operational conditions. When an aircraft is departing a high thrust is required to get in the air and start climbing. The high thrust levels of the engine result in maximum engine noise. When looking at the approach phase, the engine thrust is minimal. By using low thrust levels, the noise coming from the engine is lower. The main noise sources in the approach phase become the extracted landing gear, high lift devices and speed brakes. This means the noise generated by the airframe is more dominant. For the approach and descent phase the aircraft has been divided in airframe and engine noise, which are called the 'classical' noise sources. Figure 2.16 shows the airframe components (left) and the engine components (right).

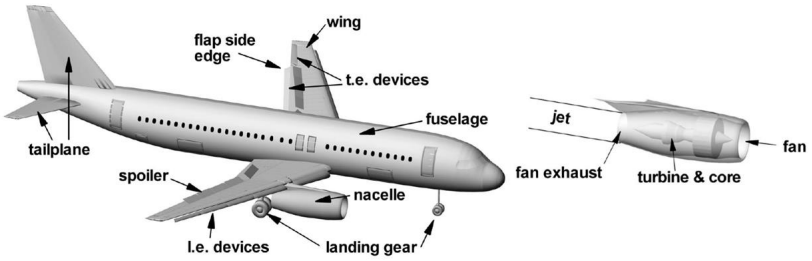

Figure 2.16: The classical noise sources of an aircraft [18]

The airframe noise is expected to be mainly at the lower frequencies and the engine noise also at the higher frequencies. Figure 2.17 displays the power spectral density as a function of the frequency for a landing Airbus A321 and a Boeing 737. The swinging black line represents the measured spectrum and the smooth lines are the modelled noise of the wing, slats, flaps, main landing gear, nose landing gear and the total airframe noise. The noise is modelled with the semi-empirical airframe noise model of Fink in the article 'Noise breakdown of landing aircraft using a microphone array and an airframe noise model' by D.G. Simons, M. Snellen, R. Merino-Martinez and A.M.N. Malgoezar [14]. Within Figure 2.17 it can be seen that up to 4500 Hz, the airframe noise is mainly contributing to the total noise of the aircraft. Above 4500 Hz the engine noise is dominant. From the airframe noise, the noise from the main landing gear is the most dominant in the overall spectrum. However, the noise from the flaps are a good competitor in the plot of the Boeing 737. The exact noise of the airframe components will deviate for various aircraft and their settings, but the modelled data gives a good indication of what noise sources to expect at certain frequencies for landing aircraft.

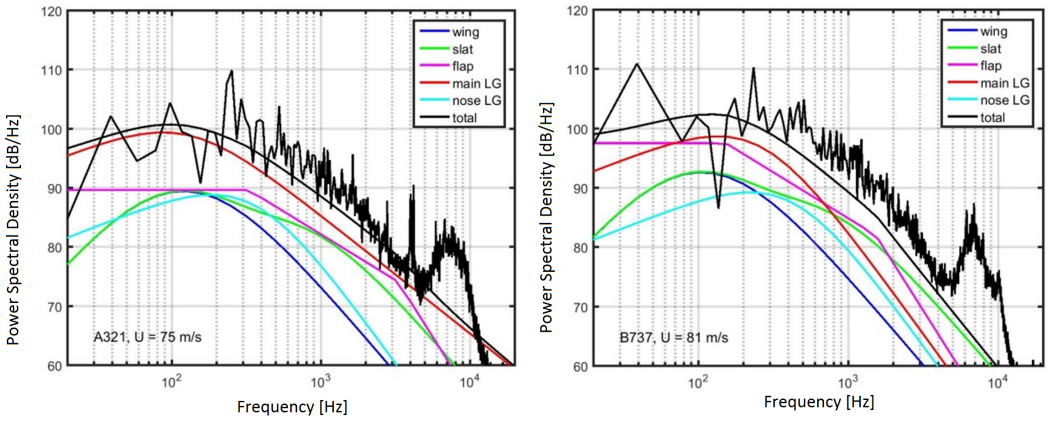

Figure 2.17: Modelled airframe noise (smooth lines) and measured total noise of a landing Airbus A321 (left) and a Boeing 737 (right) [14]

3

EXPERIMENTAL SET-UP FOR DIRECTIVITY QUANTIFICATION

A less known factor in the research on aircraft noise is the reaction of an acoustic camera to sources measured under an angle in comparison to sources measured directly overhead the camera. For this reason an acoustic camera is quantified with the emphasis on its directivity performance. This chapter describes the experiment which starts with a measurement plan in Section 3.1. Section 3.2 presents the measurement set-up and the chapter closes with a description of the corrections required (Section 3.3).

3.1. MEASUREMENTS

The goal of the experiment is to quantify the acoustic camera with the emphasis on the directivity performance. A sound source is placed at various angles relative to the plane of the camera to get information on this directivity performance. The best results are obtained with minimal sound interference, which is assured with performing the measurements in an anechoic chamber. The anechoic chamber has foam wedges on all walls, the ceiling and the floor. These wedges will absorb the sound, so there are no reflections. The mechanism by which the wedges decrease the sound, is by bouncing the waves impinging the wall in the gap between the wedges. During the bouncing, the acoustic energy of the sound wave gets dissipated through the air's molecular viscosity and the absorption of the foam. [26] The anechoic chamber of applied sciences at the TU Delft is used for the measurements. The chamber has a surface area of 8 x 8 m and is displayed in Figure 3.1.

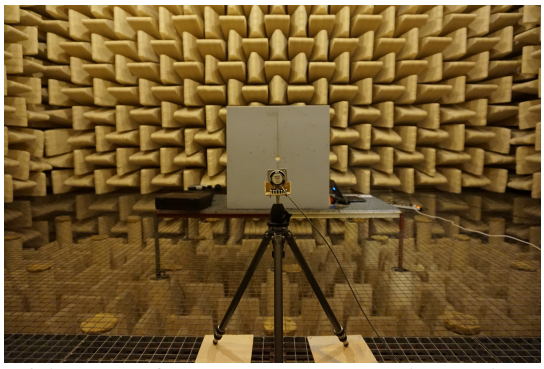

Figure 3.1: The set-up of the quantification experiment in the anechoic chamber of the TU Delft

For assessing the performance of the acoustic camera, to measure sound sources also at angles other than 0 degrees to the array, the sound source is measured under an angle and compared to measurements with the source in front. Keeping the limitations of the anechoic chamber and the measurement time available in mind, the measurement angles are set on 0 to 45 degrees in steps of 15 degrees in all directions. The 16 measurement positions of the speaker are given in Table 3.1 and are visualised in Figures 3.2 and 3.3. Figure 3.2 displays the reference system required to explain the measurement angles. The plane of the speaker

lies parallel to the plane of acoustic camera and the z-position is the distance between those planes. This distance stays constant for all measurements. For the horizontal measurements the source moves over the x-axis, for the vertical measurements over the y-axis and for the diagonal measurements over both the x- and y-axis. Figure 3.3 represents the plane of the speaker with all measurement positions. The big black dot in the middle is the starting position which is parallel to the middle of the array. The middle of the array is the origin of the reference system. The red dots are for the horizontal measurements, the blue crosses for the vertical measurements and the green triangles for the diagonal measurements. The exact spacing between the measurements is dependent on the distance between the acoustic camera and the speaker. The numbers in the figure match the numbers of the measurements in Table 3.1.

Table 3.1: Measurement number with its position during the quantification experiment

Nr.	Position	Nr.	Position
1	0 deg.	9	30 deg. Vertical
2	15 deg. Horizontal	10	45 deg. Vertical
3	30 deg. Horizontal	11	15 deg. Horizontal & 15 deg. Vertical
4	45 deg. Horizontal	12	30 deg. Horizontal & 30 deg. Vertical
5	-15 deg. Horizontal	13	45 deg. Horizontal & 45 deg. Vertical
6	-30 deg. Horizontal	14	-15 deg. Horizontal & 15 deg. Vertical
7	-45 deg. Horizontal	15	-30 deg. Horizontal & 30 deg. Vertical
8	15 deg. Vertical	16	-45 deg. Horizontal & 45 deg. Vertical

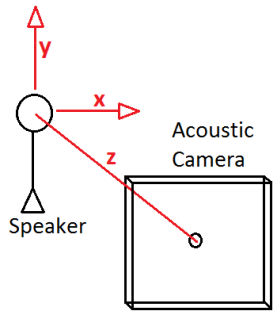

Figure 3.2: Reference system for the measurement set-up

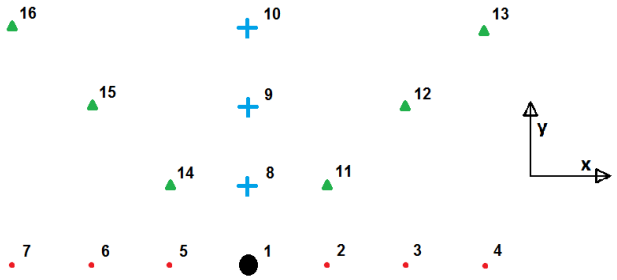

Figure 3.3: Schematic of the source positions placed on a plane which lies parallel to the plane of the acoustic camera. Dots are horizontal-, crosses are vertical- and triangles are diagonal measurements

The human hearing range and the speaker performance have to be taken into account for the determination of the played frequencies. The human hearing range is from 20 to 20.000 Hz [2]. Frequencies below or above these values cannot be heard by the human ear and are not important for these noise measurements. The speaker used during the experiments cannot play frequencies below 250 Hz. This means that the measurement frequencies will be in between 250 and 20.000 Hz. Only the centre frequencies of the 1/3rd octave band or the octave band are used to limit the measurement time. Within the 1/3rd octave band there are 20 frequencies to play and within the octave band 7 frequencies. For these measurements the octave band is used to keep within the reserved time-frame. This means the measurements will be carried out at 250, 500, 1000, 2000, 4000, 8000 and 16000 Hz.

3.2. SET-UP

The measurements are performed in the anechoic chamber of applied sciences of the TU Delft. A stable platform is required for both the speaker and the acoustic camera. This stable platform is a metal grid which can be placed on predefined locations in the anechoic chamber. Because the placement of the metal grids is predefined, there is a limitation in the position of the measurement equipment. Two metal grids are placed opposite of each other at a separation distance of 2.4 m. On one grid the acoustic camera will be placed and on the other grid the speaker (Visaton K50 SQ). The speaker is the most movable of the two and will be changing its position during the measurements to match the desired angles. The acoustic camera used

consists out of a 1 x 1 m wooden board with foam and 64 microphones placed in a random configuration (Figure 3.4).

The speaker will be placed on a camera stand to make it stand vertical and adjust the height. The amplifier is built in the speaker and is connected to a computer which generates the required frequencies through a Matlab program. The acoustic camera is placed on the other grid with its microphones connected to a data acquisition system (DAQ). This is an Arduino Micro DAQ from the TU Delft, called 'Camera 2'. The DAQ is connected to a laptop with Labview software, which controls the camera. Attached to the laptop are an environmental sensor (AM2302) and a hard drive to save all measured data. A dB meter of Brüel and Kjaer is placed in the middle of the acoustic camera to be able to verify the results. The set-up of the experiment is displayed in Figure 3.1 and Figure 3.5.

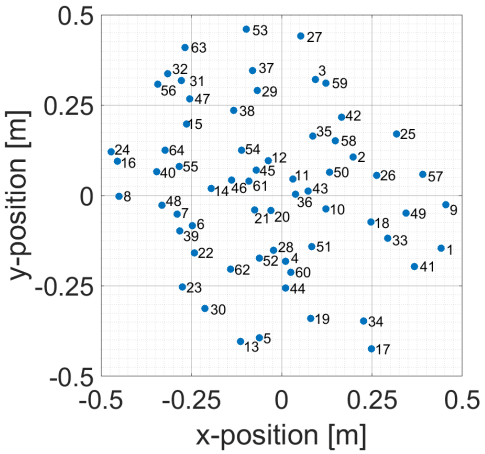

Figure 3.4: Array configuration of the acoustic camera

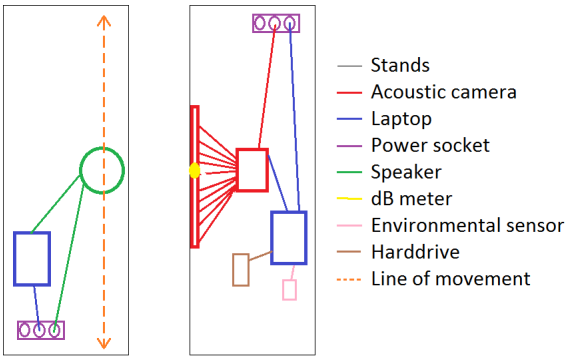

Figure 3.5: Schematic picture of the set-up of the quantification experiment

3.3. CORRECTION

Every microphone should measure the same sound pressure level when subjected to a source under the same circumstances. To check if all microphones react equally, they have to be calibrated. This is done by means of a pistonphone calibration.

For the pistonphone calibration the Brüel and Kjaer Type 4230 was used (Figure 3.6). This device emits sound at a frequency of 1000 Hz with a SPL of 94 dB. The pistonphone can be placed over a microphone and the sound is recorded for each microphone individually. The sound measured is compared to the sound which is emitted and is used to derive a correction factor for each microphone. Eight microphones did not pick up the signal, or picked up a very weak signal. These microphones were broken and cannot be used in the analysis of the measurement. The broken microphones were microphone 13, 14, 21, 23, 26, 50, 58 and 64.

Figure 3.6: Pistonphone of Brüel and Kjaer Type 423

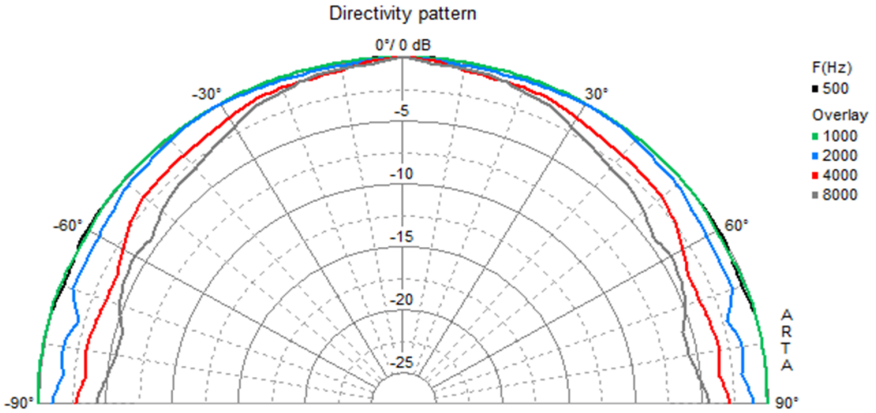

Figure 3.7: Speaker directivity according to the manufacturer [27]

The sound from the speaker is not the same as is measured by the acoustic camera. Corrections have to

be applied to the data to be able to derive the sound emitted from the received signals. The first correction is for the spreading of sound. Furthermore, the air absorbs part of the signal due to internal friction. Another correction is for the sound reflecting off the walls and floor. However, these measurements are performed inside an anechoic chamber, there are no reflections and this correction can be neglected here. The sound source itself is not completely omnidirectional. The manufacturer has provided the omnidirectionality of the speaker which is displayed in Figure 3.7. For the angular measurements the SPL correction is derived from this figure to be able to obtain the same SPL values as when is measured at 0 degrees. All corrections combined leads to Equation 3.1. In this equation SPL stands for the Sound Pressure Level in decibel, r is the distance from the microphone to the sound source and α is the sound attenuation coefficient. The correction is carried out for each microphone individually.

$$SPL(1m) = SPL(r) + 20log(r) + \alpha r + Speakercorrection \tag{3.1}$$

4

DATA ANALYSIS DIRECTIVITY MEASUREMENTS

The ability of the acoustic camera to record the sound pressure level and the position of a sound source under an angle is evaluated to determine its directivity performance. The data of the measurements described in Chapter 3 are analysed through conventional beamforming. First the results of the individual microphones are examined in Section 4.1. Section 4.2 looks at the beamform results and the effect of the frequency and measurement angle of the source plots. After this, the array performance is analysed. Section 4.3 displays the performance with respect to the estimated source strength and Section 4.4 with respect to the estimated source position.

4.1. MICROPHONE ANALYSIS

The data analysis starts by looking at the individual microphones. First the frequency response of the microphones is compared to the sound pressure level (SPL) measured with the decibel meter. The set-up as described in Chapter 3.2 was used with the source at a measurement angle of 0 degrees and the signal corrected as mentioned in Chapter 3.3. The frequency response measured with the dB meter and with all microphones is displayed in Figure 4.1. Within this figure, eight microphones have a large deviation from the dB meter, these are the broken microphones which were mentioned in Chapter 3.3 (microphone 13, 14, 21, 23, 26, 50, 58 and 64). Leaving out the broken microphones gives Figure 4.2. Within this figure the SPL deviation between the individual microphones for the measured frequencies can be derived. To make this clearer, a box plot is made of the non-broken microphones which is displayed in Figure 4.3. By knowing the deviation of the microphones, the accuracy of the measured data can be derived. The closer the SPL of all microphones are, the more accurate the measurement results. In this case the minimum and maximum values of the microphones are more then 10 dB apart for all frequencies, which is quite large. However, this deviating is due to a few outliers. When looking at the majority of the microphones the difference at 250, 1000, 2000 and 16000 Hz is only 3 dB. The spread at 8000 Hz is largest with approximately 6 dB, which means the results can be less accurate at this frequency.

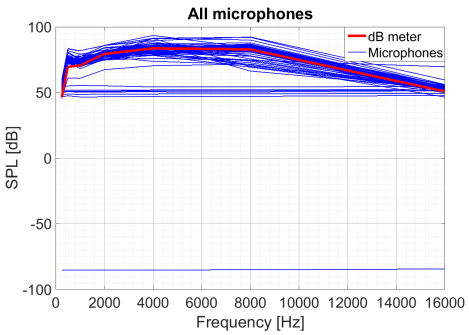

Figure 4.1: Frequency response of the decibel meter and all microphones

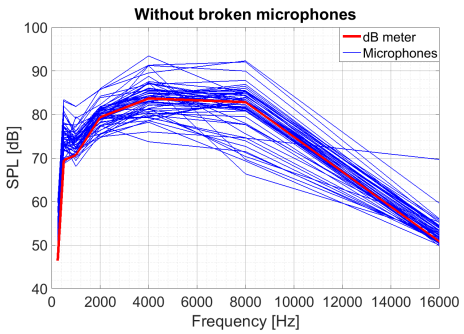

Figure 4.2: Frequency response of the decibel meter and all non-broken microphones

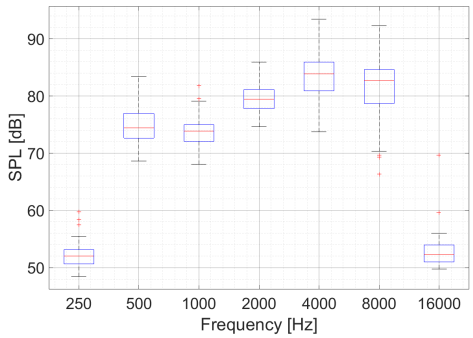

Figure 4.3: Box plot of the SPL of all non-broken microphones

Microphones 13, 14, 21, 23, 26, 50, 58 and 60 are broken and cannot be used for the analysis. Before neglecting these microphones entirely, their influence on the measurement results is evaluated. Their position and SPL with all microphones and with leaving out the broken microphones is displayed in Table 4.1. These values are derived from their source plots, which are obtained through conventional beamforming and displayed in Figure 4.4. From the table and the figure it can be concluded that the position of the source does not change. The SPL is slightly higher when leaving the microphones out of the calculations. This is as expected since the broken microphones presented a signal with a lower SPL then the source was emitting. This increase is about 1 dB which means it is hardly distinguishable by the human ear. The influence of broken microphones on measurement results is discussed in the article 'Sparse arrays and array health check tool' by Jorgen Grythe [29]. The conclusion of this article is that the measurement results of an array with broken microphones is the same as for an array with all microphones working, if there are still enough microphones left and the configuration has not changed too much. The experiment started with 64 microphones of which 8 are broken. This means 56 microphones are still working. The broken microphones are spread out on the array and the microphone configuration stays approximately the same. This means that it is expected that the broken microphones can be left out without large consequences.

Table 4.1: Influence of the broken microphones 1000 Hz and at 0 and 30 degrees horizontal

	Position		**SPL**	
	0 deg	**30 deg**	**0 deg**	**30 deg**
All microphones	(-0.0287, -0.0626)	(1.4852, -0.0061)	97.6428	97.3973
Leave out the broken microphones	(-0.0287, -0.0626)	(1.4852, -0.0061)	98.6595	98.3920

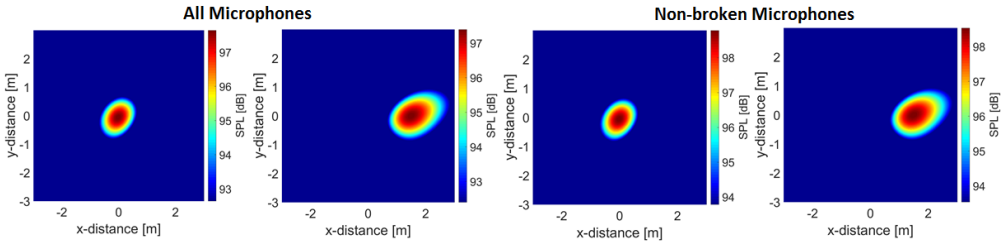

Figure 4.4: Beamform plots made including all microphones and including only the non-broken microphones for 0 and 30 degrees of the horizontal measurements

4.2. BEAMFORM RESULTS

The next step in the analysis is to look at the effect of the frequency and the measurement angle on the source plots. The source plots are made according to conventional beamforming as described in Chapter 2.2. It is a stationary source and the signal is corrected for the atmospheric effects and the speaker performance as described in Chapter 3.3. The sound measured is played from a speaker as described in Chapter 3, which acts like a monopole source and will send omnidirectional sound waves. Only the source plots at 250 Hz have a different behaviour, for which there are three possible causes. First, the speaker performance at 250 Hz is not good and influences the measurement data. Secondly, the low frequency used results in a low resolution for

beamforming, thus creating more blurry images. And as third, the absorption of the anechoic chamber could be failing at this frequency. To be able to absorb the low frequencies, the cones on the walls of the anechoic chamber must be of a certain size. This means there is a minimum frequency from which the anechoic chamber does not have reflections. This minimum frequency is unknown for the TU Delft anechoic chamber. However it is possible that 250 Hz lies below this minimum, not all sound is absorbed and reflections are measured. Therefore the data measured at 250 Hz is left out of the analysis.

The effect of the frequency on the beamform plot is evaluated with the help of Figure 4.5. The figure shows that the higher the frequency, the more side lobes appear and the smaller the main lobe at the source position. This behaviour can be explained with theory. According to Rayleigh's limit the resolution increases with frequency, which decreases the main lobe in the source plot. Furthermore, from the equation $\lambda = \frac{c}{f}$ it can be derived that the higher the frequency, the smaller the wavelength. This smaller wavelength results in a lower beam width which is calculated with the formula $\theta_b = \frac{\lambda}{N \cdot D}$, in which N is the number of microphones and D the aperture of the array. [4] The increase of side lobes and decrease of the main lobe width with increasing frequency is also confirmed by other researches like the article 'Evaluation of Beamforming Systems' from R. Schröder and O. Jaeckel [28].

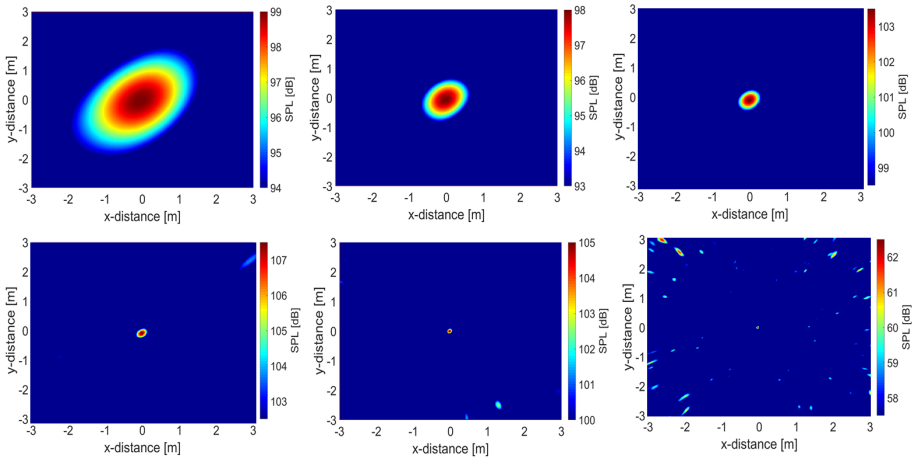

Figure 4.5: Source plots of the source in at 0 deg. for 500, 1000, 2000, 4000, 8000 and 16000 Hz (FLTR)

Figure 4.6 shows the position of the positive horizontal sources at 1000 and 4000 Hz. In the figure the source gets wider with increasing measurement angle. This effect is more apparent at the lower frequencies. The increasing main lobe width with increasing angle can be explained with the help of the steering angle. When increasing the measurement angle to the source, the steering angle is increased. According to theory, an increase in steering angle will lead to an increase in main lobe width [4]. This is displayed with a theoretical directional response function in Figure 4.7. The figure shows that when increasing the steering angle, the width of the main lobe gets larger as is also the case for the beamform plots.

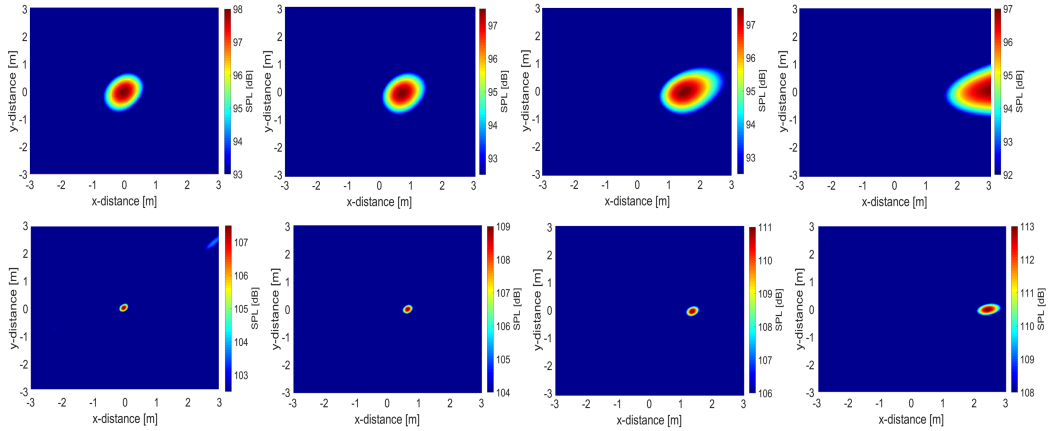

Figure 4.6: Source plots at 1000 Hz(top) and at 4000 Hz(bottom) for 0, 15, 30 and 45 degrees (FLTR)

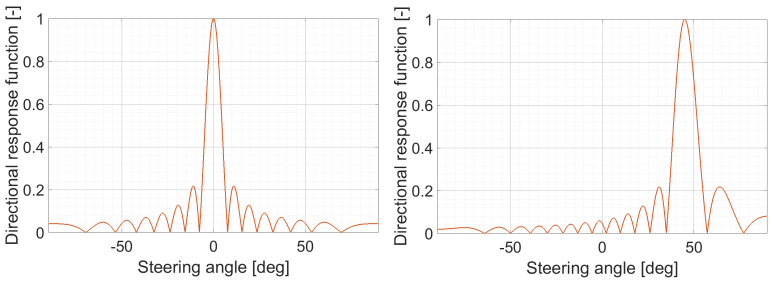

Figure 4.7: Directional response function of a theoretical case for a steering angle of 0 (left) and 45 (right) degrees at 1000 Hz

4.3. SOURCE STRENGTH

The next step in the analysis is the estimation of the source strength to determine the array performance. When evaluating the SPL of the measurements, it became apparent that 250 and 16000 Hz have a lower SPL than the other frequencies. The reason for this could be the speaker performance. The design frequency of the speaker is from 250 to 10000 Hz according to the manufacturer . This means that 16000 Hz lies outside the scope of the speaker. 250 Hz lies on the edge of the speaker performance, which can also result in a slight offset of the frequency of the sound. Power spectral density (PSD) plots were made to check if the frequency measured complies with the frequency played (Figure 4.8). From the figure it is visible that the speaker plays multiple harmonics at 250 and 16000 Hz, while there is just one clear peak at 1000 Hz. Due to the lower speaker performance at 250 and 16000 Hz, they are not used in further analysis.

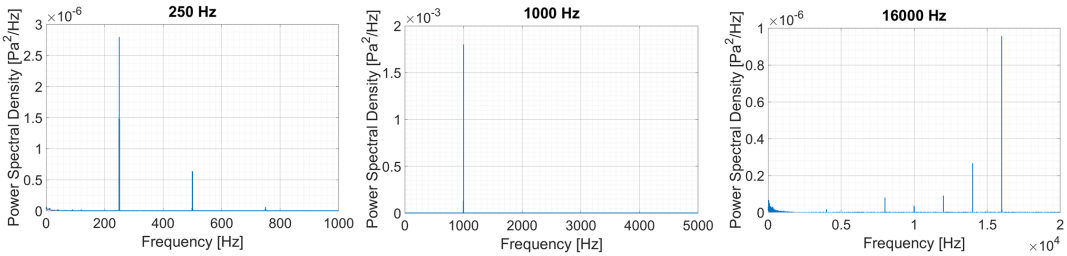

Figure 4.8: Power spectral density plots at 0 degree for 250, 1000 and 16000 Hz

For the rest of the frequencies the SPL obtained through conventional beamforming is displayed in Figure 4.9. In this figure the horizontal measurements have a source angle only on the x-axis, the vertical measurements only on the y-axis and the diagonal measurements both on the x- and y-axis as described in Chapter 3.1. The SPL does not stay constant with measurement angle, but no clear effect can be found except for 8000 Hz, which shows a distinct behaviour compared to the other frequencies. The SPL deviation between the speaker in front of the camera and under an angle is 1 dB when staying within a measurement angle of 15 degrees. This means that the measurements under a small angle give a good estimation of the real source strength. However, due to the slight deviation it can result in different main sources. The OSPL (Overall Sound Pressure Level) difference of a Boeing B737 between the nose landing gear and the trailing edge devices is for instance less than 2 dB [4]. This means that angular measurements can result in a different indication of the main noise source.

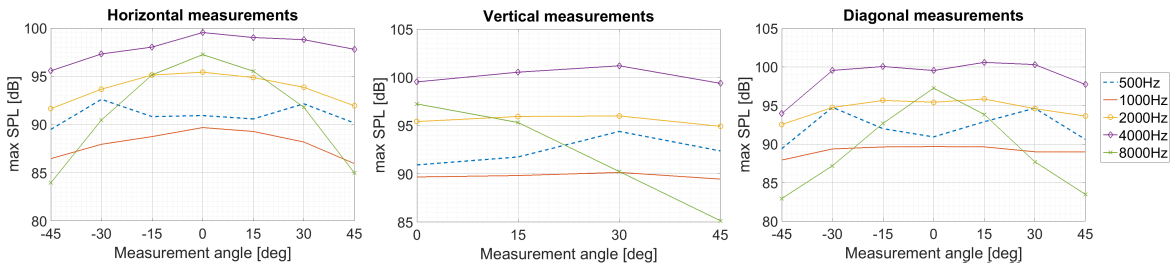

Figure 4.9: SPL for all measurement angles obtained through conventional beamforming

4.4. SOURCE POSITION

The position of the speaker during the experiment is known and can be compared with the position obtained through conventional beamforming. Figure 4.10 shows the position offset between the real source position and the estimated position of the source in the beamform plots for the positive horizontal measurements. The difference of the real and the estimated source position is relatively large, especially at the lower frequencies. At 500 and 1000 Hz the offset in x-position is so high that the mid of the source falls out of the measurement window (Figure 4.11). The offset is largest in the direction of the measurements and increases with increasing measurement angle. This means that the deviation in x-position is largest for the horizontal measurements, while for the vertical measurements the deviation in y-position is largest. This is displayed in Figure 4.12 with the real source position indicated with a white dot. The position deviations are of the same order in all directions.

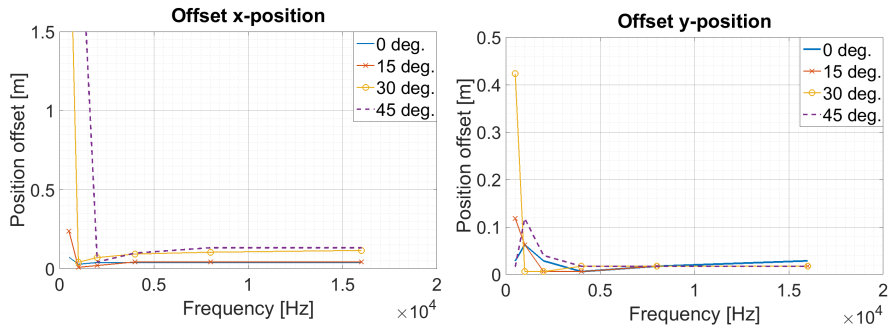

Figure 4.10: Offset of the source position for positive horizontal measurements [m]

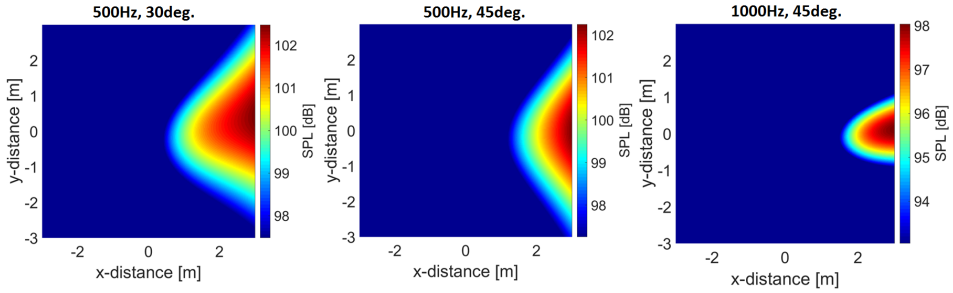

Figure 4.11: Beamform plots of 500 Hz at 30 and 45 degree and 1000 Hz at 45 degree for the positive horizontal measurements

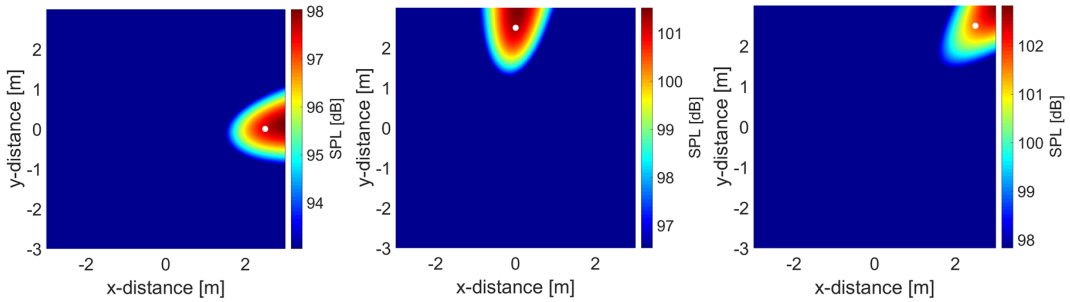

Figure 4.12: Beamform plots at 1000 Hz and a measurement angle of 45 degrees in the horizontal, vertical and diagonal direction with a white dot indicating the real source position

The position offset arises due to the chosen steering vector. Different steering vectors are used in the past, but none can provide both the exact source strength and the exact source location [30]. The errors are small for sources with a small measurement angle. However, for larger measurement angles the deviations become

unacceptable and two different normalisations have to be applied. First the correct source position is found with Equation 4.1.

$$\vec{w}_j = \frac{\vec{g}_j}{||\vec{g}_j||} \tag{4.1}$$

After this, the beamform analyses can be repeated with Equation 4.2 instead of 4.1 to determine the exact source strength.

$$\vec{w}_j = \frac{\vec{g}_j}{\vec{g}_j \vec{g}'_j} = \frac{\vec{g}_j}{||\vec{g}_j||^2} \tag{4.2}$$

Figure 4.13 shows the difference in beamform plots when using only Equation 4.1 (left) and only Equation 4.2 (right). In the figure it can be seen that the source position shifts closer to the real position of the speaker (the white dot) with Equation 4.1, but that the SPL is decreased. Figure 4.14 displays the deviation between the estimated and the real source position with the two equations at 15 degrees for the horizontal measurements. This angle is chosen since this is the most interesting for fly-over measurements. While using Equation 4.1 there is still a small deviation left. However this is less than 5 cm, which cannot be distinguished in the fly-over measurements.

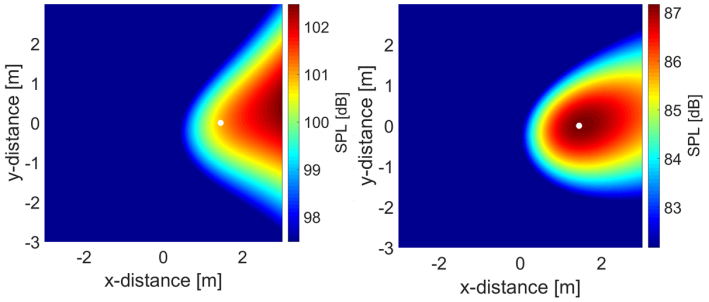

Figure 4.13: Beamform plots with Equation 4.2 (left) and 4.1 (right) at 500 Hz and 30 degrees of the horizontal measurements. The white dot is the real source position

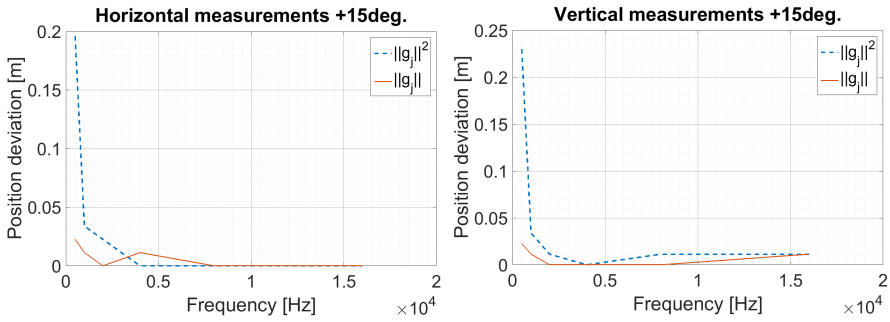

Figure 4.14: Position deviation of Equation 4.2 and 4.1 at a measurement angle of 15 degrees for horizontal (left) and vertical (right) measurements

5

PREVIOUS FLY-OVER CAMERA

This chapter describes the analysis of the fly-over camera previously used by the TU Delft. The camera is designed by a group of students and their process is described in Reference [31]. The analysis of the previous camera includes their recommendations (Section 5.1), the transmission loss (Section 5.2), a spectrogram analysis (Section 5.3) and an evaluation on the frequency band of interest (Section 5.4).

5.1. FLAWS

The performance of the previous camera is mapped to be able to improve the design. This information is obtained through Reference [31] and a conversation with Kirk Scheper who worked on this project. The comments on elements that can be improved are:

- The exact measurement angle is unknown.
- A separate optical camera is used, but better pictures will be obtained with an optical camera fixed in the structure.
- The measurement time is limited by the laptop battery.
- The measurements are limited by the memory available.
- Cables are attached at the wrong position.
- Only 32 microphones are used, limiting the signal quality.
- The resolution of the camera can be low for sources far away.
- It is hard to know the exact positioning of the microphones
- There is little information on the ground effect, which might interact with the structure.

For all these comments a solution is found starting with the measurement angle. For fly-over measurements the camera has to be set level, which can be measured with a spirit level meter. If the measurement site is crooked, the structure should be able to counteract this offset. This means a support structure which is adjustable in height has to be used.

Instead of a separate optical camera, a holding for the optical camera can be implemented in the construction. It is best to place the optical camera in the middle of the construction for the best images.

For a longer measurement time an external battery can be used. The limited space for the data can be solved by using an external hard drive with a large storage capacity.

To avoid wrong positioning of microphones and cables, everything needs to be labelled and written down in a report. It is less likely that a wrong connection occurs when it is clearly stated.

In Chapter 2 it was mentioned that an increase in microphones results in better source plots. However, the number of microphones was limited by the available budget and the data acquisition system. For the optimised acoustic camera a predefined data acquisition system is used with slots for 64 microphones. This is twice as many the microphones as before, which will result in an improved signal.

The resolution of the camera is dependent on its Rayleigh limit which is described in Chapter 2. An increase in the Rayleigh criterion means an increase in resolution. This can be made possible by increasing the aperture of the array or decreasing the distance to the source. It is hard to decrease the distance to the source,

which means that the aperture of the array is increased. To ensure an increased resolution the aperture relative to the previous camera is doubled. The aperture of the previous camera was 1.7 m, which means the optimised aperture should be 3.4 m.

To know the exact position of the microphones a construction has to be made in which the microphones are always in the exact same place. The microphones should be clamped to avoid them from tilting. A solution for this problem is dependent on the exact lay-out of the construction, but it should be kept in mind during the trade-off of potential configurations.

Extra research is required for a better understanding of the ground effect on the camera. This research is divided in two sections: Section 5.2 calculates the transmission loss of the camera and Section 5.3 is a spectrogram analysis of the B737-800 measured with the previous fly-over camera.

5.2. TRANSMISSION LOSS

When a sound wave hits a wall, part of the wave will be reflected and part of the wave will pass through this wall. For the acoustic camera, a sound wave could pass through the construction plates, reflect off the ground, pass through them again, hit the microphones and influence the measurement results. To have an idea about this influence, the transmission loss of the previous acoustic camera is calculated.

The camera is made out of 10 mm multiplex, topped with Flamex GU 15 mm foam and is placed approximately 300 mm above the ground. For these calculations it is assumed that the sound wave is perpendicular to the construction. Another assumption made is that the wooden plank and the foam are two individual surfaces which are surrounded by air (Figure 5.1). The transmission loss (TL) of both surfaces is added up by: $TL_{total} = 10log(10^{TL_{wood}/10} + 10^{TL_{foam}/10})$. This means that the reflections of the sound waves in between the media are not taken into account. The transmission loss calculated in this section is the most beneficial case. It is not the exact value, but gives an approximation to get an idea about transmission loss of the particular construction. The ground surface is modelled as grass and concrete.

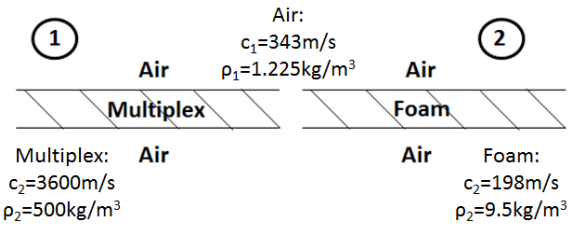

Figure 5.1: Assumed state of the construction materials with their properties

The transmission loss of sound going through an object can be calculated with equation 5.1. In this equation TC is the transmission coefficient, which can be calculated with Equation 5.2. [2] In this equation c is the speed of sound and ρ is the density. The subscript 1 is for air and 2 for multiplex or foam respectively.

$$TL = 10log(\frac{1}{|TC|^2}) \tag{5.1}$$

$$TC_{12} = \frac{2\rho_2 c_2}{\rho_2 c_2 + \rho_1 c_1} \tag{5.2}$$

Assuming $\rho_2 c_2 >> \rho_1 c_1$ brings us to Equation 5.3. This assumption is valid for both multiplex and foam as displayed in Table 5.1.

$$|TC|^2 = \frac{4}{4cos^2(k_2 d_2) + (\frac{\rho_2 c_2}{\rho_1 c_1})^2 sin^2(k_2 d_2)} \tag{5.3}$$

Table 5.1: Material properties of Air, Multiplex and Flamex GU foam

	Air	**Multiplex**	**Flamex GU foam**
Speed of sound $[m/s]$	343	3600	198
Density $[kg/m^3]$	1.225	500	9.5
$\boldsymbol{\rho \cdot c}$ $[kg/(m^2 s)]$	420.175	1800000	1881

The next approximation is $\frac{\rho_2 c_2}{\rho_1 c_1} sin(k_2 d_2) >> 2cos(k_2 d_2)$ which gives Equation 5.4. This assumption is displayed in Figure 5.2 for multiplex (left) and foam (right) and for frequencies from 30 to 20000 Hz. If the assumption is valid, the red solid line should be above the blue striped line. This is the case for multiplex, but not for al frequencies for foam. This means that for foam the transmission coefficient of Equation 5.3 is used. For wood, the transmission coefficient can be simplified even more.

$$|TC|^2 = \frac{4\rho_1^2 c_1^2}{\rho_2^2 c_2^2 sin^2(k_2 d_2)} \tag{5.4}$$

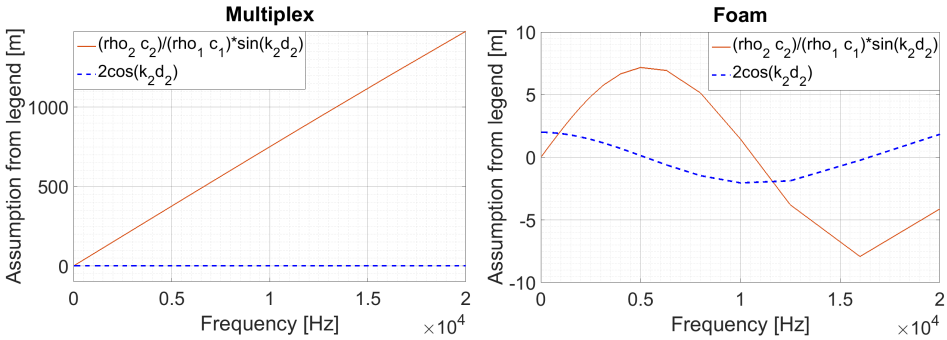

Figure 5.2: Visualisation of assumption $\frac{\rho_2 c_2}{\rho_1 c_1} sin(k_2 d_2) >> 2cos(k_2 d_2)$ for multiplex (left) and foam (right)

The last approximation is $k_2 d_2 << 1$, which results in Equation 5.5. The approximation is displayed in Figure 5.3 for frequencies from 30 to 20000 Hz. The blue striped line has to stay below one (the red solid line) to make the assumption valid. This is the case and the assumption holds for multiplex.

$$|TC|^2 = \frac{4\rho_1^2 c_1^2}{\omega^2 s^2} \tag{5.5}$$

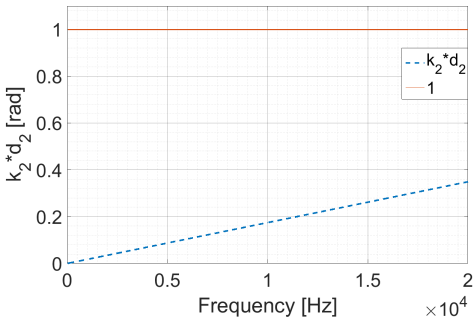

Figure 5.3: Visualisation of assumption $k_2 d_2 << 1$ for multiplex

With the known transmission coefficients for multiplex and Flamex GU foam, the transmission loss can be calculated. Equation 5.6 is used for multiplex and Equation 5.7 for Flamex GU foam.

$$TL = 20log(\frac{2\pi f s}{2\rho_1 c_1}) \tag{5.6}$$

$$TL = 20log(\frac{2cos(k_2 d_2) + \frac{\rho_2 c_2}{\rho_1 c_1} sin(k_2 d_2)}{2}) \tag{5.7}$$

The sound loss due to the air absorption is calculated with Equation 5.8. In this equation r is the distance the sound travelled and α the sound attenuation coefficient. The surface reflection is calculated with Equations 2.8 and 2.9 which were mentioned in Chapter 2.

$$TL_{air} = \alpha r \tag{5.8}$$

The combination of these equations resulted in the transmission loss displayed in Figure 5.4. The maximum sound pressure level of a Boeing 737 is around 93 dB. This means that frequencies above 1250 Hz will

be filtered for a grass surface and above 2000 Hz for a concrete surface.

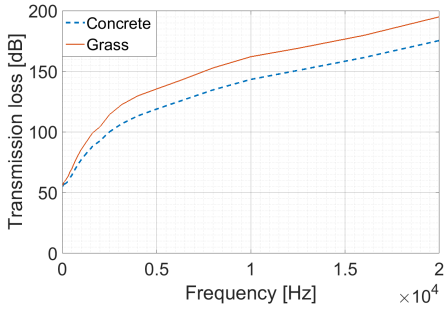

Figure 5.4: Transmission loss of the TU acoustic camera used for fly-over measurements

5.3. SPECTROGRAM ANALYSIS B737-800

A spectrogram analysis is carried out to see the behaviour of the acoustic camera regarding the ground effect. For this analysis fly-over data of the Boeing B737-800 obtained with the DSE fly-over camera is used [31]. The spectrograms of microphone 1 and microphone 30 are displayed in Figure 5.5.

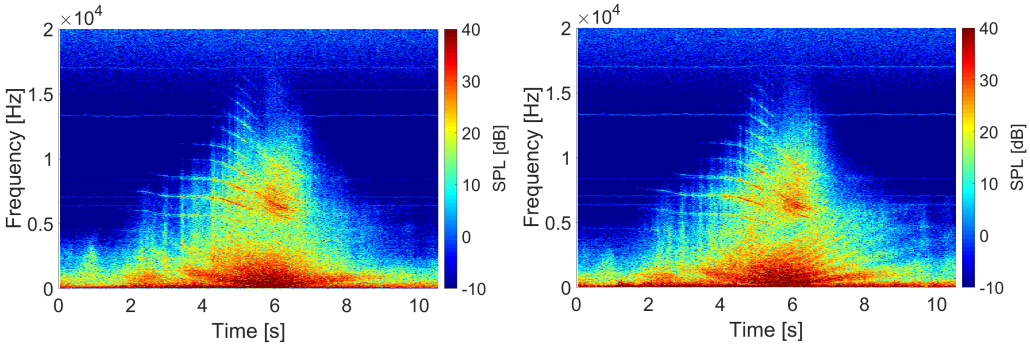

Figure 5.5: Spectrogram of the B737-800 measured with microphone 1 (left) and microphone 30 (right)

The Lloyd's mirror pattern is visible in both spectrograms. It is however less present for microphone 1 than microphone 30 and for microphone 30 it is mainly visible at the right side of the figure (after 6 seconds). As a next step all microphones are evaluated and the results compared with their position in the array to obtain a better understanding of this result. The array configuration with microphone numbering is displayed in Figure 5.6.

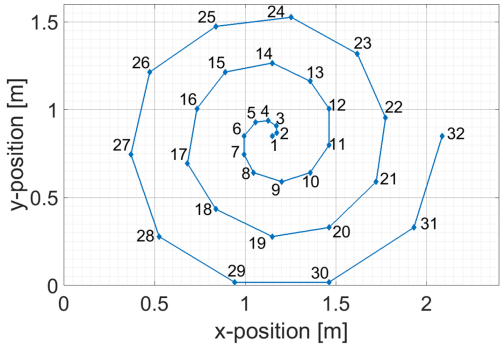

Figure 5.6: The array configuration of the acoustic camera during the measurements of the B737-800

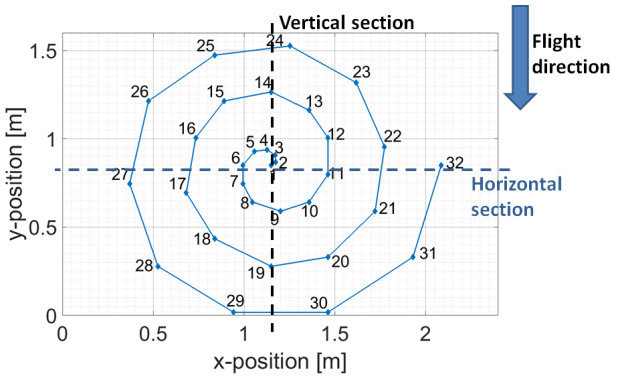

Figure 5.7: The array configuration of the acoustic camera during the measurements of the B737-800 with flight track and section indication

Looking at the position of the microphones and their spectrograms an interesting phenomenon was discovered. It appeared that the microphones which were positioned near the edge of the camera and in the

flight direction of the aircraft had the most fringes. This effect is made clear in Figures 5.8 and 5.9. Figure 5.8 displays the spectrogram of a vertical section of the camera with microphones 24, 14, 1, 9, 19 and 29 and Figure 5.9 displays the spectrogram of a horizontal section of the camera with microphones 27, 17, 7, 11, 21 and 32. The sections and the flight track are displayed on the array in Figure 5.7.

When the aircraft is approaching the array, sound waves reflect off the ground and hit the microphones closest to the edge. This is best visible for microphone 24 in which Lloyd's mirror reflection is visible between 3 and 6 seconds (during approach). The same is happening for microphone 29 where Lloyd's mirror reflection is visible in between 6 and 9 seconds (when the aircraft is flying away from the array). The microphones which are positioned in the middle of the array only have one parabolic line instead of the multiple fringes. This effect is also present for the microphones close to an edge, but not in flight direction (microphones 27 and 32). This means that the fringes have the most influence on the microphones positioned close to the edge and in flight direction of the aircraft. The effect weakens for microphones positioned more than 30 cm from the edge of acoustic camera.

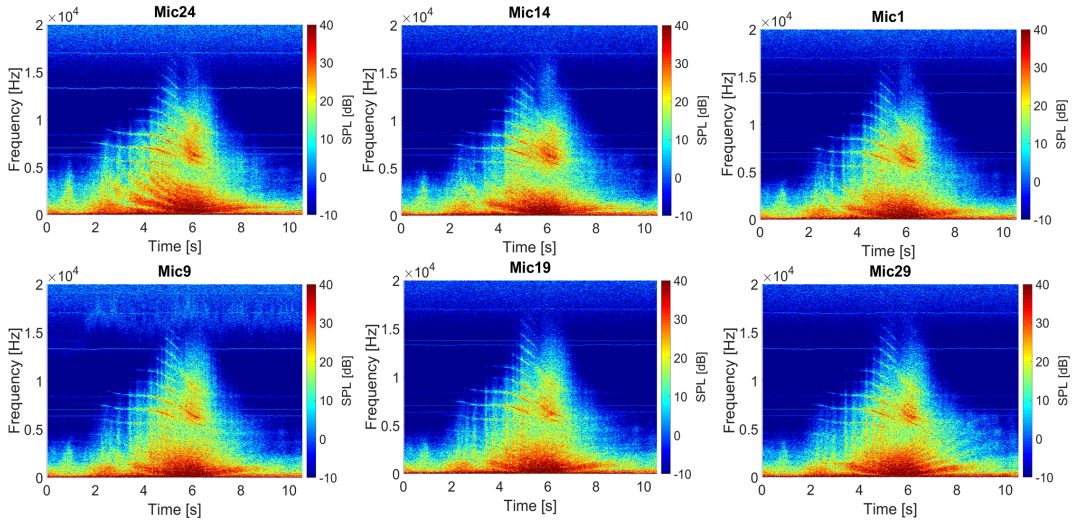

Figure 5.8: Spectrogram of microphones 24, 14, 1, 9, 19 and 29 which lie on a vertical section of the acoustic camera

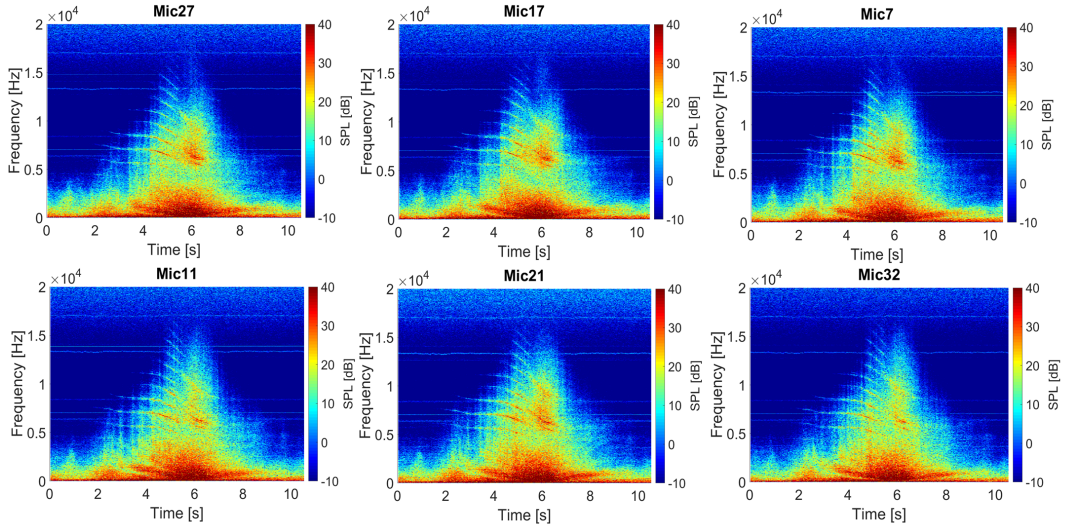

Figure 5.9: Spectrogram of microphones 27, 17, 7, 11, 21 and 32 which lie on a horizontal section of the acoustic camera

The observed Lloyd's pattern can be caused by phenomena. First of all the ground reflection is considered. Sound waves are emitted from a source, reflect off the ground and penetrate through the construction of the

array to influence the measurement results (Figure 5.10). If this happens the observed Lloyd's pattern should be the same for all microphones. This means that the asymmetric fringes in the spectrogram are not caused by the ground reflection. However, there is one line visible for all microphones which may be caused by the ground reflection (Figure 5.9). In Section 5.2 it was concluded that the higher frequencies would be blocked, but the lower frequencies could partly penetrate the construction of the acoustic camera. The parabolic line of the ground effect visible for all microphones is at the lower frequencies. This means that it is possible that part of the sound penetrates the construction and interferes with the signal. The line also matches the theoretical expectation which is calculated with Equation 2.10 and plotted in Figure 5.11.

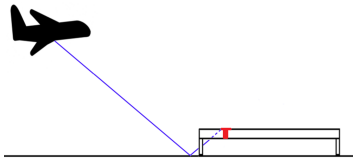

Figure 5.10: Schematic of a sound wave reflecting off the ground

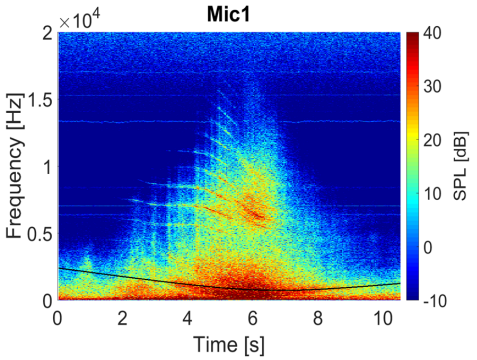

Figure 5.11: Spectrogram of the B737-800 with theoretical estimation of the ground effect

It is most likely that the multiple asymmetric lines for the ground effect are caused through edge diffraction. An example of this phenomenon is displayed in Figure 5.12. When edge diffraction is the cause, the ground effect is depended on the position of the microphone and the flight path of the aircraft. Only the microphones close to the edge and in flight direction of the aircraft will suffer from Lloyd's mirror reflection. This is exactly what happens in the spectrograms of the B737-800.

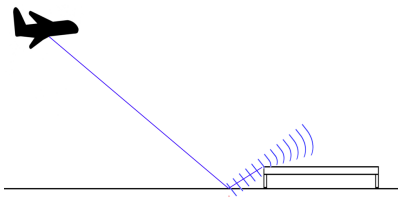

Figure 5.12: Edge diffraction of a sound wave on the acoustic camera

5.4. FREQUENCY BAND

The noise emitted by aircraft lies within a specific range of frequencies. This frequency band is important to know and is used to tune the acoustic camera. To be able to make an estimation of the frequency band of interest, the data from the Boeing B737-800 is evaluated. From its spectrogram (Figure 5.5) and Power Spectral Density (PSD) plot (Figure 5.13) the frequency band is set to be from 500 to 15000 Hz.

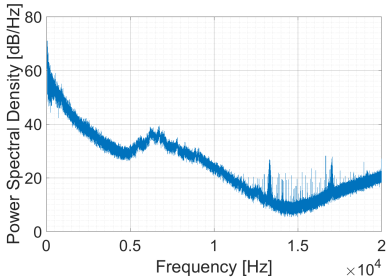

Figure 5.13: Power Spectral Density plot of the Boeing B737-800

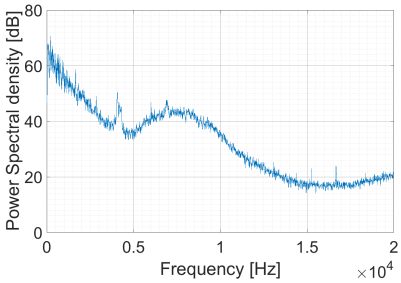

Figure 5.14: Power Spectral Density plot of the Airbus A321

The PSD plot of the B737-800 shows an increase of the signal above 15 kHz (Figure 5.13). This increase could be electronic or background noise. However it should have been filtered by an anti-aliasing filter (low pass filter). This phenomenon is examined to make sure it will not happen during the next measurement campaign.

Other aircraft measured with the same camera are evaluated to see if it was a measurement error or a problem within the system itself. Figure 5.14 shows the PSD plot of the Airbus A321. This plot has again an increasing signal above 15 kHz.

The anti-alias filter used during the measurements is a Sallen-Key filter. This filter can be the cause of the increase, while this phenomena is documented before for this type of filter [32]. However, while inspecting the general behaviour of a Sallen-Key filter, this phenomenon does not occur. The frequency response of a Sallen-Key filter with a 2^{nd} and 4^{th} order Butterworth filter is displayed in Figure 5.15. The cut-off frequency of this filter was set at 10 kHz. A low-pass filter is designed to block all frequencies above the cut-off frequency (stopband), while passing all frequencies below that (the passband) [33]. The cut-off frequency of the Butterworth filter is not completely sharp, but has a roll-off. It is designed to have the smallest roll-off without having a passband ripple and is commonly called the maximally flat filter [33]. The flat passband and the roll-off are visible in Figure 5.15, but the increase in high frequency is not there.

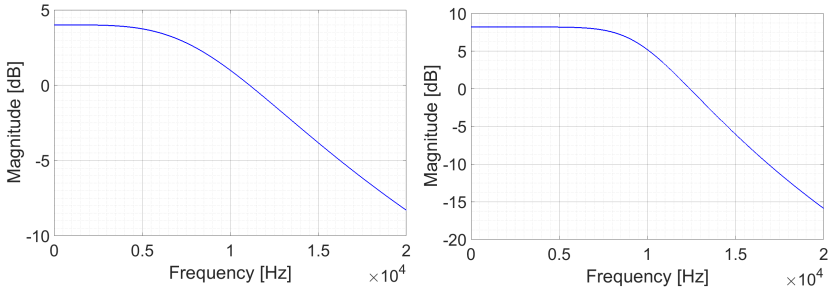

Figure 5.15: Frequency response of the Sallen-Key filter with a 2nd (left) and 4th (right) order Butterworth filter

A typical Sallen-Key filter should work fine for these kinds of measurements and no real problem can be pinpointed. It is possible that settings were wrong during the measurements. However, this information is not well documented and lost over time. This means that it is unknown what went wrong. The measurements carried out during this research are performed with a different data-acquisition system than the one used in the previous fly-over measurement campaign. The DAQ used during this research is from the ANCE section and is called camera 4. For the previous measurements the DAQ called camera 2 was used. Camera 4 uses a Sallen-Key Butterworth filter just like camera 2 and needs to be checked for this phenomenon. Figure 5.16 shows a PSD plot of a background measurement in the wind tunnel performed with camera 4. This plot does not show the increase in levels for the higher frequencies and it is expected the increase will not occur during the measurements at Schiphol.

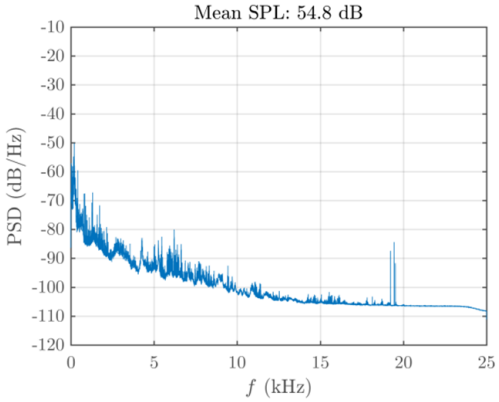

Figure 5.16: Power spectral density plot of an empty wind tunnel measurement with camera 4

6

DESIGN OF THE NEW ACOUSTIC CAMERA DEDICATED FOR FLY-OVER MEASUREMENTS

This chapter discusses the process of the design of the optimised acoustic camera. It starts with the general lay-out, which is chosen by a trade-off between configurations commonly used for fly-over measurements (Section 6.1). After this an array configuration is chosen and analysed in Section 6.2. The complete design of the acoustic camera is described in more detail in Section 6.3.

6.1. CONFIGURATION

Three basic configurations are commonly used for measuring fly-over aircraft. These configurations are displayed in Figure 6.1 and are:

1. Separate microphones attached to one structure
2. Separate microphones with their own holdings
3. All microphones attached to a plate

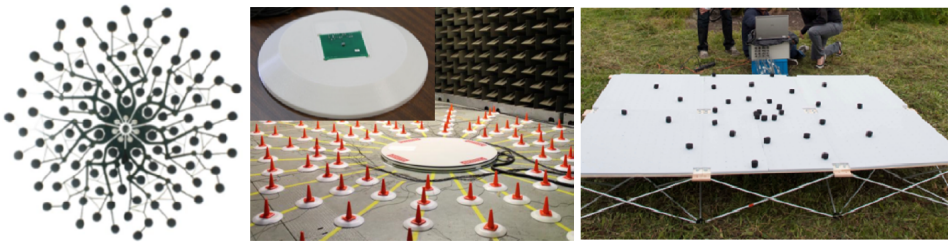

Figure 6.1: Configurations of acoustic cameras commonly used for fly-over measurements. FLTR: configuration 1, configuration 2 in general and with a zoom in on a separate microphone and configuration 3 [10, 31, 34]

To be able to pick the best construction a trade-off between all three configurations is made. This trade-off is displayed in Table 6.1 and is based on the Weighted Objectives Method (WOM). This method compares the configurations based on an overall score, which consist of a weighted sum of all the scores per criteria. The one with the highest overall score wins. The trade-off is made on costs, manufacturability, position accuracy, set-up, the ease of transportation and flexibility.

Configuration 1 is the most expensive, while it has a complicated construction made of expensive materials. It can be bought at 01dB [10] for 12-35k euro. Configuration 3 is the least expensive and is built with a total cost of 6232 euro [31]. There are no prices mentioned for configuration 2, but all separate microphone holders have to be made. This means more material and working hours are needed than for configuration 3 (till a certain size of the array configuration) and thus it will be more expensive.

In terms of manufacturability, configuration 1 is the best since this camera can be bought off the shelf. The hardest to manufacture will be configuration 2, since separate casings have to be made for all microphones.

For the position accuracy the most points are assigned to configuration 3. The construction is rigid and the microphones will always be in the exact same place. Configuration 1 also has a fixed position for all microphones. However, the construction is more flexible and can move when the wind is blowing. Configuration 2 has the least points, because there is no predefined configuration. It is difficult and time consuming to place the microphones for every measurement at the exact same position.

The set-up time for configuration 1 will be the shortest. Everything is already in place and just needs to fold out. Configuration 3 takes a bit more time since all plates need to be connected and the microphones placed. The longest set-up time is for configuration 2, since to position of each microphone has to be measured accurately for each experiment.

Configuration 2 will be the best to handle during transportation. It consists out of small components which can easily be stacked in a car. Configuration 1 folds into a packet which is easy to transport. Configuration 3 is the hardest to transport, while large rigid plates are used.

The measurement flexibility is best for configuration 2. Due to the separate microphones any configuration with desired aperture can be made. Configuration 1 is the worst since the microphones are fixed to the construction and cannot be adapted. Configuration 3 has been assigned 2 points since it has a rigid structure with fixed microphones, but the construction can easily be adapted.

The trade-off criteria are given a weight factor to make the most important one stand out. Only one array configuration is used for the optimised camera. This means the flexibility is in this case less important, but can be useful in the future. The position accuracy is the most important, since this was a main point of recommendation of the previous camera and will result in better measurement results. Adding all assigned points gives configuration 3 as the best option. This is especially due to the low costs, good manufacturability and the position accuracy. The transportation is harder due to the large plates used, but should be no problem when hiring a large van.

Table 6.1: Trade-off between configurations of acoustic cameras commonly used for fly-over measurements

Criteria	Weight	Config1	Config2	Config3
Costs	2	1	2	3
Manufacturability	2	3	1	2
Position accuracy	3	2	1	3
Set-up	2	3	1	2
Transportation	2	2	3	1
Flexibility	1	1	3	2
Total		25	20	**27**

6.2. MICROPHONE ARRAY

Chapter 2 describes a wide range of existing array configurations. The spiral arrays or optimised random arrays are concluded to be the best to use. The spiral arrays perform the best for a broadband frequency range while the random arrays are the best for an optimised frequency. For the Schiphol measurements the desired frequency band is from 500 to 15000 Hz [Chapter 5]. Because broadband frequencies are measured, there is no need to optimize an array for a specific frequency. This means that a spiral array is used. Chapter 2 mentions the Underbrink spiral as having the best overall performance, thus this array will be used for the optimised acoustic camera.

Array parameters need to be defined to determine the microphone positions within the Underbrink array. These parameters are the maximum and minimum radius of the array (Rd_{max} and Rd_0), the number of spiral arms (N_a), the number of microphones per spiral (N_m) and the spiral angle (ν). The Underbrink array places the microphones in the centre of equal area segments [9]. The radii of the microphones can be calculated with Equations 6.1 and 6.2 in which $m = 1, ..., N_a$ and $n = 2, ..., N_m$. With the radii known, the angles are calculated by placing each microphone along a log spiral on the multiple arms with Equation 6.3.

$$Rd_{m,1} = Rd_0 \tag{6.1}$$

$$Rd_{m,n} = \sqrt{\frac{2n-3}{2N_m-3}}\,Rd_{max} \tag{6.2}$$

$$\mu_{m,n} = \frac{ln(\frac{Rd_{m,n}}{Rd_0})}{cot(\nu)} + \frac{m-1}{N_a}2\pi \tag{6.3}$$

The microphones and data acquisition system called 'camera 4' of the ANCE section is used. This system consists out of 64 microphones. The aperture of the array is set to be 3.4 m (Chapter 5). Space is reserved for the optical camera in the middle of the array. To avoid edge diffraction affecting the microphones, they are placed at least 30 cm from the edge of the plate (Chapter 5). This gives plates of 4 x 4 m with a minimum array radius of 0.15 m and a maximum of 1.7 m. The spiral angle is set to $\frac{5\pi}{16}$ radians. To be able to fit all microphones evenly on the arms, the number of arms needs to be 4 or 8. More than 8 arms will give insufficient microphone spacing. To check which amount of arms works best, source plots of both configurations are simulated and displayed in Figure 6.2. Judging from these figures it is best to use the configuration with 8 arms due to the less clear presence of side lobes. Before deciding on this configuration, its manufacturability is checked. The microphones cannot be placed too close together to avoid them using up the same space or have a too thin construction in between. The diameter of the microphones is 10 mm, which means the drilled holes would be around 15 mm. To have a minimum of 2 cm of construction plate between the holes, the minimum distance between the centres of the microphones should be 3 cm. The minimal distance appearing in the configuration is 4.39 cm, which complies with the constraints.

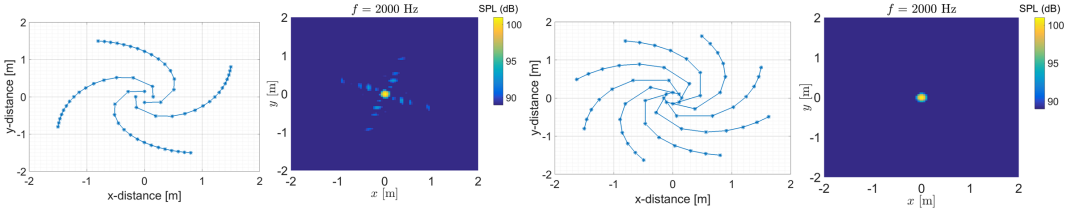

Figure 6.2: Underbrink spiral array with 4 and 8 arms together with their simulated beamform plots

A beamforming simulation is made to analyse the performance of the array. The frequency band of interest is between 500 and 15000 Hz and the beamform window is set to 50 x 50 m to fit an aircraft. For the steering vector, formulation 3 from the paper 'Three-Dimensional Acoustic Source Mapping with Different Beamforming Steering Vector Formulations' of E. Sarradj is used [35], which is displayed in Equation 6.4. In this equation $\vec{g_j}$ is the steering vector, f the frequency, N the number of microphones, $\vec{r}_{j,n}$ the distance from the microphone to the grid point, $\vec{r}_{j,0}$ the distance from the middle of the array to the grid point and c the speed of sound.

$$\vec{g_j} = \frac{1}{\vec{r}_{j,n}\,\vec{r}_{j,0}\sum_{j=1}^{N}\vec{r}_{j,n}^{-2}}\, e^{\frac{-i2\pi f(\vec{r}_{j,n}-\vec{r}_{j,0})}{c}} \tag{6.4}$$

First all frequencies are checked for a monopole source placed at position (0,0), which is displayed in Figure 6.3. In the figure the main lobe width decreases and the side lobe level increases with increasing frequency as expected (Chapter 4). The side lobe level increases, but stays low enough not to interfere with the main lobe. The position of the source stays in its exact location and the source can clearly be distinguished for all frequencies.

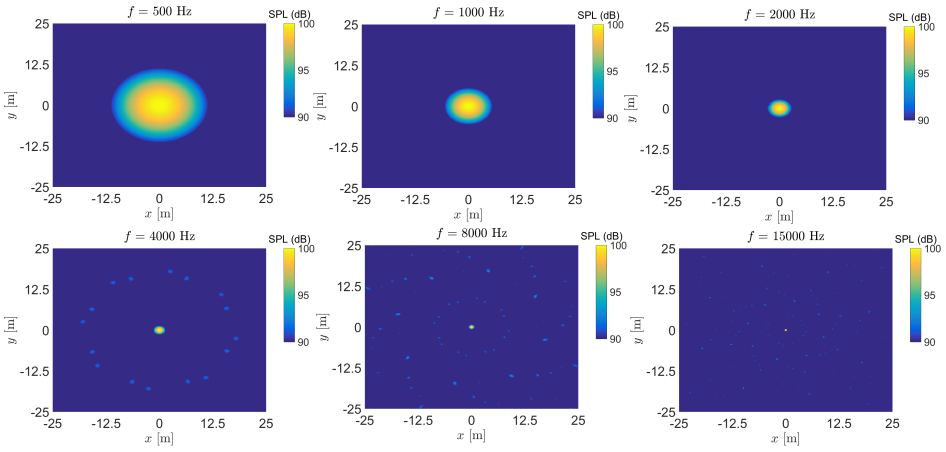

Figure 6.3: Simulated beamform plots of a monopole source at 500, 1000, 2000, 4000, 8000 and 15000 Hz, measured with an 8 arm Underbrink array

Next to a monopole source in front of the camera, it is also important to have more information about sources under an angle. The source is placed at 10 and 20 meter from the origin in the horizontal, vertical and diagonal direction. The simulated beamform plots of these positions at 2000 Hz are displayed in Figure 6.4. For the beamform simulation the same parameters as before were used. Comparing the sources under an angle, with the source in front of the camera, it can be seen that the positioning of the sources is exact, only the source is more stretched then before and side lobes appear. The stretching of the sources and the increased side lobes are as expected (Chapter 4). They do not interfere with the current results and the main source is still clearly visible with the exact sound pressure level and position.

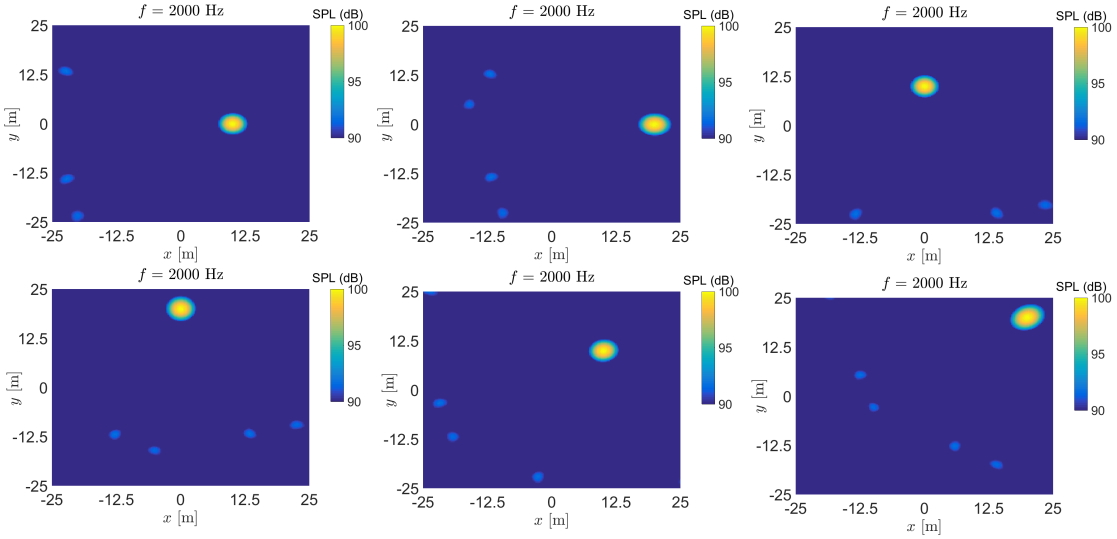

Figure 6.4: Monopole source with a horizontal, vertical and diagonal deflection

To see how the Underbrink array reacts to multiple sources, the main and nose landing gear of the Airbus A320 are simulated. This means that there are two sources approximately 4 m from the middle in the vertical direction (the main landing gear) and one source approximately 12.6 m in the horizontal direction (the nose landing gear) [36]. This is not a representative of the real beamform plot of the A320, due to the equal sound pressure level of the simulated sources. It aims to get an indication of the position of multiple sources and reaction to this of the Underbrink array. The simulated beamform plot is displayed in Figure 6.5. In this figure, the main sources can be distinguished and are simulated at their correct positions.

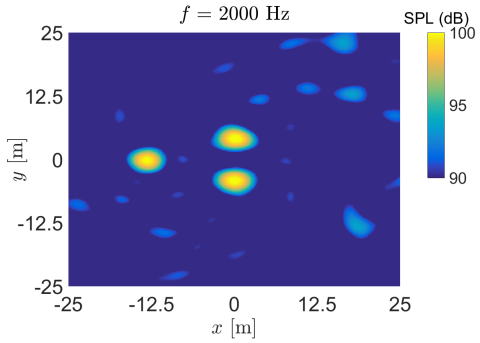

Figure 6.5: Simulated beamform plot of 3 monopole sources

As a final check also the Archimedean spiral, the Dougherty log-spiral and the Multi-arm spiral were analysed with the beamform simulation. The beamform plots are displayed in Figure 6.6 and compared to Figure 6.2. All arrays are simulated with 64 microphones, a minimum radius of 0.15 m, a maximum radius of 1.7 m and (if applicable) with 8 arms. The frequency selected is 2000 Hz. A 12 dB range is chosen for 100 scan grid points and with formulation 3 from Sarradj as steering vector [35]. Comparing all configurations in Figure 6.6 with the 8 arm Underbrink spiral (Figure 6.2), it is apparent that the main lobe width of all configurations is

approximately the same and that only the Underbrink spiral does not have any side lobes. This means that the Underbrink spiral array has the best simulated performance for a monopole source in front of the array.

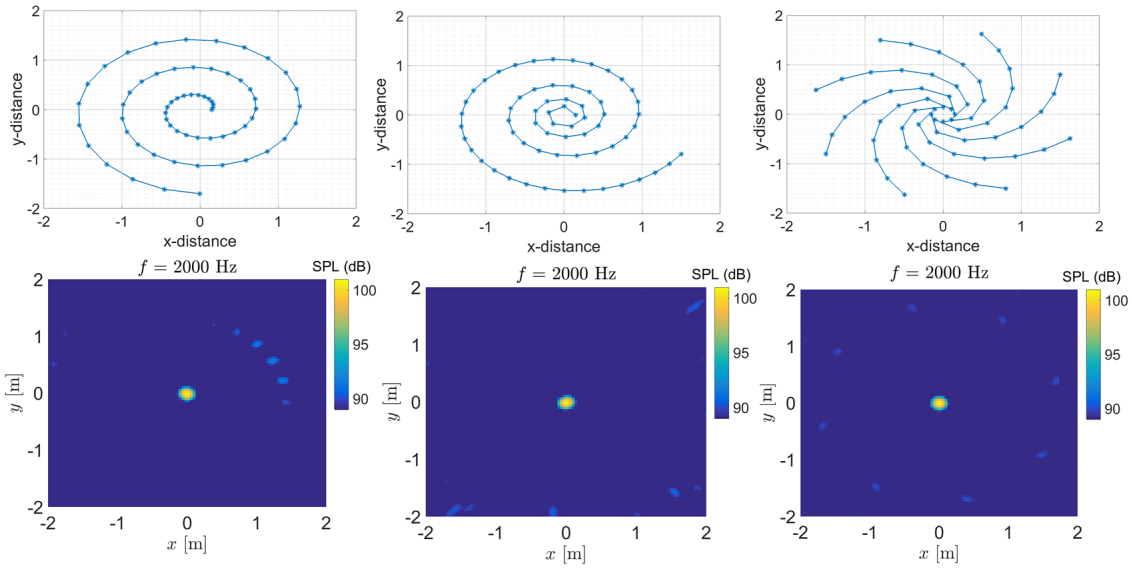

Figure 6.6: The Archimedean (left), Dougherty log- (mid) and Multi-arm (right) spiral configurations with their simulated beamform plot at 2000 Hz

6.3. DETAILED DESIGN

The optimised acoustic camera will be a design with all microphones fixed in a big plate configuration. The camera will have a size of 4x4m. This larger size is to improve the resolution. The camera must be detachable for easy transportation. The detachment must be easy, but still thorough for a good operability without losing structural strength and measurement accuracy. The data acquisition system (DAQ) of camera 4 is used together with its 64 microphones. The wires of the microphones have to be elongated before use. After elongation the microphones are calibrated.

The plating material of the acoustic camera must be strong, stiff, light, cheap and easy to manufacture. Multiplex complies with these criteria. The construction will be divided in 16 plates of 1 x 1 m to keep it operable. The thickness of the plates is 12 mm to provide enough stiffness. To check if the 1 x 1 x 0.012 m multiplex plates are stiff enough, the maximum deflection is calculated. This can be done with Equation 6.5 [37].

$$\delta_{max} = \frac{0.142p \cdot b^4}{E \cdot d^3[2.21(\frac{b}{l})^3 + 1)} = \frac{0.142 \cdot 60.26 \cdot 1^4}{8.4 \cdot 10^9 \cdot 0.012^3[2.21(\frac{1}{1})^3 + 1]} = 1.84 \cdot 10^{-4} m \tag{6.5}$$

In this equation the load on the plate is taken as the gravity on the plate and on the foam ($p = 9.81 \cdot 6 + 9.81 \cdot 0.1425 = 60.26N$). The Young's modulus ($E$) of multiplex is $8.4 \cdot 10^9 N/m^2$. The eventual deflection is less than 1 mm, which is acceptable.

The placement of absorption foam on top of an acoustic camera is a widely discussed topic within the field of research. Some researchers say it is best to use no foam and place the microphones flush mounted in the plate. This way the direct and indirect signals have the same length and the sound pressure is doubled (Chapter 2.5). This gives an increase of 6 dB for all frequencies which can easily be accounted for during the data analysis. However this only happens for ideal conditions. The microphones should be of a high quality and the wood a perfect reflector. This is not the case for these measurements. The reflections with and without foam are measured in Reference [31]. In their experiment the increase in sound pressure level was less than 6 dB for the plate without foam. When repeating the experiment approximately the same values were obtained. Without having the certainty of the 6 dB increase it is better to have the least influence as possible. This is achieved by placing foam on top of the plating material. For the previous camera elaborate tests were performed on sound absorption of different kinds of foam [31]. It was found that Flamex basic had the highest absorption coefficient. The thicker the foam, the better the performance. However, the difference between Flamex 50 mm and 15 mm is small, while there is a large price difference. For this reason Flamex GU

15 mm is used. The foam will be cut in pieces of 1 x 1 m and glued on top of the plating material.

The 16 big plates have to be attached to each other in such a way it can be easily operated. This will be achieved by using wooden support plates of 0.15 x 0.15 m. These plates can be made out of the left-over wood of the big plates (multiplex with a thickness of 12 mm). The support plates and the big plates will be fitted with a bolt and a winged nut. This way the support plates can be easily attached without the use of any tools. The support plates will overlap the big plates to connect them together as displayed in Figure 6.7. Figure 6.8 shows a schematic drawing of the support plate with the required holes and a striped square for the support structure. The support plate in the middle of the acoustic camera needs to have an extra hole for the optical camera. The plate is made larger (20 x 20 cm) with more space for the support structure for extra reinforcement in the middle of the array.

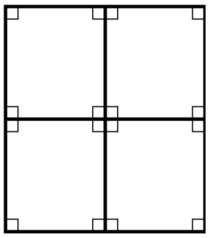

Figure 6.7: Concept of the big plates with support plates

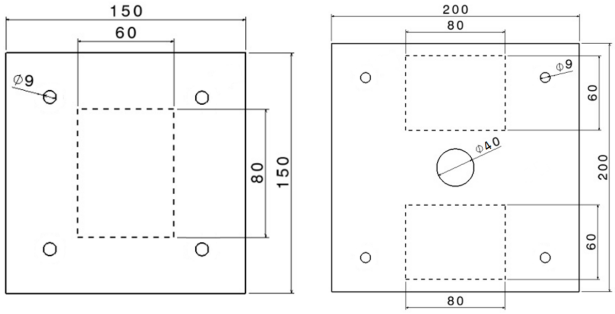

Figure 6.8: Schematic drawing of a general support plate (left) and the support plate placed in the middle of the camera (right)

The striped lines on the support plates in Figure 6.8 are for a support structure. This support structure will consist out of adjustable furniture legs. These legs will be attached to the support plates and will be present at the corners of each big plate. The small elevation given by these legs provides room for the microphone castings, cables and structural parts underneath the camera. The legs are adjustable so the plates can be set level, even when the floor is crooked. An example of the adjustable legs is displayed in Figure 6.9. The legs can carry a load of 125 kg, which is more than the weight of the construction.

In Section 6.2 it is decided to use an Underbrink spiral array for the microphone configuration. This array configuration has a good overall performance and works for broadband signals, which makes it perfect for imaging fly-over aircraft. The configuration is slightly rotated to avoid microphone placement on the edge of a plate. The configuration is displayed in Figure 6.10 with the big plates emphasized with black lines and the support plates with red lines.

Figure 6.9: Adjustable furniture legs

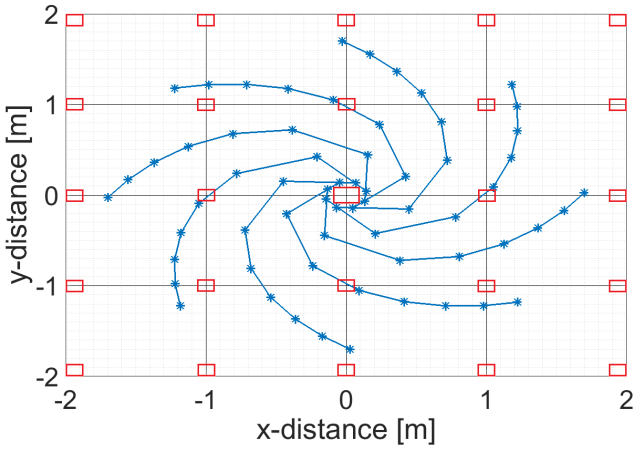

Figure 6.10: Underbrink spiral array configuration for 64 microphones

A high position accuracy is required for the microphone placement. The microphones will be kept in place by the hole in the wood and the foam. However, this still allows the microphones to move a little. The

best is to clamp the microphones with a clip placed below the holes in the big plates. This is done with a clothes pin. An example of this clamping structure is given in Figure 6.11.

A hole in the middle of the array configuration is made in which the optical camera can be placed. The optical camera can be placed on a platform made out of two corner pieces as is displayed in Figure 6.12. The camera will stay in place while the lens is clamped in the hole and ropes or elastic bands are attached to the structure to work as a belt.

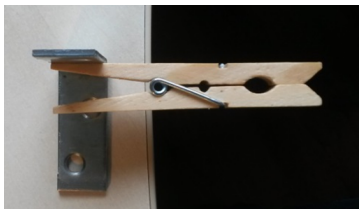

Figure 6.11: Clamping structure for the microphones

Figure 6.12: Structure holding the optical camera

Figure 6.13: Rough foam used as a wind shield for the microphones

Because the camera will be used outdoors, the weather conditions have to be taken into account. A wind shield is placed over the microphones to prevent the wind from interfering with the measured signal. Rough foam will be used as wind shield and is cut into circles and placed over the microphones as displayed in Figure 6.13. The rough foam was successful in tests for the previous fly-over camera [31]. This was verified with an extra experiment. For this experiment a vent was placed in front and on the side of the microphones. When the vent was close to the microphones, the frequency emitted could hardly be measured without using wind shielding, but could be measured with using the rough foam (Figure 6.14). To receive the best signal and minimize wind induced noise the rough foam wind shielding is used.

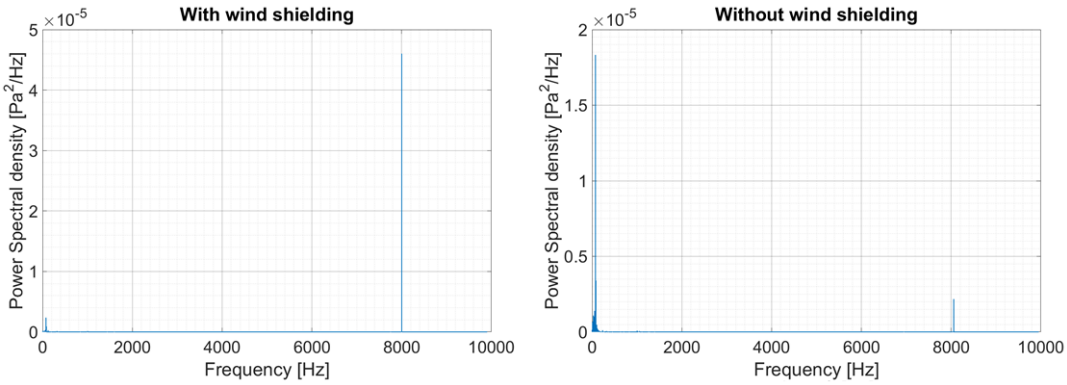

Figure 6.14: PSD plots at 8000 Hz measured with (left) and without (right) wind shielding

The design is built at the flight hall of Aerospace Engineering at the TU Delft. The complete building process with the verification of the design is presented in Appendix A.

7

MEASUREMENTS SCHIPHOL

The acoustic camera will be verified with a fly-over measurement campaign. To be able to measure aircraft at a relative low height, the experiment had to be performed near an airport. Airports in the vicinity of Delft are Rotterdam The Hague Airport and Schiphol Airport. Schiphol Airport is chosen for these measurements, due to the higher variety in aircraft type and more aircraft movements per hour. The first measurement campaign was carried out at the 14^{th} of August. The portable batteries broke down during this campaign and only a few aircraft could be measured. For this reason an extra measurement campaign was carried out on the 16^{th} and 17^{th} of October. The measurement campaigns are described in this chapter. The chapter starts with the selection of the site and its conditions (Section 7.1). After this the used tools and its settings are presented (Section 7.2). The chapter closes with notes on the measurements itself and a list of the measured aircraft (Section 7.3).

7.1. LOCATION

The acoustic camera was placed in the extension of one of the runways of Schiphol to ensure a straight fly-over and a minimum distance between the aircraft and the camera. This position also ensures approximately the same measurement conditions for all aircraft, since they will follow the same flight track. Aircraft taking-off can deviate slightly with their flight track, depending on their destination. The flight tracks of landing aircraft will be the same, since they will follow the Instrument Landing System (ILS) at their approach and are aiming for the same touch down zone. This gives a preference for measuring landing aircraft over aircraft taking-off. A more important benefit of measuring landing aircraft has to do with the main noise sources. During take-off the engine is set at maximum thrust settings, resulting in the engine as the dominant noise source. For landing aircraft the engine is less dominant and airframe noise can be measured as well.

Schiphol has six runways which are displayed in Figure 7.1. The Oostbaan will not be considered for the measurement campaign. It has a short runway and is only in use by small aircraft, like private and business jets. Positions 09, 24 and 36C indicated in Figure 7.1 cannot be used while this is no public area. Positions 36L and 18L are also off the table, because the runway is closed for landing in this direction. The measurements will be carried out when the weather conditions are good. This means that there is no rain, the temperature is below 30 degrees and the wind speeds are maximal 4 Beaufort. The Buitenveldertbaan is only used during strong winds from the west. This situation will not occur during the measurements, which means position 27 will not be used. This leaves positions 18R, 18C, 06 and 36R as potential locations. From these locations position 06 is the least ideal, while it is close to a busy highway and has high background noise levels. Positions 18R and 18C can be used for aircraft landing in southern directions and position 36R for aircraft landing in the northern direction.

The preferred location of the acoustic camera is dependent of the usage of the runways, which is dependent on the weather conditions. Schiphol has certain preferred runways for take-off and landing (Figure 7.2). This preference is to make sure the traffic streams avoid densely populated areas and minimize the noise experienced on the ground. The preferences can be used as an indication of the potential measurement location on the day of the measurements, but are not set in stone.

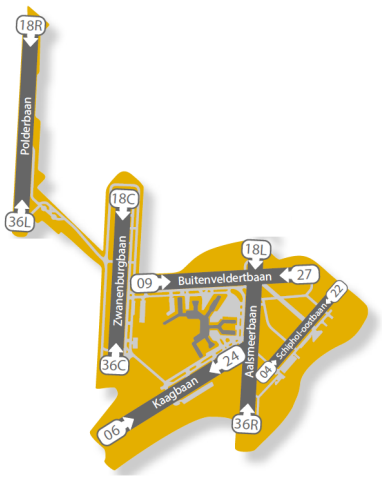

Figure 7.1: Runways of Schiphol Airport [38]

Periode 06:00 - 23:00 uur

Preferentie	Landen		Starten	
	L1	L2	S1	S2
1	06	(36R)	36L	(36C)
2	18R	(18C)	24	(18L)
3	06	(36R)	09	(36L)
4	27	(18R)	24	(18L)
5a	36R	(36C)	36L	(36C)
5b	18R	(18C)	18L	(18C)
6a	36R	(36C)	36L	(09)
6b	18R	(18C)	18L	(24)

Zichtcondities: goed
- zicht tenminste 5.000 m
- wolkenbasis tenminste 1.000 voet
- in daglichtperiode (UDP)

Zichtcondities: goed
- zicht tenminste 5.000 m
- wolkenbasis tenminste 1.000 voet

Zichtcondities: goed of marginaal
- zicht tenminste 1.500 m
- wolkenbasis tenminste 300 voet

Figure 7.2: Runway preference of Schiphol [38]

Apart from the position relative to the runway, it is also important that the acoustic camera will be placed on a level surface in an open area. The level surface is important for the position accuracy when beamforming the data afterwards. A slight deviation is acceptable since the legs of the camera can be adjusted. An open area is preferred to minimize reflections of the sound signal. The camera has to be placed on a public area which can be reached by car. Position 18R does not have an open area near the runway which can be reached by car and is therefore not considered suitable.

This leaves two locations which can be used for the fly-over measurements. These are at position 18C (when the wind is coming from the south) and position 36R (when the wind is coming from the north). A site at position 18C and at 36R which fulfils all requirements is displayed in Figure 7.3. The site of 36R lies approximately 1200 m from the ILS transmitter. The standard glide slope of an ILS is three degrees, which gives a fly-over height of 63 meter. The site for position 18C lies approximately 950 m from the ILS transmitter. Assuming the standard glide slope of three degrees, gives a fly-over height of 50 meter. On the days of the measurements the wind was coming from the south and position 18C was used to set-up the acoustic camera.

Figure 7.3: Measurement location at 36R (left) and at 18C (right)(36R: 52°16′59.7″N4°46′35.9″E, 18C: 52°20′ 13.7″N4°44′25.8″E)

7.2. EQUIPMENT AND SETTINGS

This section describes the equipment, settings and conditions during the measurements. First of all the acoustic camera itself is used which consist out of 16 big plates, 25 support plates and 100 screws and winged nuts. 64 microphones are positioned in the plates and connected to the data acquisition system (DAQ) called Camera 4. Information on this system is displayed in Table 7.1. The DAQ is attached to a laptop with LabVIEW software and a power output. The LabVIEW software is developed by National Instruments Corporation and functions as a user interface to control the instruments, provide real-time visualization of the recorded data and store the data. The power output is an external battery (Yucel Y7-12 used in August and Ultracell UL7-12 used in October). The laptop used is a HP Elitebook 8560w and can perform 3 hours on its internal battery. For a longer duration the laptop can be charged with a car charger (Voltcraft NPI 150-12/NPI150-24) or a

power bank (Xtorm AL390). To make sure there is enough storage space for all data an external hard drive is used (Western Digital: My passport ultra. 2TB).

Table 7.1: Information on the data acquisition system: Camera 4 [39]

Item	Value
Microphones	
Model	PUI AUDIO 665-POM-2735P-R
Number of microphones	64
Length	60 mm
Diameter	15 mm
Cable length	Varying from 3.4-5 m
Data logging	
Sample Frequency	50 kHz
Frequency Range	0.2 – 25 kHz
Microphone Crosstalk	-45 dB
High Pass Filter -3dB	170 Hz
Low pass filter -3dB	40 kHz
Maximum sound pressure level	
Low Amplification	122 dB
High Amplification	105 dB
Settings	
Amplification	Low amplification
Distance to source	50 m

The sampling rate of the experiment was 50 kHz as mentioned in Table 7.1. This rate has to be at least twice the highest frequency of interest according to the Nyquist Theorem. A band limited analogue signal can be perfectly reconstructed by following this theorem. If the sampling rate is too low, the signal will be aliased. A passband filter is applied to keep only the frequencies of interest (the aircraft noise). All frequencies outside the filter range are eliminated. The passband filter of this system is from 170 – 40000 Hz as displayed in Table 7.1. In Chapter 5, the frequency band of interest is determined to be from 500 to 15000 Hz. The band of interest lies within the passband filter and the maximum frequency is less than half the sampling rate. This means the data acquisition system is capable of obtaining the desired signal.

7.2.1. OPTICAL CAMERA

The optical camera is used during the data analysis for matching the source plot with the aircraft and for the determination of the aircraft position. The optical camera is placed in the middle of the acoustic camera and is connected to the same laptop as the DAQ and controlled with the LabVIEW software. The specifications of the camera are displayed in Table 7.2 together with its settings during the experiment.

Table 7.2: Specifications and settings of the optical camera [39]

Item	Value
Specifications	
Manufacturer and model	Datavision UI-1220LE
Lens	Kowa LM4NCL
USB cable length	5m
Resolution	752x480
Max frame rate	87 Hz
Settings	
Frame rate	30 Hz
Exposure Time	0.1 ms
Master Gain	1 on day 1 and 0.1 on days 2 and 3
Image Dimension	480 x 752
Bits	8
Actual FPS	30

7.2.2. ENVIRONMENTAL CONDITIONS

An environmental sensor is attached to the same laptop as the DAQ and controlled with the LabVIEW software to measure the temperature, humidity and air pressure. The environmental data from the KNMI is used [40] for verification. This institute delivers their weather forecast to Schiphol and is certified with the ISO 9001:2008 norm. The specifications of the environmental sensor and the weather conditions during the measurements are displayed in Table 7.3.

Table 7.3: Specifications of the environmental sensors [39] and the weather conditions

Item	**Value**		
Environmental sensors			
Sample Frequency	GPS – 1Hz, Other – 0.4 Hz		
Data Acquisition System	Arduino Micro		
GPS	Adafruit Ultimate GPS breakout board		
Tilt and Rotation	LSM303 Triple-axis Accelerometer-Magnetometer		
Humidity and Temperature	AM2302 Temperature-Humidity sensor		
Weather conditions			
	Day 1	**Day 2**	**Day 3**
Temperature	24.4 °C	18.2 °C	12.9°C
Humidity	75%	81%	82%
Wind speed	2.8 m/s	4.5 m/s	3.8 m/s
Direction of the wind	South East (118°)	South (184°)	South West (218°)
Air Pressure	101.85 kPa	101.89 kPa	101.94 kPa

7.2.3. AIRCRAFT INFORMATION

Information on the fly-over aircraft is needed for the data analysis. The aircraft type is required to match the identified noise sources to an aircraft. The fly-over height is needed to account for the atmospheric propagation effects. The Doppler effect can be accounted for by knowing the speed of the aircraft relative to the acoustic camera. While knowing the flight track of the aircraft, the noise sources can be accurately displayed with a sound source map on the fly-over aircraft. All this information is measured in two ways: with the help of the optical camera and with an ADS-B (Automatic Dependent Surveillance-Broadcast) receiver. Flightradar24.com is used for verification.

The optical camera is placed in the middle of the acoustic camera and looks straight up. The aircraft flies through its viewing window from which the aircraft height and speed can be determined. The developers of the AcoustiCam calibrated the camera using the Camera Calibration Toolbox for Matlab [41]. The calibration resulted in an intrinsic parameter matrix (Equation 7.1) from which the focal lengths (in pixels) are obtained.

$$Ac = \begin{bmatrix} FL_x & \gamma & u_0 \\ 0 & FL_y & v_0 \\ 0 & 0 & 1 \end{bmatrix} = \begin{bmatrix} 644.9019 & 0 & 240.6257 \\ 0 & 634.2610 & 400.1048 \\ 0 & 0 & 1 \end{bmatrix} \tag{7.1}$$

Within Equation 7.1, Ac is the Intrinsic parameter matrix, FL_x the focal length in x-direction, FL_y the focal length in y-direction, γ the skew coefficient, u_0 the 1st coordinate of the principal point and v_0 the 2nd coordinate of the principal point.

The height (H) of the aircraft can then be calculated with Equation 7.2. In this equation the wingspan in meters ($wingspan_m$) is divided by the wingspan in pixels ($wingspan_p$) and multiplied by the focal length in the y-direction (FL_y). dY is the pixel to meter ratio in the y-direction. The pixel to meter ratio in x-direction (dX) can be calculated with Equation 7.3.

$$H = FL_y \frac{wingspan_m}{wingspan_p} = FL_y dY \tag{7.2}$$

$$dX = \frac{H}{FL_x} \tag{7.3}$$

The aircraft velocity (V) can be calculated by the displacement of the aircraft over the pictures taken with the camera as displayed in Equation 7.4. In this equation dt is the number of frames used divided by the frame rate.

$$V = \frac{\sqrt{dX^2 + dY^2}}{dt} \tag{7.4}$$

The ADS-B system measures all data on-board of the aircraft itself. The aircraft determines its position using the Global Navigation Satellite System in combination with the Internal Navigation System. The position data together with the aircraft ID and altitude is sent to the ground by an ADS-B transponder. An ADS-B receiver on the ground can pick up this signal and save all data. The ADS-B receiver from the TU Delft is used with its specifications displayed in Table 7.4.

Table 7.4: Specifications of the ADS-B receiver [39]

Item	**Value**
Manufacturer and model	GNS 5890 ADS-B Receiver USB Stick
USB dimensions	61 x 27 x 9 mm
Receiving frequency	1090 MHz
Range	300 km

The data obtained from the ADS-B receiver and the optical camera do not always match. One of the systems has to be chosen to determine the height and velocity of the aircraft for the data analysis. The ADS-B data and the optical camera both have their pros and cons. The benefit of the optical camera is that it is recorded simultaneously with the acoustic data with 30 frames per second. This ensures that the height and velocity at a specified time can be obtained. The disadvantage is the accuracy. The pictures can be blurry, which makes it hard to specify a certain point on the aircraft. The disadvantage of the ADS-B system is that data is received every second. Sometimes the signal cannot be received correctly and seconds are missing from the data file. This makes it hard to specify the data for a specific time. The benefit is the long recording time. With the optical camera only data from the aircraft overhead can be obtained while de ADS-B system also has data when the aircraft is approaching and leaving the camera.

The data from the ADS-B system and the optical camera are compared and checked with the expectations to decide which data to use for the analysis. When evaluating the ADS-B data, the height appeared to be negative for the landing aircraft. The height obtained with the optical camera was around 60 m for landing aircraft, which approximately matches the 3 degree glide slope till the ILS transmitter. The values of the optical camera are the most realistic and are used in the analysis. The velocities of the optical camera and the ADS-B data lie close together and are both realistic. For the spectrogram analysis the velocity of the ADS-B data is used, due to the known frequency over time and good match with the Doppler effect. For the beamform analysis the velocity of the optical camera was used due to the known velocity in x- and y-direction and good match of the beamform plots with the pictures of the optical camera.

7.3. MEASUREMENT

The measurements were carried out on the 14^{th} of August and the 16^{th} and 17^{th} of October. During the measurements on the 14^{th} of August not all went as planned, which made it necessary to do an additional measurement campaign. This campaign was spread out over two days to capture as much aircraft as possible. The measurement set-up is displayed in Figure 7.4.

Figure 7.4: Set-up of the Schiphol measurements

The first measurement campaign was restricted by failure of the portable batteries. The Yucel battery appeared to be over its expiration date and worked for 1 minute before it died out. The Voltcraft car charger wasn't as good as expected and could not give enough power. The Xtorm power bank worked fine, but got overheated due to the high temperatures. These battery problems made the measurements difficult and restricted the measurement time and measured aircraft. For the measurements in October a replacement was bought for the Yucel battery (the Ultracell UL7-12), which powered the acoustic camera during the entire measurement campaign. The Xtorm battery was used to power the laptop inside the van (where it was a bit cooler), when no aircraft were using the runway. On the 17^{th} of October, the Xtorm battery also worked outside of the van due to the lower outside temperature and lack of sunlight heating the battery.

A weak point in the design of the camera appeared to be the pins. While the pins are strong enough to keep the microphones in position, they easily de-attached by a high pressure during transport and set-up. Duct tape was used as extra reinforcement for the second measurement campaign. When the glue band broke, the pins would still be attached. However, they were more loosely fitted, which causes a small decrease in microphone position accuracy. For next measurements it would be good to have an even stronger bond between the pins and their angles plates by using split pins for instance.

During the first measurement campaign in August both landing and take-off aircraft were measured. This was due to a runway change of Schiphol. Halfway through the day Schiphol decided to let aircraft take-off on the Zwanenburgbaan instead of landing, as was the case in morning. During the whole day 10 landing aircraft and 9 take-off aircraft were measured. The measurements in October had fewer difficulties and resulted in 153 measured aircraft. Not all aircraft have matching ADS-B data. This is due to the absence of an ADS-B emitter in some aircraft and difficulties in connectivity of the ADS-B receiver. A part of the aircraft without ADS-B data could be identified with the use of flightradar24.com and pictures taken. The landing aircraft which could be identified over the three measurement days are displayed in Table 7.5. The table shows the type of aircraft and the amount of measurements available. The complete data set of all aircraft with their specifications is displayed in Appendix C.

Table 7.5: Landing aircraft measured

Aircraft type	**Amount**	**Aircraft type**	**Amount**
A319	4	B737	66
A320	13	B747	1
A321	4	B777	9
A330	1	B787	8
A380	2	CRJ-900	2
Avro RJ85	3	CRJ-1000	1
ERJ-175	16	Fokker 70	7
ERJ-190	23		
ERJ-145	1	**Total**	**161**

8

CORRECTIONS

This chapter discusses the corrections required on the data measured at Schiphol Airport. The corrections are explained through a spectrogram analysis. For this analysis the data of the landing Boeing B747 (measurement 22 of 17 October) is used. The chapter starts with a display of the spectrogram without corrections and one with the background noise in section 8.1. After this, the effects of forward motion are explained in Section 8.2. Section 8.3 shows the Doppler effect on the signal and section 8.4 the atmospheric effects. The chapter closes with section 8.5 describing the influence of the ground effect.

8.1. BACKGROUND NOISE

A spectrogram is a two-dimensional function which visualises the amplitude of the received signal versus the frequency over a period of time. The spectrogram belonging to measurement 22 (of 17 October) of a landing Boeing B747 is displayed in Figure 8.1. The signal displayed is measured by microphone 1A of the acoustic camera. The signal received has to be corrected to get the emitted signal. This correction starts with the background noise. The sound signal measured consists out of the sound emitted by the aircraft and the background noise. An empty measurement was executed (a measurement without any flyover) to get an idea about the influence of the background noise. The spectrogram of the background noise is displayed in Figure 8.2. The background noise is minimal and only occurs at low frequencies. All frequencies below 30 dB are removed to delete the background noise from the spectrogram. Figure 8.3 displays the spectrogram without the background noise.

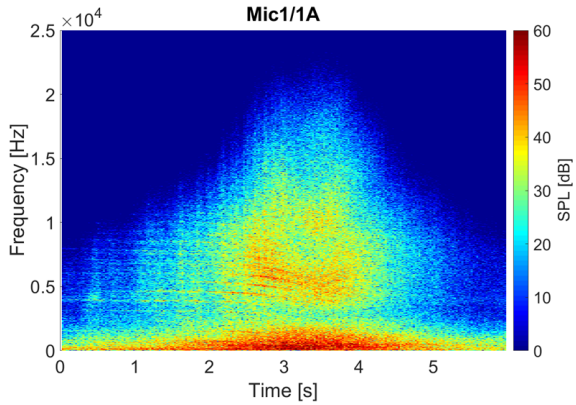

Figure 8.1: Spectrogram of a B747 (measurement 22, October 17)

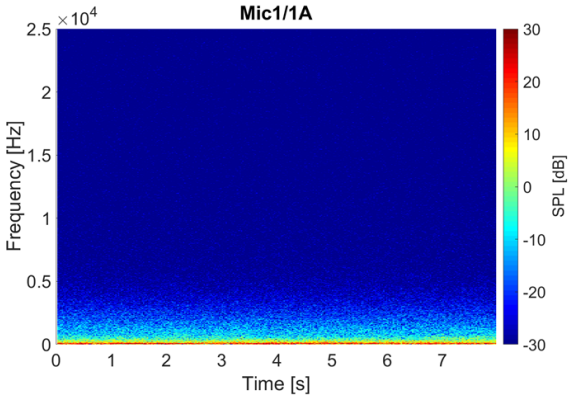

Figure 8.2: Spectrogram of background noise

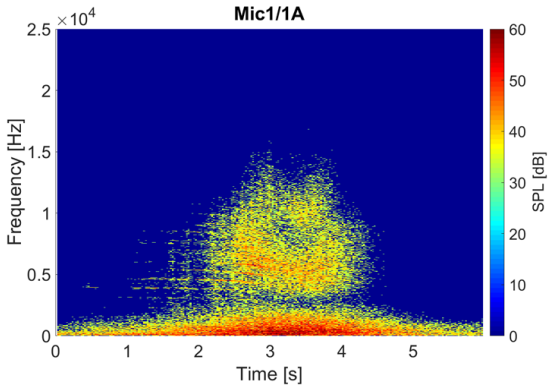

Figure 8.3: Spectrogram of a B747 (measurement 22, October 17) without signals below 30 dB

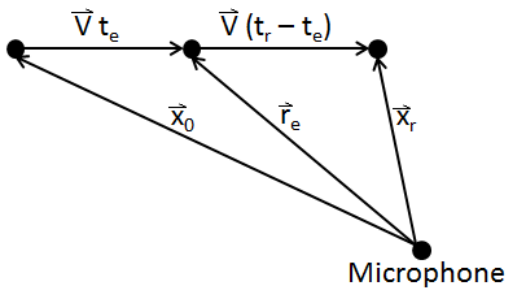

Figure 8.4: Source-receiver geometry

8.2. EFFECTS OF FORWARD MOTION

The aircraft measured is a moving source which needs to be corrected for the effects of forward motion. Due to the forward motion of the aircraft, the time at which the sound is received (t_r) is not the same as the time at which the sound is emitted (t_e). The source receiver geometry is visualised in Figure 8.4. Within the figure $\vec{x_0}$ is the initial position vector, $\vec{r_e}$ the distance to the source at the time of emission, $\vec{x_r}$ the distance to the source when the signal is received and $\vec{V}$ the velocity of the aircraft. The time delay can be calculated with Equation 8.1, in which c is the speed of sound.

$$t_r - t_e = \frac{||\vec{r_e}||}{c} \tag{8.1}$$

There are two unknowns in the equation (t_e and $\vec{r_e}$), which can be solved with the help of Figure 8.4. From the figure an expression for $\vec{r_e}$ is found, which can be used in Equation 8.1 and gives Equation 8.2.

$$t_r - t_e = \frac{||\vec{x_0} + \vec{V}\,t_e||}{c} \tag{8.2}$$

The position vector when the signal is received can be calculated with Equation 8.3.

$$\vec{x_r} = \vec{x_0} + \vec{V}\,t_e + \vec{V}\,(t_r - t_e) = \vec{x_0} + \vec{V}\,t_r \tag{8.3}$$

Equation 8.3 can be rewritten for $\vec{x_0}$ and substituted in Equation 8.2, which gives Equation 8.4.

$$t_r - t_e = \frac{||\vec{x_r} - \vec{V}\,(t_r - t_e)||}{c} \tag{8.4}$$

Squaring and rewriting Equation 8.4 will lead to Equation 8.5. This equation can be rewritten in quadratic form as displayed in Equation 8.6.

$$c^2(t_r - t_e)^2 = ||\vec{x_r}||^2 + ||\vec{V}||^2(t_r - t_e)^2 - 2\vec{x_r}\,\vec{V}\,(t_r - t_e) \tag{8.5}$$

$$(c^2 - ||\vec{V}||^2)(t_r - t_e)^2 + 2\vec{x_r}\,\vec{V}\,(t_r - t_e) - ||\vec{x_r}||^2 = 0 \tag{8.6}$$

Solving Equation 8.6 for the time delay $(t_r - t_e)$ results in Equation 8.7.

$$t_r - t_e = \frac{-\vec{x_r}\,\vec{V} \pm \sqrt{(\vec{x_r}\,\vec{V})^2 + (c^2 - ||\vec{V}||^2)||\vec{x_r}||^2}}{c^2 - ||\vec{V}||^2} \tag{8.7}$$

By knowing the time delay, the distance to the aircraft at the time of emission can be found with Equation 8.1. All fly-over aircraft are measured near a runway, so their speed is subsonic. This means that the time delay is positive and only the positive sign in the numerator of Equation 8.7 is used to obtain positive real values for $||\vec{r_e}||$.

8.3. DOPPLER EFFECT

All moving sound sources are influenced by the Doppler effect. This Doppler effect is the change in frequency due to the relative speed difference of the receiver and the observer. When a sound source is moving towards the receiver, sound waves are compressed and the received frequency is higher than the emitted frequency. Similarly, when a sound source moves away from the receiver, the received wavelength is larger and the received frequency is lower than the emitted frequency. This effect is present in the fly-over measurements and is visible in the spectrogram as lines with frequency varying with time. The ratio between the observed frequency and the frequency emitted is the Doppler factor and can be calculated with Equation 8.8.

$$\frac{f'}{f} = \frac{1}{1 - Mcos\theta} \tag{8.8}$$

In this equation f' is the observed frequency, f the emitted frequency, M the Mach number and θ the angle between the flight path of the aircraft and the direct path of the sound to the receiver as shown in Figure 8.5.

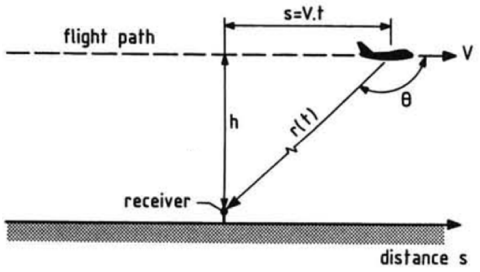

Figure 8.5: Geometry of the flight path of an aircraft [19]

Figure 8.6 visualises the Doppler effect. The Doppler shifted frequency is displayed over the spectrogram of Figure 8.1 with black striped lines. The angle and the Mach number are derived from the ADS-B data of the aircraft.

The Doppler shift must be eliminated from the spectrogram for further analysis of the data. This can be achieved by adapting the spectrogram with the time difference calculated with Equation 8.1. This adoption straightens the lines of the Doppler shift as displayed in the spectrogram of Figure 8.7.

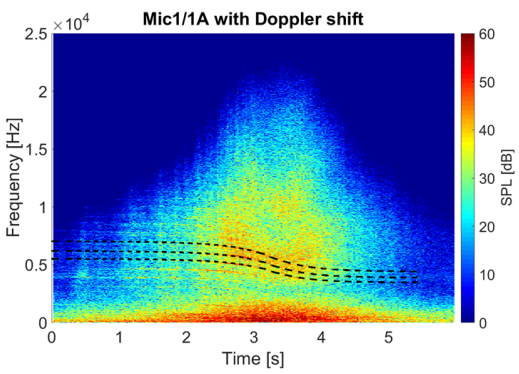

Figure 8.6: Display of the Doppler effect in the spectrogram of a B747 (measurement 22, October 17)

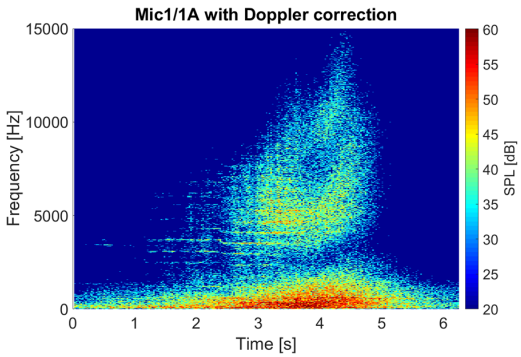

Figure 8.7: Spectrogram of a B747 (measurement 22, October 17) modified for the Doppler shift and without background noise

8.4. ATMOSPHERIC EFFECTS

The sound emitted by a non-directional sound source spreads out over an increasingly larger surface at increasing distances from the source. To be able to correct for this geometrical spreading the inverse-distance law can be used, which is given by Equation 8.9. This law states that the reduction in sound pressure level attributable to the spherical divergence is equal to 6 dB for each doubling of the distance [19]. Figure 8.8 shows the sound loss due to geometrical spreading with reference distance $r_1 = 1m$.

$$SPL(r_1) - SPL(r_2) = 20log(\frac{r_2}{r_1}) \tag{8.9}$$

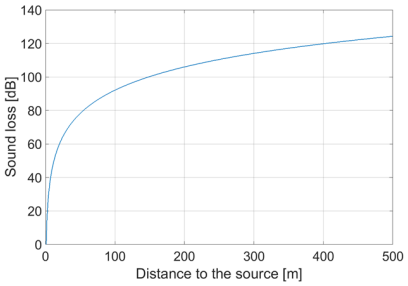

Figure 8.8: Loss in SPL due to geometrical spreading with $r_1 = 1m$

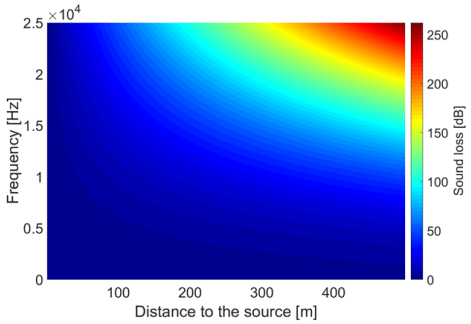

Figure 8.9: Loss in SPL due to sound attenuation with $r_1 = 1m$

Apart from geometrical spreading, part of the sound will be absorbed travelling through the atmosphere. Internal friction of atmospheric air causes this absorption. The rate of the sound absorption is expressed by the sound attenuation coefficient (α in [db/m]) and the decrease of sound pressure level can be calculated with Equation 8.10.

$$\Delta SPL = \alpha(r_2 - r_1) \tag{8.10}$$

The sound attenuation coefficient is dependent on the frequency of the sound, the air temperature and the amount of water vapour in the atmosphere. The calculations for this coefficient are provided in Appendix D. The sound attenuation is especially high at the higher frequencies as displayed in Figure 8.9.

Combining the geometrical spreading with the sound attenuation results in Equation 8.11. This equation can be used to calculate the sound pressure level at a distance of 1 meter. The spectrogram including the correction for the atmospheric effects and the Doppler effect is displayed in Figure 8.10.

$$SPL(r_1 = 1m) = SPL(r) + 20log(r) + \alpha \cdot r \tag{8.11}$$

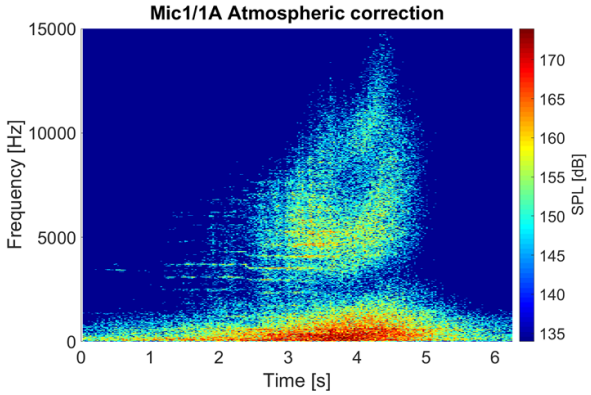

Figure 8.10: Spectrogram of a B747 (measurement 22, October 17) corrected for the atmospheric effects and the Doppler effect without background noise

8.5. GROUND EFFECT

The ground effect is discussed in in Chapter 2 and 5. This effect shows itself in the spectrogram through parabolic lines (Lloyd's mirror reflection). In the analysis of the previous fly-over camera it became apparent that the influence of the ground effect on the results was dependent on the position of the microphones. The microphones near the edge of the construction and in the flight direction of the aircraft had the most fringes due to edge diffraction. To prevent this at the optimised camera all microphones were placed at least 30 cm from the edge. The spectrogram of microphones 2H, 4H, 6H and 8H are analysed to see if this design choice worked out. These microphones are closest to the edge at each side of the camera and their spectrograms

are displayed in Figure 8.11. Microphone 1A lies in the middle of the camera and is used as reference. The spectrogram of this microphone is displayed in Figure 8.1. The spectrograms are not corrected. The ground effect is hardly visible in Figure 8.11, especially when comparing these spectrograms to the spectrograms of the B737 measured with the previous fly-over camera (Figures 5.8 and 5.9). The same absence of Lloyd's mirror reflection is discovered in all other measurements. The microphones at the edges are not influenced by the edge diffraction of the sound waves and the design choice can be considered successful.

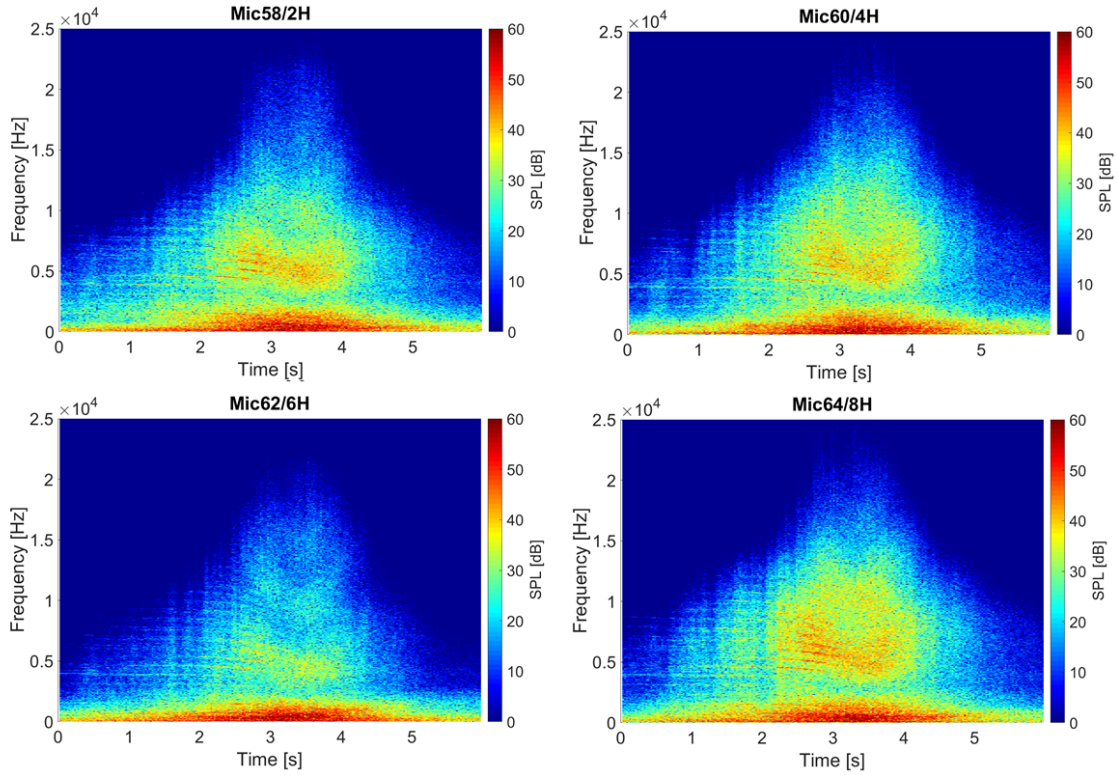

Figure 8.11: Spectrogram of a B747 (measurement 22, October 17) with microphone 2H, 4H, 6H and 8H

9

BEAMFORM ANALYSIS

Beamform plots are made to determine the performance of the new acoustic camera. Chapter 2 discusses the connection between the resolution of the beamform pictures and the diameter of the array through Rayleigh's criterion. An increased resolution can be obtained by decreasing the distance to the source or increasing the aperture of the array. The aperture of the previous fly-over camera is 1.7 m, the new camera has doubled this to 3.4 m. Section 9.1 compares the beamform results from the previous measurements [42] with the current beamform results to check if this increase has indeed improved the resolution.

9.1. RESOLUTION

The array's resolution can be calculated by the Rayleigh criterion (Equation 9.1) and is plotted in Figure 9.1 for the previous and the new acoustic camera.

$$R = 1.22\frac{h \cdot c}{D \cdot f} \tag{9.1}$$

When two noise sources are separated by a distance which lies below the line in the figure, they cannot be distinguished as separate sources. The line shifts downward when increasing the aperture, which results in an increase in resolution. It was difficult to distinguish the main landing gear and the engines of small aircraft for the previous fly-over camera. With the increase in aperture, this should be easier for the new camera. The closest distance between the main landing gear and the engines of four different aircraft are researched to evaluate the ability of the acoustic camera to separate the engine noise from the airframe noise. The four aircraft chosen have three different sizes with two aircraft of the smallest size, for which the noise sources are the hardest to distinguish. These aircraft are an Airbus A380, Boeing B747, Boeing B737 and an Airbus A321. Their closest distance between the main landing gear and the engines are plotted in Figure 9.1 by the striped lines. For the previous camera the main landing gear and the engines can be distinguished from 1013 Hz for the A380, 1651 Hz for the B747 and 2332 Hz for the B737 and the A321. For the new camera this is 503 Hz for the A380, 820 Hz for the B747 and 1163 Hz for the B737 and the A321. The noise of the landing gear is expected to be visible at the lower frequencies, which was problematic for the previous camera for the smaller aircraft. The increase in resolution of the new camera should make it possible to have this distinction.

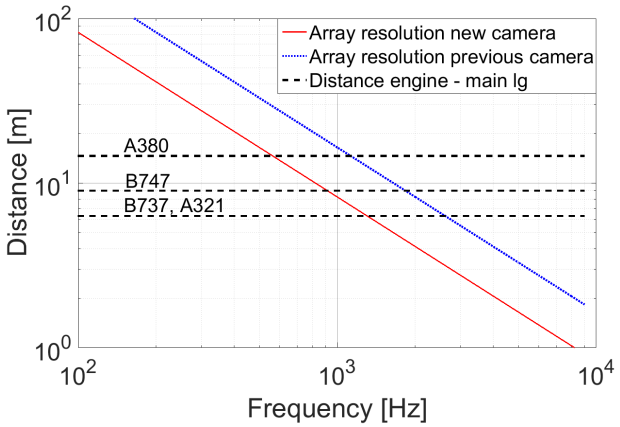

Figure 9.1: Array resolution of the new and previous fly-over camera at a height of 60 m

The old and the new plots are compared to check if the beamform plots are indeed improved with the increasing aperture. Conventional beamforming is used for the analysis and a 50 ms snapshot is taken when the aircraft is overhead, corresponding to a frequency resolution of 20 Hz. The source plots of the previous camera are obtained from Reference [42]. In Reference [42] a low (1050–4500 Hz) and a high (4500-9500 Hz) frequency band is used. The same frequency band and decibel range are used for the new beamform plots to be able to make a fair comparison. In the high frequency band only the engine noise is present. This is confirmed with Figure 9.2, which shows the beamform plot of a Boeing B737 with the previous and the new acoustic camera for the high frequency band. The low frequency band is more interesting to observe due to the present airframe noise. The beamform plots at the low frequency band are displayed in Figures 9.3 to 9.6.

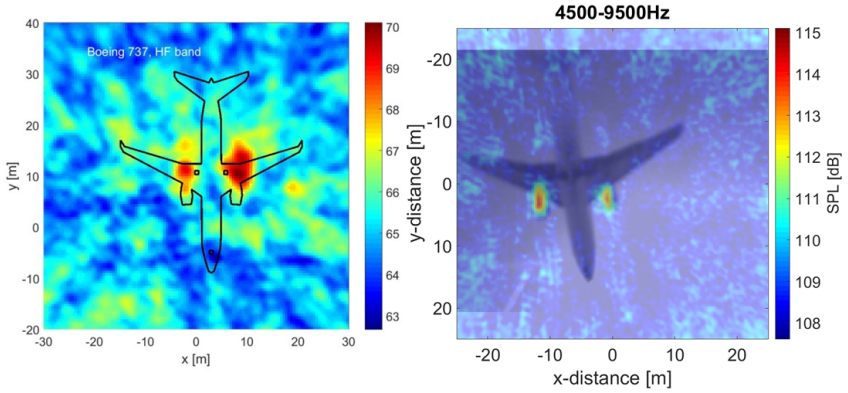

Figure 9.2: Beamform plot of the B737 using the high frequency band for the previous (left) and the new (right) acoustic camera

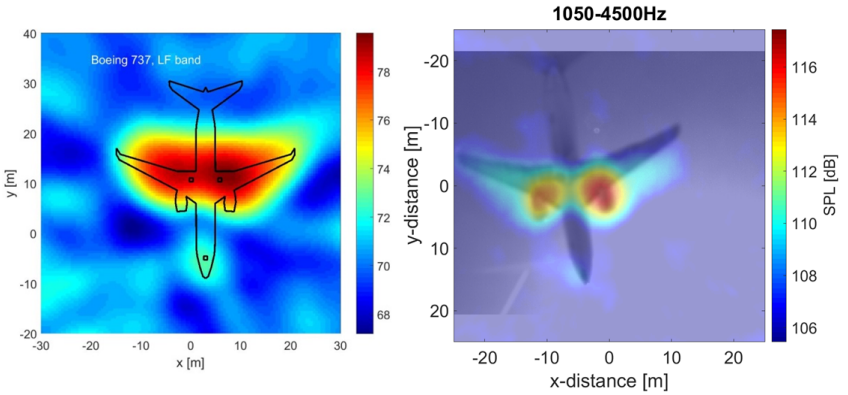

Figure 9.3: Beamform plot of the B737 using the low frequency band for the previous (left) and the new (right) acoustic camera

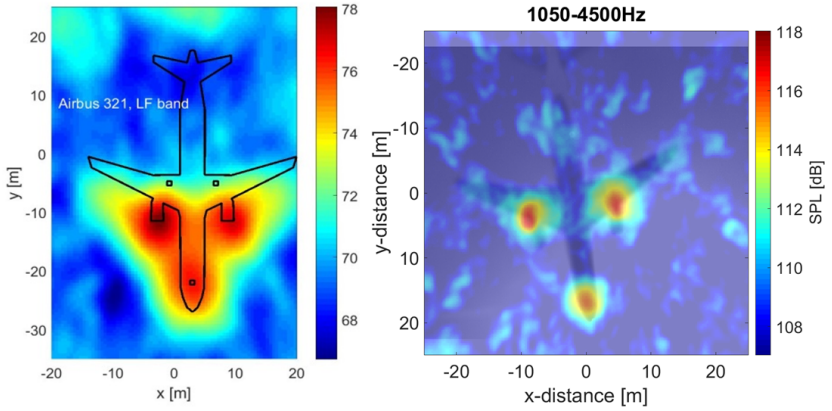

Figure 9.4: Beamform plot of the A321 using the low frequency band for the previous (left) and the new (right) acoustic camera

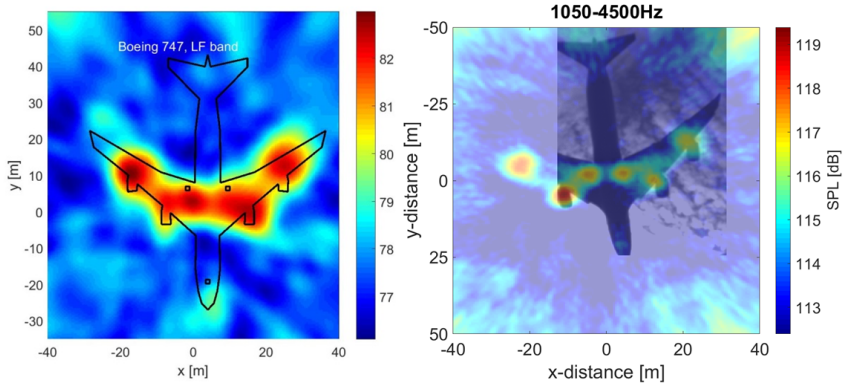

Figure 9.5: Beamform plot of the B747 using the low frequency band for the previous (left) and the new(right) acoustic camera

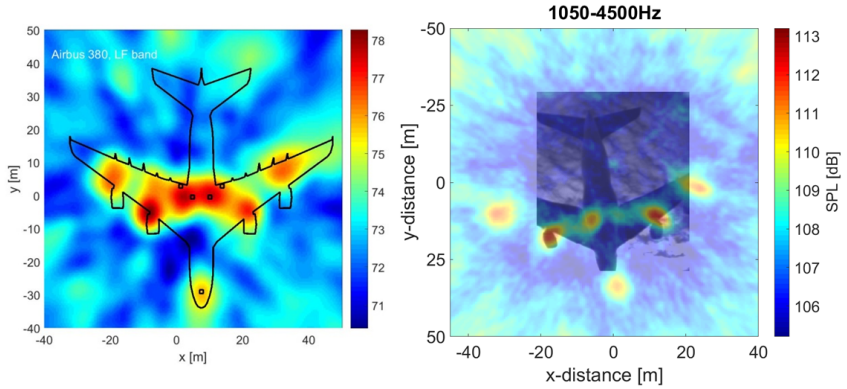

Figure 9.6: Beamform plot of the A380 using the low frequency band for the previous (left) and the new(right) acoustic camera

The beamform plots show a clear increase in resolution with the new camera. The B737 (Figure 9.3) shows for instance two separate sources placed on the engines instead of a large spot covering half the body of the aircraft. The sources are however quite large, which makes it hard to distinguish the engines from the main landing gear. The same applies to the A321 (Figure 9.4). The increase in resolution is more apparent for the Boeing B747 (Figure 9.4). The previous acoustic camera shows one spot covering both the engines and the main landing gear, while this is split in separate sources for the new camera. The Airbus A380 has a clear separation between the engines and the main landing gear. This was also the case for the previous acoustic camera.

The decibel range is set to 5 dB for clearer beamform pictures of the new acoustic camera. These new plots are displayed in Figure 9.7 and 9.8. The positioning of the sources is more precise in these pictures. For the B737 and the A321 it was not evident if the sources indicated the main landing gear or the engines. By adjusting the decibel scale, it is apparent that the sources are placed on the engines and that there is no source on the main landing gear. Different frequency bands and time frames are examined, but none show a clear noise source on the main landing gear. The resolution of the new camera is sufficient, but the main landing gear is not displayed for the smaller aircraft, which means they are not present as main noise sources.

From theory it is expected to see the engines as dominant noise source at the high frequencies. At the lower frequencies the airframe noise should also become visible. The main and nose landing gear are probably the main sources of this airframe noise. Based on model insights spots on the wings are expected apart from this, as noise from the slats, flaps and spoilers. (Chapter 2.6 and Reference [18, 30, 31, 42]) These expectations from the theory are visible in Figure 9.7 and 9.8. The high frequency band displays only the engines as main noise sources, while the low frequency band also highlights the main and nose landing gear. Noise from high lift devices and spoilers are no main noise sources in these measurements, but are sporadically visible when going through the frequency band in small steps.

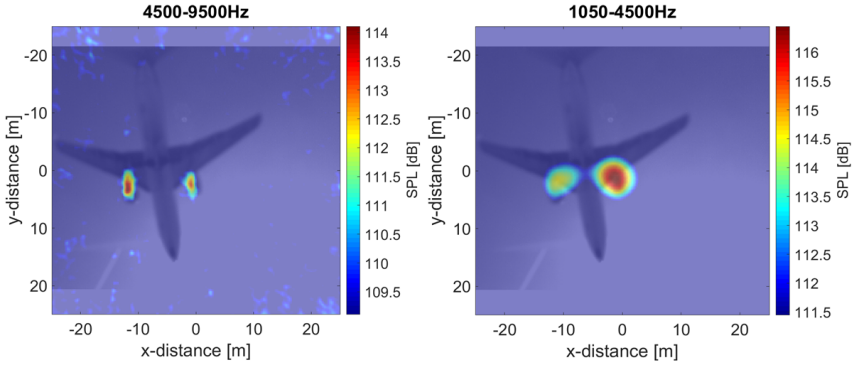

Figure 9.7: Beamform plot of the B737 using the high (left) and the low (right) frequency band

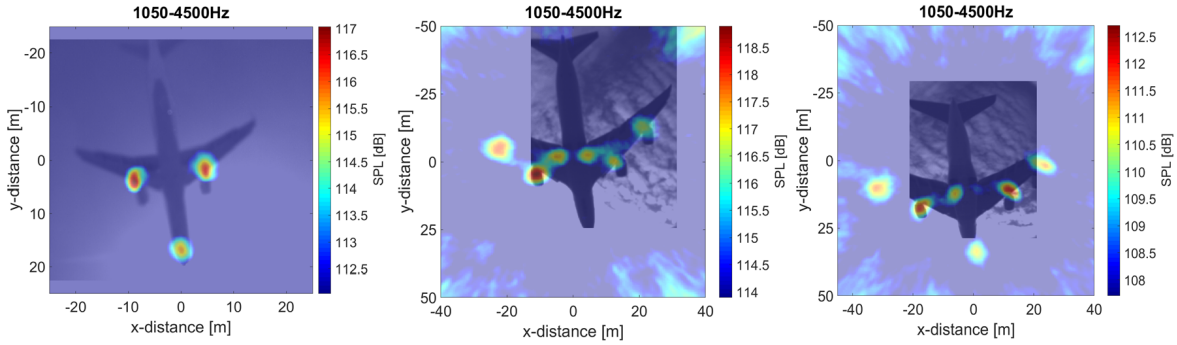

Figure 9.8: Beamform plot of the A321, B747 and A380 using the low frequency band

10

CONCLUSION AND RECOMMENDATIONS

The goal of the research is to quantify and improve the acoustic camera used by the TU Delft for the use of outdoor measurements. The quantification, optimisation and verification parts were carried out to reach this goal. Conclusions on these parts and on the main research question are given in Section 10.1. Section 10.2 presents points of improvement on the research and recommendations for future research.

10.1. CONCLUSION

The research is divided in three main parts: The quantification, optimisation and verification. Conclusions are drawn on each part separately to be able to answer the main research question.

10.1.1. QUANTIFICATION

The quantification starts with an examination of the directivity performance of the acoustic camera of the TU Delft. For the directivity quantification, a sound source was measured under an angle in a controlled environment (the anechoic chamber of the TU Delft). From this experiment, it was discovered that the source position had an offset which increased with increasing measurement angle. The weight factor used for beamforming can be adapted to avoid this position deviation. The sound pressure level also had a deviation with increasing measurement angle. However, no correlation between the deviation in measured sound pressure level and the source position could be found.

After the directivity experiment, the previous fly-over camera of the TU Delft was analysed. The main flaws of this camera were the position accuracy of the microphones, low resolution and unknown influence of the ground effect. A solution for the position accuracy and the resolution is designed during the optimisation phase, but for the ground effect additional information was required and a small study was performed. The transmission loss of the construction was considered first. It was concluded that only low frequencies would penetrate the structure and the influence on the measurements was minimal. For a Boeing B737 all noise with frequencies above 1250 Hz was filtered when measuring on a grass surface and above 2000 Hz for a concrete surface. A spectrogram analysis was performed on the data of a Boeing B737, measured with the previous fly-over camera to gather more information on the ground effect. Lloyd's mirror reflection was present in the spectrograms, but was not equal for all microphones. It became apparent that the position of the microphone in the array had a large influence on this effect. The microphones positioned near the edge of the array and in flight direction were affected most. This was due to edge diffraction and might be avoided by placing the microphones more than 30 cm from the edge. Noise of high frequencies was found for the power spectral density plots of the previous acoustic camera. High frequencies were not fully filtered out of the signal. No origins for this were found when looking at the general properties of the Sallen-Key filter. Also the data acquisition system of camera 4 (which is used during the fly-over measurements described in this report) did not give any sign of this presence of high frequency noise. This means that for the current system there is no high frequency noise.

10.1.2. OPTIMISATION

An optimised camera can de designed with all information gathered during the quantification phase. The optimisation starts with a decision on the general lay-out of the acoustic camera. Three common configurations

used for fly-over measurements are considered. These configurations are: separate microphones attached to one structure, separate microphones with their own holdings and all microphones attached to a plate. After a trade-off the configuration with all microphones attached to a plate is chosen due to the low costs, good manufacturability and high position accuracy.

For the array configuration an Underbrink spiral array is used due to its good overall performances, which are required when measuring fly-over aircraft. The array contains 64 microphones in an 8-arm configuration. The aperture of the array is doubled in comparison with the previous fly-over camera to 3.4 m. The increase in aperture results in an increase in resolution of the eventual beamform pictures. The microphones are placed 30 cm from the edges to avoid interference from edge diffracted sound waves.

The construction must be at least 4 x 4 m to be able to fit an array with these specifications. It is divided in 16 plates of 1 x 1 m to keep it easy to handle and transport. The plates can be assembled through support plates with bolts and winged nuts. Adjustable legs are placed below the support plates to make sure the camera can be set level. The main plates are made out of multiplex due to its strength, stiffness, weight, costs and manufacturability. Placed on top of the multiplex will be Flamex GU 12 mm foam to absorb reflections and decrease the signal interference. Clothes pins are used to clip the microphones and assure their exact positioning during all measurements. A structure holding the optical camera is made in the middle of the construction to obtain clear images required for the data analysis. Rough foam is placed over the microphones to serve as wind shield.

10.1.3. VERIFICATION

The optimised acoustic camera was built and an outdoor measurement campaign was carried out. This campaign was performed at the north side of the Zwanenburgbaan of Schiphol Airport. The aircraft information was gathered with an ADS-B receiver and checked with the optical camera. The measurements were carried out in three days. On the first day of the measurements, the portable batteries broke down and data from only 10 landing aircraft was obtained. The other two days went as planned and in total 161 landing aircraft could be measured.

The data had to be corrected for the background noise, the effects of forward motion, the Doppler effect and atmospheric effects before it could be analysed. When evaluating the ground effect, it became apparent that the fringes of Lloyd's mirror reflection were not detectable. This is the case for all microphones independent of their position within the array and with respect to the flight track of the aircraft. This means that by placing the microphones at least 30 cm from the edge, the interference of the edge diffraction is resolved.

Beamform plots made with the previous and the optimised acoustic camera were compared to check the influence of the increased aperture. The resolution had increased by doubling the array aperture. The engines and main landing gear could be distinguished for all aircraft, which could not be done with the smaller array.

10.1.4. MAIN RESEARCH QUESTION

The main research question can be answered by going through al main parts. The main research question is: What is the performance of the current acoustic camera used by the TU Delft and how can it be improved? The quantification section answers the first part of the research question: What is the performance of the current acoustic camera? No correlation between the sound pressure level and the measurement angle could be found. However, it was discovered that the position of the source deviates with increasing measurement angle, which could be solved by adjusting the weight factor used during beamforming. The issues of the previous fly-over camera were the position accuracy of the microphones, the resolution and the ground effect. These issues were all solved in the optimised design. The optimisation of the camera answers the second part of the main research question: How can the performance of the acoustic camera be improved? The position accuracy is increased by using a rigid structure, clamping the microphones and using adjustable legs. The resolution is increased by doubling the aperture of the array. The construction allows only low frequencies to penetrate the complete structure due to transmission loss, which will result in minimal interference of the ground reflected signal with the direct signal. The fringes of Lloyd's mirror pattern caused by edge diffraction are solved by placing the microphones at least 30 cm from the edge. To conclude, the main goal of the research is achieved. Knowledge is gained on the previous acoustic camera and an improved version is designed and tested.

10.2. RECOMMENDATIONS

Five major points of improvement were discovered during the research. These improvements have to do with the performance of the equipment, the documentation, the verification of the aircraft information, the data analysis and the design itself.

- The performance of the equipment needs to be improved during both the controlled and the outdoor measurements. No adequate correlation between the measurement angle and the sound pressure level was found during the directivity quantification. This might be different if the materials used were of a better quality. An omnidirectional speaker and microphones with a higher performance would already help. Better equipment could also be used during the Schiphol measurements. One measurement day was lost due to battery problems, which could be avoided.
- The research would have gone smoother if there was a good documentation available of previous researches. The wheel was reinvented, time was lost and the initial planning was exceeded. A complete manual with thorough documentation is made for this research to avoid re-inventing the wheel in the future.
- It would have been beneficial to have more data on the fly-over aircraft for the verification of the aircraft information. Ground data can be obtained from Schiphol or NLR apart from the ADS-B data and the information obtained with the optical camera.
- A different beamforming algorithm could be used for the data analysis to obtain more accurate source plots with lower side lobe levels.
- A point of improvement on the design of the optimised acoustic camera itself is the attachment of the clips. They got loose when under pressure during transport or set-up. This might be avoided by attaching them with split pens.

In the future, additional research can be carried out on the directivity performance of the optimised fly-over camera. Controlled angular measurements with a known source can be performed. The source can be attached to a drone which can fly over the acoustic camera at a specified height and position.

Furthermore, the fly-over data measured can be used in future research. The increase in resolution makes it possible to have a better verification of semi-empirical noise models, while the approximations for both the engines and the landing gear can be checked. With this, a better understanding of aircraft noise is created, which eventually enables people to decrease the aircraft's noise imprint on its environment.

BIBLIOGRAPHY

[1] L. Brusniak, J.R. Underbrink, R.W. Stoker, *Acoustic Imaging of Aircraft Noise Sources Using Large Aperture Phased Arrays*. The 27th American Institute of Aeronautics and Astronautics Aeroacoustics Conference, Massachusetts, May 2006

[2] D.G. Simons, *Introduction to aircraft noise*. Lecture sheets of the course Introduction to aircraft noise [AE4445] at the TU Delft, March 2015.

[3] B.D. van Veen, K.M. Buckley, 'Beamforming: A versatile approach to spatial filtering'. *IEEE ASSP Magazine*, April 1988

[4] D.G. Simons, *Advanced Aircraft Noise Modelling and Measurement*. Lecture sheets of the course Advanced Aircraft Noise Modelling and Measurement [AE4463] part 2 at the TU Delft, June 2016

[5] M. Carré, *Sound power estimation with an acoustic camera*. Lulea University of Technology, Lulea, November 2010

[6] P. Sjitsma, *Phased array beamforming applied to windtunnel and fly-over tests*. National Aerospace Laboratory NLR, December 2010

[7] E. Sarradj, *Optimal planar microphone array arrangements*. Brandenburgische Technische Universität Cottbus-Senftenberg, Germany, 2015

[8] J.J. Christensen, J. Hald, *Technical review: Beamforming*. Brüel and Kjaer, Denmark, 2004

[9] Z. Prime, C. Doolan, *A comparison of popular beamforming arrays*. Australian Acoustical Society, Victor Harbour, November 2013

[10] 01dB, *Noise Inspector - Acoustic Cameras Technical datasheet*. ACOEM group, France, October 2016

[11] E.J.G. Arcondoulis, C.J. Doolan, L.A. Brooks, A.C. Zander, *A Modification to Logarithmic Spiral Beamforming Arrays for Aeroacoustic Applications*. The 32nd American Institute of Aeronautics and Astronautics Aeroacoustics Conference, Oregon, June 2011

[12] J. Grythe, *Acoustic camera and beampattern*. Norsonic AS, Oslo, August 2015

[13] R.P. Dougherty, *Spiral-shaped array for broadband imaging*. US Patent 5,838,284. 17 November 1998

[14] A. Malgoezar, M. Snellen, P. Sijtsma, D. Simons, *Improving Beamforming by Optimization of Acoustic Array Microphone Positions*. The 5th Berlin Beamforming Conference, Berlin, 2016

[15] E.J. Arcondoulis, C.J. Doolan, A.C. Zander, L.A. Brooks, *Design and calibration of a small aeroacoustic beamformer*. The 20th International Congress on Acoustics, Sydney, August 2010

[16] L. Brusniak, J.R. Underbrink, R.W. Stoker, *Acoustic Imaging of Aircraft Noise Sources Using Large Aperture Phased Arrays*. The 27th American Institute of Aeronautics and Astronautics Aeroacoustics Conference, Massachusetts, May 2006

[17] BBC, *Waves*, 2014. Available from: http://www.bbc.co.uk/ [Accessed December 2016]

[18] L. Bertsch, *Noise sources on-board*. Lecture sheets of the course Advanced Aircraft Noise Modelling and Measurement [AE4463] part 1 at the TU Delft, May 2016

[19] G.J.J. Ruijgrok, *Elements of aviation acoustics*. Delft: Delft University press, 1993

[20] J.S. Lamancusa, *Outdoor Sound propagation*. Penn State, July 2009

[21] A. Mic, *Ground Reflection Interference in Aircraft Sound*. Available from: https://amateurgeophysics.wordpress.com/the-analysis-of-sound-using-raven-lite-software/6-the-analysis-of-sound-ground-reflection-interference-in-aircraft-sound/ [Accessed September 2017]

[22] J.H. Miles, *Analysis of ground reflection of jet noise obtained with various microphone arrays over an asphalt surface*. Eighty-ninth Meeting of the Acoustical Society of America, Texas, April 1975

[23] B.N. Shivashankara, G.W. Stubbs, *Ground Plane Microphone Installation for Measurement of Aircraft Fly-over Noise*. The Boeing Company, Seattle, 1984

[24] D.H.T. Bergmans, N.V. Bogholm, *Measuring environmental aircraft noise*. NLR, Augustus 2008

[25] W.L. Willshire, Jr., P.A. Nystrom, *Investigation of Effects of Microphone Position and Orientation on Near-Ground Noise Measurements*. NASA Technical Paper, 2004

[26] R.H. Randall, *An Introduction to Acoustics*. Mineola: Dover Publications, 2005

[27] Visaton, *K 50 SQ - 8 Ohm*. Available from: http://www.visaton.com/en/industrie/breitband/k50sq_8.html [Accessed September 2017]

[28] R. Schröder, O. Jaeckel, *Evaluation of beamforming systems*. 4^{th} Berlin Beamforming Conference, 2012

[29] J. Grythe, *Sparse arrays and array health check tool*. Norsonic, Oslo, April 2016

[30] M. Snellen, R. Merino-Martinez, D. Simons, 'Assessment of Noise Variability of Landing Aircraft Phased Microphone Array'. *Journal of Aircraft*, Aerospace Research Central, Articles in Advance, May 2017.

[31] M. Boon, M. Debrouwere, J. Domhof, R. van der Goot, J. Hendriks, A. Koelewijn, K. Scheper, E. Smeur, J. Verwilligen, L. Uyttersprot, *Final Report: AcoustiCam*. TU Delft Faculty of Aerospace Engineering, Delft, June 2011

[32] B.C. Baker, 'Stop-band limitations of the Sallen-Key low-pas filter'. *Analog Applications Journal*, Vol. 4Q, pp. 5-7, 2008

[33] S.W. Smith, *The Scientisi and Engineer's Guide to Digital Signal Processing*. 2nd edition, San Diego: California Technical Publishing, 1999

[34] W.M. Humphreys, Jr., D.P. Lockard, M.R. Khorrami, W.G. Culliton, R.G. McSwain, *Development and Calibration of a Field-Deployable Microphone Phased Array for Propulsion and Airframe Noise Flyover Measurements*. 22nd American Institute of Aeronautics and Astronautics Aeroacoustics Conference, Lyon, June 2016

[35] E. Sarradj, 'Three-Dimensional Acoustic SourceMapping with Different Beamforming Steering Vector Formulations'. *Advances in Acoustics and Vibration*, Hindawi Publishing Corporation, Vol. 2012, pp. 1-12, May 2012

[36] P. Jackson, *Jane's all the world's aircraft*. Jane's information group, United Kingdom, June 2016

[37] R.Beardmore, *Loaded flat plates*. Available from: http://www.roymech.co.uk/Useful_ Tables/ Mechanics/Plates.html [Accessed June 2017]

[38] Schiphol group, *Gebruiksprognose 2017 Amsterdam Airport Schiphol*. Technical report, Schiphol Group, October 2016

[39] Aircraft Noise and Climate Effects, *Acoustic camera user manual*, Aerospace Engineering, Delft University of Technology, September 2014

[40] KNMI, *Luchtvaartmetorologie*. Available from: http://www.knmi.nl/nederland-nu/luchtvaart [Accessed Augustus 2017]

[41] J.Y. Bouguet, *Camera calibration toolbox for Matlab*, October 2015. Available from: http://www.vision.caltech.edu/bouguetj/calib_ doc/

[42] D.G. Simons, M. Snellen, R. Merino-Martinez, A.M.N. Malgoezar, *Noise breakdown of landing aircraft using a microphone array and an airframe noise model*. Inter.noise conference, Hong Kong, August 2017

A

BUILDING PROCESS AND VERIFICATION

This appendix describes the building process and the verification of the optimised acoustic camera. It presents a short production plan with cost estimation in Section A.1. A verification experiment was carried out when all parts were manufactured to check if the design and production were executed correctly. This verification experiment is described in Section A.2.

A.1. PRODUCTION PLAN

All parts of the acoustic camera are described in Chapter 6. For the construction of these parts a production plan is made and carried out. The steps taken during the building process are:

- Cut large multiplex plates to 1 x 1 m
- Glue all clothes pins to the 90 deg. hooks
- Draw the positions of all holes on the large plates. This includes the holes for the microphones in the Underbrink spiral (D = 1.4 cm), the holes for the support plates (D = 0.9 cm) and a hole for the optical camera (D = 4 cm)
- Cut from the leftover multiplex the smaller support plates of 15 x 15 cm and the mid support plate of 20 x 20 cm
- Draw the holes for the bolt and winged nut on the support plates (D = 0.9 cm)
- Drill all holes in the big plates
- Drill all holes in the support plates
- Screw the cupboard legs to the support plates
- Screw the clothes pins to the big plates
- Cut the foam to match the big plates (16 times 1 x 1 m)
- Draw the Underbrink array on the foam and make small holes at those positions
- Glue the foam to the big plates
- Make 64 circles with a diameter of 40 mm out of rough foam
- Elongate the wires of the microphones
- Elongate the wire for the optical camera
- Make the holding for the optical camera and attach it to the mid support plate
- Mark the position of the microphones on the camera and label the microphones

The tasks were carried out at the flight hall of aerospace engineering. The eventual parts manufactured are displayed in Figure A.1 and the complete design in Figure A.2. The total costs of the camera were €785.91. An elaborate cost estimation is displayed in Appendix B.

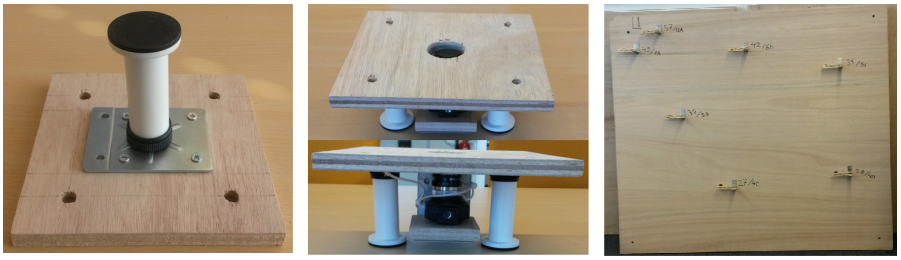

Figure A.1: A support plate, the mid plate with optic camera and a big plate from the back

Figure A.2: Set-up for the verification of the complete acoustic camera

A.2. DESIGN VERIFICATION

Before executing verification measurements at Schiphol Airport, the acoustic camera was tested indoors at the TU Delft. For this experiment it was checked if the microphones were working, if all plates fitted together, if the optical camera works, what the set-up time is and if the acoustic camera could handle measurements with a small sound source.

A.2.1. MICROPHONES

As mentioned in Section A.1, the wires of the microphones were elongated. Due to the elongation, the signal gets degraded. The maximum diminution of the signal is 0.58 dB and the mean 0.23 dB. All microphones are calibrated with a pistonphone calibration at 1000 Hz and 94 dB. The average calibration factor was 1.02.

A.2.2. SET-UP

The experiment was executed in Lecture room E in the building of Aerospace Engineering at the TU Delft. First the set-up time of the camera was measured. This was approximately 45 minutes with 2 people. The set-up consisted of attaching the support plates to the big plates with a bolt and winged nut, clipping the microphones to their assigned position, placing the optical camera in its holder in the middle of the camera and attaching all wires to the data acquisition system and a laptop. The sound source used for the experiment is the Visaton K50SQ. The speaker was attached to a wire and placed 1.5 m above the microphones near the middle of the acoustic camera. The whole set-up fitted together and is displayed in Figure A.2.

While testing the acoustic camera it became apparent that the optical camera gave a good image, but was placed a bit too low. A part of the absorption foam blocked the view of the camera. This was solved by lifting the camera with a small wooden block.

A.2.3. SOUND SOURCE

After assembling the camera, its ability to detect sound sources was tested. It has to be noted that the camera is designed for fly-over measurements. The array aperture is 3.4 m to increase the resolution of fly-over aircraft. The aircraft are quite big and will fly over the camera at a height of about 60 m. During this experiment the sound source is approximately 5 x 5 cm and placed at 1.5 m above the array. The measurements were carried out within the desired frequency band for the fly-over measurements. This frequency band is

determined in Chapter 5.4 and is from 500 to 15000 Hz. To have an acceptable measurement time only the centre frequencies of the octave bands were played, which means the measured frequencies were: 500, 1000, 2000, 4000, 8000 and 15000 Hz.

For the data analysis, first the response per microphone is examined. An example of the sound pressure level (SPL) for each microphone is displayed in Figure A.3. This figure shows that microphone 21 has a lower value than the rest of the microphones. The microphone was broken and is left out the data analysis. For all frequencies the power spectral density (PSD) was plotted to see if the frequency emitted was also the frequency measured. Figure A.4 displays the PSD plot at 500 Hz at which a peak is visible at its matching frequency, which was the case for all frequencies.

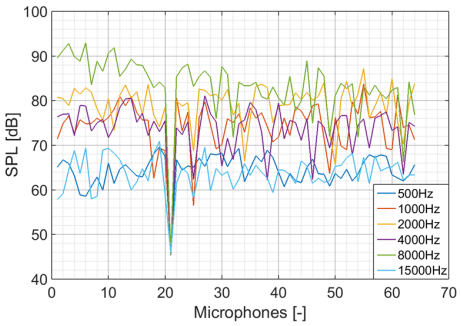

Figure A.3: SPL per microphone

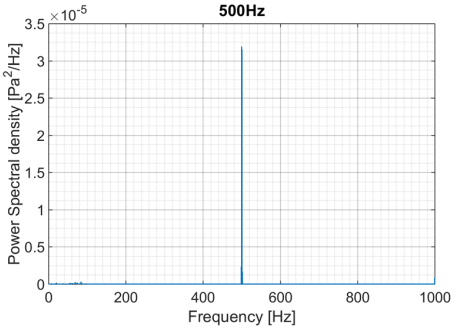

Figure A.4: PSD plot at 500 Hz

Conventional beamforming is used for the estimation of the strength and position of the source. The real position of the speaker was at the coordinates (0,0.25). Table A.1 shows the position of the speaker estimated through beamforming, with in Figure A.5 the position deviation. From this data it is apparent that at low frequencies, the position estimation is well within boundaries. The maximum deviation is 9 cm and the average deviation 1.8 cm.

Table A.1: Source position obtained through beamforming

Frequency [Hz]	**500**	**1000**	**2000**	**4000**	**8000**	**15000**
x-position [m]	0.01	-0.01	0	-0.03	0.01	0.04
y-position [m]	0.25	0.24	0.25	0.34	0.26	0.26

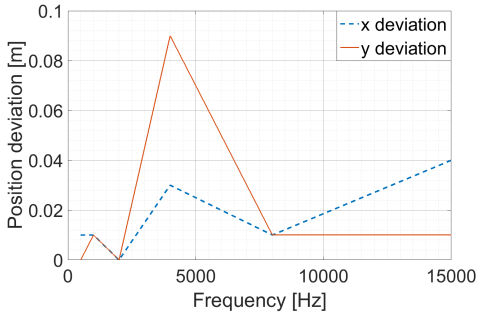

Figure A.5: Deviation between the original position and the position obtained through beamforming

The obtained source plots are displayed in Figure A.6. The lower frequencies display a clear clean source, but at higher frequencies more side lobes appear and it becomes hard to distinguish the main source. This increase in side lobes is due to the large size of the speaker compared to the small distance to the source. This is displayed with a simulated beamform plot in Figure A.7. Within this figure a source is simulated at 1 m distance from the camera. The figure on the left is simulated with the array as is in real life and the figure on the right is with an aperture of half this size. The increase in side lobes with the aperture is clearly visible. However, this large aperture is required to obtain a good resolution when using the camera to measure fly-over aircraft. This effect is displayed in Figure A.8. The same arrays as for Figure A.7 are used, but the source is placed at 50 m distance. Both give a clear picture of the main noise source without side lobes. However,

the main lobe width of the array with the large aperture is smaller, which makes it better to pinpoint the exact main noise source with its location.

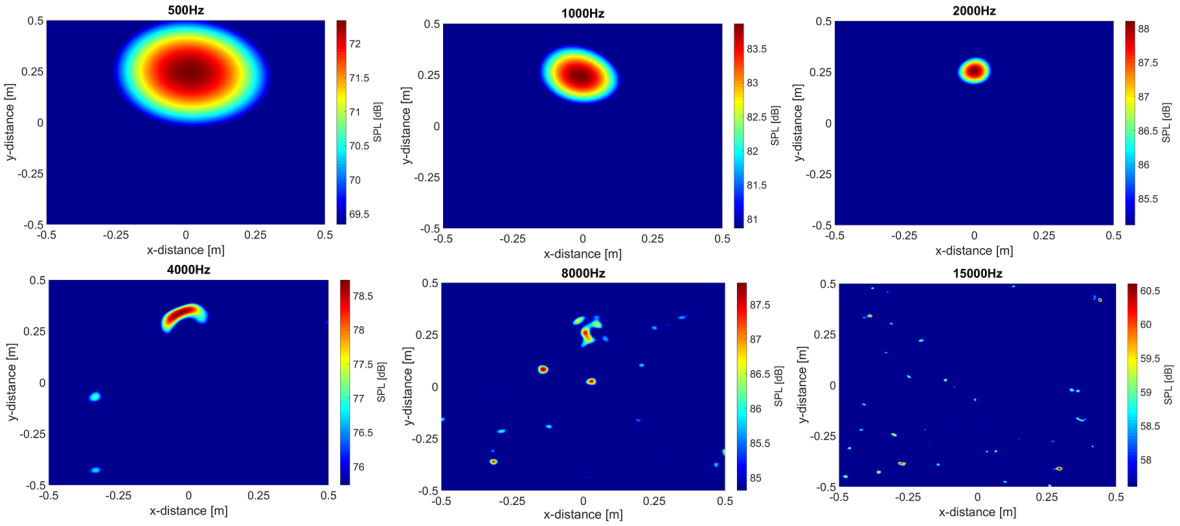

Figure A.6: Source plots obtained through conventional beamforming at 500, 1000, 2000, 4000, 8000 and 15000 Hz

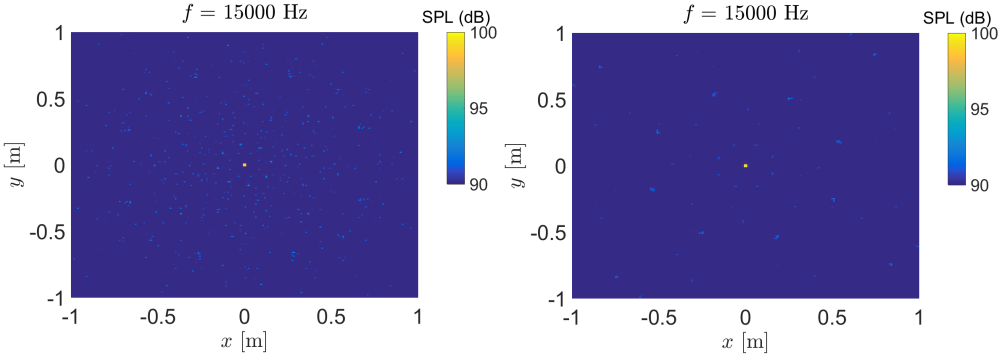

Figure A.7: Simulated source plots with an Underbrink spiral array with an aperture of 3.4 m (left) and 1.7 m (right) with the source at 1 m distance

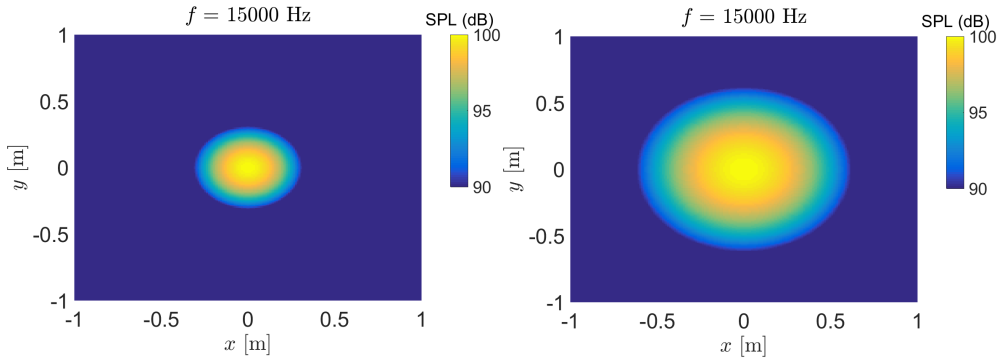

Figure A.8: Simulated source plots with an Underbrink spiral array with an aperture of 3.4 m (left) and 1.7 m (right) with the source at 50 m distance

B

COST BREAKDOWN

Table B.1: Cost breakdown of the acoustic camera

Part	Amount	Shop	Costs
Multiplex plates (244 x 122 x 1.2 cm)	8	Gamma	283.92
Bolts (M8, L40)	100	Hornbach	8.75
Winged nuts (M8)	100	Hornbach	27.10
Rough foam (158 x 82 x 23 mm)	4	Hornbach	21.80
Flamex GU foam (100 x 120 x 1.5 cm)	16	Akoestiekwinkel	290.82
Stauf extreme tack glue	1	Akoestiekwinkel	12.33
Usb cable optic camera (5m)	1	Conrad	14.94
Clothes pins	64	Hema	2.50
90deg. angled plates (40mm)	64	Gamma	16.94
1 second glue	2	Gamma	3.39
Tie wraps (pack)	1	Gamma	1.50
Cupboard legs	26	Ikea	49.00
Screws (3 x 12 mm)	128	Gamma	8.45
Screws (3.5 x 16 mm)	104	Gamma	5.97
Aluminium tape	1	Gamma	8.99
Flux	1	Gamma	7.29
Heat shrink	6	Praxis	17.94
Bolt with nut (M5, L16)	2	Gamma	2.29
Lighter	1	Gamma	1.99
Total			**785.91**

C

MEASURED AIRCRAFT

This appendix displays information on the measured aircraft. It is divided in three tables for the three measurement days. Table C.1 displays the aircraft measured on the 14^{th} of August, Table C.2 on the 16^{th} of October and Table C.3 on the 17^{th} of October. The information includes the measurement number, the file name, the ICAO (registration code from the International Civil Aviation Organization), the type of aircraft, the engine type and its registration number. Table C.1 has blank spots while these aircraft were not detected by a malfunction in the ADS-B receiver.

Table C.1: Information on the measured aircraft on the 14^{th} of August

Landing aircraft						
Nr.	**File name**	**ICAO**	**Callsign**	**Type**	**Engine**	**Registration**
1	2017-08-14_ 13-13-48	4BAA88	THY2UE	A321-231	2x V2500	TC-JTH
2	2017-08-14_ 13-15-16	48415F	KLM18G	B737-8K2	2x CFM56-7	PH-BXF
3	2017-08-14_ 13-16-48	06A13A	QTR31GD	B777-3DZ	2x GE90	A7-BAX
4	2017-08-14_ 13-19-05	484160	KLM1974	B737-8K2	2x CFM56-7	PH-BXG
5	2017-08-14_ 13-20-33	x	x	x	x	x
6	2017-08-14_ 13-22-04	484F01	TFL112	B737-86N	2x CFM56-7	PH-TFD
7	2017-08-14_ 13-23-36	48548E	KLM76L	Emb-175-200STD	2x CF34	PH-EXL
8	2017-08-14_ 13-25-04	484CB9	KLM36X	B737-7K2	2x CFM56-7	PH-BGT
9	2017-08-14_ 13-27-31	x	x	x	x	x
10	2017-08-14_ 13-28-58	484556	KLM88B	B737-8K2	2x CFM56-7	PH-BXY
Take-off aircraft						
Nr.	**File name**	**ICAO**	**Callsign**	**Type**	**Engine**	**Registration**
11	2017-08-14_ 15-00-00	484B92	x	B737-7K2	2x CFM56-7	PH-BGL
12	2017-08-14_ 15-01-21	3.99100	x	A320-214	CFM56-5B4/3	F-HEPC
13	2017-08-14_ 15-02-30	4B84E7	x	A321-231	2x V2500	TC-AGG
14	2017-08-14_ 15-03-51	485206	x	E-190-100STD	2x CF34	PH-EXE
15	2017-08-14_ 15-04-48	4B160B	x	A320-214	2x CFM56-5	HB-IJB
16	2017-08-14_ 15-06-13	395024	x	Erj-145-MP	2x AN AE3007	F-GUBE
17	2017-08-14_ 15-07-21	3C6619	x	A320-211	2x CFM56-5	D-AIPY
18	2017-08-14_ 15-38-16	AB5D52	DAL165	A330-302	2x CF6-80	N831NW
19	2017-08-14_ 15-39-43	484B2A	TRA181B	B737-8K2	2x CFM56-7	PH-HSA

Table C.2: Information on the measured aircraft on the 16^{th} of October

Nr.	File name	ICAO	Type	Engine	Registration
1	2017-10-16_ 11-16-07	4855D1	ERJ-175STD	2xCF34	PH-EXO
2	2017-10-16_ 11-17-47	484ACB	ERJ-190STD	2xCF34	PH-EZA
3	2017-10-16_ 11-19-18	3444C8	A320-214	2x CFMI CFM56-5B4/P	EC-MBK
4	2017-10-16_ 11-21-18	48507F	ERJ-190STD	2xCF34	PH-EXA
5	2017-10-16_ 11-22-51	48507F	A320-214	2x CFM56-5	9H-AEI
6	2017-10-16_ 11-24-27	484556	B737-8K2	2x CFM56-7	PH-BXY
7	2017-10-16_ 11-26-13	484163	B737-8K2	2x CFM56-7	PH-BXK
8	2017-10-16_ 11-28-09	5110CA	CRJ-900LR	2x CF34	ES-ACG
9	2017-10-16_ 11-29-59	4840D4	Fokker 70	2x RR RB.183 Tay	PH-KZB
10	2017-10-16_ 11-31-29	4855D2	ERJ-175STD	2x CF34	PH-EXP
11	2017-10-16_ 11-32-37	4BA8E3	B737-8F2	2x CFM56-7	TC-JGC
12	2017-10-16_ 11-34-17	4852F4	ERJ-175STD	2x CF34	PH-EXG
13	2017-10-16_ 11-36-00	393D82	A319-113	2x CFM56-5	F-GPMC
14	2017-10-16_ 11-37-16	393D82	B737-8K2	2x CFM56-7	PH-BGC
15	2017-10-16_ 11-40-13	5081E7	B737-8HX	2x CFM56-7	UR-PSA
16	2017-10-16_ 12-47-17	48418C	B737-9K2	2x CFM56-7	PH-BXR
17	2017-10-16_ 12-50-23	C033A0	B737-8HX	2x CFM56-7	C-FTOH
18	2017-10-16_ 12-53-17	3430CD	A320-216	2x CFM56-5	EC-KMI
19	2017-10-16_ 13-03-04	484F16	B737-7K2	2x CFM56-7	PH-BGW
20	2017-10-16_ 13-06-51	495293	A319-112	2x CFM56-5	CS-TTS
21	2017-10-16_ 13-08-36	484C54	ERJ-190STD	2x CF34	PH-EZP
22	2017-10-16_ 13-09-56	484CB9	B737-7K2	2x CFM56-7	PH-BGT
23	2017-10-16_ 13-11-55	484966	B737-7K2	2x CFM56-7	PH-BGG
24	2017-10-16_ 13-13-39	484160	B737-8K2	2x CFMI CFM56-7B24	PH-BXG
25	2017-10-16_ 13-15-15	4844C6	B737-8K2	2x CFMI CFM56-7B24	PH-BXV
26	2017-10-16_ 13-17-04	484166	B737-8K2	2x CFMI CFM56-7B24	PH-BXN
27	2017-10-16_ 13-18-28	4D0113	B747-8RF	4x GEnx-2B67	LX-VCJ
28	2017-10-16_ 13-20-42	8963F0	A380-8EI	4x GP7270	A6-EOS
29	2017-10-16_ 13-23-12	06A072	B777-3DZ	2x GE GE90-115B	A7-BAH
30	2017-10-16_ 13-25-45	4852F5	ERJ-175STD	2x GE CF34-8E5	PH-EXH
31	2017-10-16_ 13-27-24	48548C	ERJ-175STD	2x GE CF34-8E5	PH-EXK
32	2017-10-16_ 13-28-51	484CB4	B737-8K2	2x CFMI CFM56-7B24	PH-BCA
33	2017-10-16_ 13-30-39	484F7E	ERJ-190STD	2x GE CF34-10E5	PH-EZV
34	2017-10-16_ 13-32-27	39B16D	CRJ-1000	2x GE CF34-8C5A2	F-HMLN
35	2017-10-16_ 13-34-12	484FDE	B737-8K2	2x CFMI CFM56-7B24E	PH-BCD
36	2017-10-16_ 13-35-42	485342	B787-9	2x GEnx-1B	PH-BHH
37	2017-10-16_ 13-37-51	4CA6AC	Avro RJ85	4x LY LF507-1F	EI-RJY
38	2017-10-16_ 13-39-31	4BAA50	A321-231	2x IAE V2533-A5	TC-JRP
39	2017-10-16_ 13-41-16	484C52	ERJ-190STD	2x GE CF34-10E5	PH-EZN
40	2017-10-16_ 13-42-44	4841A8	B737-8K2	2x CFMI CFM56-7B27	PH-HZX
41	2017-10-16_ 15-04-57	4855D2	ERJ-175STD	2x GE CF34-8E5	PH-EXP
42	2017-10-16_ 15-07-02	4855D1	ERJ-175STD	2x GE CF34-8E5	PH-EXO
43	2017-10-16_ 15-10-19	345313	A320-232	2x IAE V2527-A5	EC-MOG
44	2017-10-16_ 15-12-45	4851AE	B787-9	2x GEnx-1B	PH-BHC
45	2017-10-16_ 15-15-05	04C118	B787-8	2x GEnx-1B	5Y-KZB
46	2017-10-16_ 15-17-50	48418A	B737-9K2	2x CFMI CFM56-7B26	PH-BXO
47	2017-10-16_ 15-19-41	48415E	B737-8K2	2x CFMI CFM56-7B24	PH-BXE
48	2017-10-16_ 15-21-49	485086	ERJ-190STD	2x GE CF34-10E5	PH-EXD
49	2017-10-16_ 15-23-40	485207	ERJ-190STD	2x GE CF34-10E5	PH-EXF
50	2017-10-16_ 15-25-26	484F15	B737-7K2	2x CFMI CFM56-7B22E	PH-BGU
51	2017-10-16_ 15-27-07	48548E	ERJ-175STD	2x GE CF34-8E5	PH-EXL
52	2017-10-16_ 15-28-41	780D8F	B777-FFT	2x GE GE90-110B1	B-2094
53	2017-10-16_ 15-31-42	484B30	ERJ-190STD	2x GE CF34-10E5	PH-EZC
54	2017-10-16_ 15-33-07	484CB7	B737-7K2	2x CFMI CFM56-7B22	PH-BGQ
55	2017-10-16_ 15-34-33	48436C	B777-206(ER)	2x GE GE90-94B	PH-BQE

Nr.	File name	ICAO	Type	Engine	Registration
56	2017-10-16_ 15-37-24	485064	ERJ-190STD	2x GE CF34-10E5	PH-EZY
57	2017-10-16_ 15-38-57	484B02	Fokker 70	2x RR Tay 620-15	PH-KZU
58	2017-10-16_ 15-40-17	484163	B737-8K2	2x CFMI CFM56-7B24	PH-BXK
59	2017-10-16_ 15-41-58	400FE2	A319-111	2x CFMI CFM56-5B5/P	G-EZBR
60	2017-10-16_ 15-43-29	7807BB	B777-F1B	2x GE GE90-110B1	B-2080
61	2017-10-16_ 15-46-10	484B00	Fokker 70	2x RR Tay 620-15	PH-KZS
62	2017-10-16_ 15-47-47	484F80	ERJ-190STD	2x GE CF34-10E5	PH-EZX
63	2017-10-16_ 15-49-28	485206	ERJ-190STD	2x GE CF34-10E5	PH-EXE
64	2017-10-16_ 15-50-45	4851AF	B787-9	2x GEnx-1B	PH-BHD
65	2017-10-16_ 15-53-04	484442	B737-8BK	2x CFMI CFM56-7B24	PH-BXU
66	2017-10-16_ 15-55-00	48455C	B737-7K2	2x CFMI CFM56-7B22	PH-BGE
67	2017-10-16_ 15-56-25	484B92	B737-7K2	2x CFMI CFM56-7B22	PH-BGL
68	2017-10-16_ 15-58-23	4852F4	ERJ-175STD	2x GE CF34-8E5	PH-EXG
69	2017-10-16_ 15-59-58	484F18	B737-8K2	2x CFMI CFM56-7B24	PH-BCB
70	2017-10-16_ 16-01-31	4845EB	B737-8K5	2x CFMI CFM56-7B26	PH-TFA

Table C.3: Information on the measured aircraft on the 17^{th} *of October*

Nr.	File name	ICAO	Type	Engine	Registration
1	2017-10-17_ 10-42-09	501D1F	A320-214	2x CFMI CFM56-5B4/P	9A-CTJ
2	2017-10-17_ 10-44-08	48506D	B787-8	2x GEnx-1B	PH-TFM
3	2017-10-17_ 10-46-21	48418B	B737-9K2	2x CFMI CFM56-7B26	PH-BXP
4	2017-10-17_ 10-48-02	4853D3	B737-8K2	2x CFMI CFM56-7B26E	PH-HXJ
5	2017-10-17_ 10-50-19	4852F5	ERJ-175STD	2x GE CF34-8E5	PH-EXH
6	2017-10-17_ 10-54-49	484C54	ERJ-190STD	2x GE CF34-10E5	PH-EZP
7	2017-10-17_ 10-58-10	4A08EB	B737-82R	2x CFMI CFM56-7B26E	YR-BGK
8	2017-10-17_ 11-00-03	484B31	ERJ-190STD	2x GE CF34-10E5	PH-EZD
9	2017-10-17_ 11-02-15	4841A9	B737-8K2	2x CFMI CFM56-7B27	PH-HZW
10	2017-10-17_ 11-06-51	4855D0	ERJ-175STD	2x GE CF34-8E5	PH-EXN
11	2017-10-17_ 11-08-47	48415F	B737-8K2	2x CFMI CFM56-7B24	PH-BXF
12	2017-10-17_ 11-10-20	484AA1	B737-8K2	2x CFMI CFM56-7B27	PH-HSW
13	2017-10-17_ 11-12-07	484C53	ERJ-190STD	2x GE CF34-10E5	PH-EZO
14	2017-10-17_ 11-13-50	4BB841	A320-251N	2x CFMI LEAP-1A26	TC-NBA
15	2017-10-17_ 11-15-27	4D2025	A320-214	2x CFMI CFM56-5B4/P	9H-AEO
16	2017-10-17_ 11-17-16	484163	B737-8K2	2x CFMI CFM56-7B24	PH-BXK
17	2017-10-17_ 11-19-22	485084	ERJ-190STD	2x GE CF34-10E5	PH-EXB
18	2017-10-17_ 11-20-55	485065	ERJ-190STD	2x GE CF34-10E5	PH-EZZ
19	2017-10-17_ 11-23-02	4BAA06	A320-232	2x IAE V2527-A5	TC-JPF
20	2017-10-17_ 11-26-05	484556	B737-8K2	2x CFM56-7	PH-BXY
21	2017-10-17_ 11-28-15	484C26	ERJ-190STD	2x GE CF34-10E5	PH-EZK
22	2017-10-17_ 11-29-38	3985A2	A320-214	2x CFMI CFM56-5B4/3	F-HBNC
23	2017-10-17_ 11-31-10	484160	B737-8K2	2x CFMI CFM56-7B24	PH-BXG
24	2017-10-17_ 11-33-04	484B00	Fokker 70	2x RR Tay 620-15	PH-KZS
25	2017-10-17_ 11-36-38	89649C	A330-243F	2x RR Trent 772B-60	A6-DCE
26	2017-10-17_ 12-54-22	484371	B777-206(ER)	2x GE GE90-94B	PH-BQK
27	2017-10-17_ 12-56-55	4840E6	Fokker 70	2x RR Tay 620-15	PH-KZI
28	2017-10-17_ 12-58-46	344285	A320-232	2x IAE V2527-A5	EC-LQN
29	2017-10-17_ 13-00-48	484130	B737-8K2	2x CFMI CFM56-7B24	PH-BXA
30	2017-10-17_ 13-04-20	485009	B737-8K2	2x CFMI CFM56-7B27E	PH-HSI
31	2017-10-17_ 13-06-40	4BAA8B	A321-231	2x IAE V2533-A5	TC-JTK
32	2017-10-17_ 13-08-23	484559	B737-8K2	2x CFMI CFM56-7B24	PH-BGB
33	2017-10-17_ 13-10-04	484F06	B737-7K2	2x CFMI CFM56-7B22	PH-BGM
34	2017-10-17_ 13-12-23	896183	A380-861	4x GP7270	A6-EED
35	2017-10-17_ 13-15-50	48455B	B737-7K2	2x CFMI CFM56-7B22	PH-BGD

Nr.	File name	ICAO	Type	Engine	Registration
36	2017-10-17_ 13-16-56	485339	B737-86J	2x CFMI CFM56-7B26E	PH-CDH
37	2017-10-17_ 13-19-02	4855D2	ERJ-175STD	2x GE CF34-8E5	PH-EXP
38	2017-10-17_ 13-20-34	484CC2	ERJ-190STD	2x GE CF34-10E5	PH-EZR
39	2017-10-17_ 13-21-57	484166	B737-8K2	2x CFMI CFM56-7B24	PH-BXN
40	2017-10-17_ 13-23-18	4BA74B	B737-86J	2x CFMI CFM56-7B24	TC-IZK
41	2017-10-17_ 13-25-03	484F07	B737-7K2	2x CFMI CFM56-7B22	PH-BGP
42	2017-10-17_ 13-26-38	484C1B	ERJ-190STD	2x GE CF34-10E5	PH-EZG
43	2017-10-17_ 13-28-08	484EE4	B737-8K2	2x CFMI CFM56-7B27	PH-HSD
44	2017-10-17_ 13-32-32	485122	B737-8K2	2x CFMI CFM56-7B27E	PH-HSK
45	2017-10-17_ 13-34-38	48520C	B737-8K2	2x CFMI CFM56-7B24E	PH-HXD
46	2017-10-17_ 13-35-51	4B8686	A321-211	2x CFMI CFM56-5B3/P	TC-ATF
47	2017-10-17_ 13-37-54	395025	ERJ-145MP	2x AN AE3007A1	F-GUBF
48	2017-10-17_ 13-39-16	406B8E	A320-214	2x CFMI CFM56-5B4/3	G-EZWV
49	2017-10-17_ 13-41-50	06A07C	B777-3DZ	2x GE GE90-115B	A7-BAP
50	2017-10-17_ 13-44-07	4B8E0B	B737-82R	2x CFMI CFM56-7B26E	TC-CPK
51	2017-10-17_ 13-46-13	4CA4E3	Avro RJ85	4x LY LF507-1F	EI-RJO
52	2017-10-17_ 13-47-55	48418C	B737-9K2	2x CFMI CFM56-7B26	PH-BXR
53	2017-10-17_ 13-49-39	343194	A320-214	2x CFMI CFM56-5B4/3	EC-KRH
54	2017-10-17_ 13-51-16	484162	B737-8K2	2x CFMI CFM56-7B24	PH-BXI
55	2017-10-17_ 13-52-57	4841A6	B737-9K2	2x CFMI CFM56-7B26	PH-BXT
56	2017-10-17_ 13-54-38	4CA51F	Avro RJ85	4x LY LF507-1F	EI-RJT
57	2017-10-17_ 13-56-20	484F15	B737-7K2	2x CFMI CFM56-7B22E	PH-BGU
58	2017-10-17_ 13-58-21	400CD2	A319-111	2x CFMI CFM56-5B5/P	G-EZIS
59	2017-10-17_ 15-00-54	4851F6	B777-306(ER)	2x GE GE90-115B	PH-BVS
60	2017-10-17_ 15-03-42	3C4D63	CRJ-900LR	2x GE CF34-8C5	D-ACKC
61	2017-10-17_ 15-05-17	485341	B787-9	2x GEnx-1B	PH-BHG
62	2017-10-17_ 15-07-49	484135	B737-8K2	2x CFMI CFM56-7B27	PH-HZE
63	2017-10-17_ 15-09-26	04C118	B787-8	2x GEnx-1B	5Y-KZB
64	2017-10-17_ 15-13-58	485206	ERJ-190STD	2x GE CF34-10E5	PH-EXE
65	2017-10-17_ 15-16-00	48414D	B737-8K2	2x CFMI CFM56-7B27	PH-HZI
66	2017-10-17_ 15-18-52	4B8DF2	B737-8SH	2x CFMI CFM56-7B26E	TC-COR
67	2017-10-17_ 15-20-59	4852F6	ERJ-175STD	2x GE CF34-8E5	PH-EXI
68	2017-10-17_ 15-23-39	484B02	Fokker 70	2x RR Tay 620-15	PH-KZU
69	2017-10-17_ 15-25-26	484B90	B737-7K2	2x CFMI CFM56-7B22	PH-BGI
70	2017-10-17_ 15-27-34	4851AE	B787-9	2x GEnx-1B	PH-BHC
71	2017-10-17_ 15-29-56	484C54	ERJ-190STD	2x GE CF34-10E5	PH-EZP
72	2017-10-17_ 15-31-45	4852F4	ERJ-175STD	2x GE CF34-8E5	PH-EXG
73	2017-10-17_ 15-33-17	4841D7	B737-7K2	2x CFMI CFM56-7B24	PH-XRZ
74	2017-10-17_ 15-34-57	780C5B	B777-FFT	2x GE GE90-110B1	B-2091
75	2017-10-17_ 15-37-17	48455A	B737-8K2	2x CFMI CFM56-7B24	PH-BGC
76	2017-10-17_ 15-39-01	484F7C	ERJ-190STD	2x GE CF34-10E5	PH-EZT
77	2017-10-17_ 15-40-23	4691C5	A320-323	2x IAE V2527-A5	SX-DNE
78	2017-10-17_ 15-42-08	4840D4	Fokker 70	2x RR Tay 620-15	PH-KZB
79	2017-10-17_ 15-43-38	484966	B737-7K2	2x CFMI CFM56-7B22	PH-BGG
80	2017-10-17_ 15-45-05	4855D1	ERJ-175STD	2x GE CF34-8E5	PH-EXO
81	2017-10-17_ 15-46-38	4B8E05	B737-82R	2x CFMI CFM56-7B26E	TC-CPE
82	2017-10-17_ 15-48-18	484B31	ERJ-190STD	2x GE CF34-10E5	PH-EZD
83	2017-10-17_ 15-49-44	484165	B737-8K2	2x CFMI CFM56-7B24	PH-BXM

D

SOUND ATTENUATION COEFFICIENT

The sound attenuation coefficient is dependent on the frequency of the sound, the air temperature, the atmospheric pressure and the amount of water vapour in the atmosphere. This appendix shows how to calculate the sound attenuation coefficient. Within these calculations all variables with a lowercase zero stand for the reference values, which are taken at sea level. The equations are taken from Reference [20].

The attenuation coefficient can be calculated with the use of Equation D.1. Within this equation T is the atmospheric temperature, p_s is the atmospheric pressure and F is the scaled frequency. F and can be rewritten as $F = \frac{f}{p_s}$. $F_{r,O}$ is the scaled relaxation frequency of oxygen and $F_{r,N}$ of nitrogen, which can be calculated with Equations D.2 and D.3. The absolute humidity (L) can be calculated from the relative humidity (L_r) with Equation D.4. The saturated vapour pressure (p_{sat}) within this formula can be calculated with Equation D.5 with $T_{01} = 273.16K$.

$$\alpha = \frac{20}{ln(10)} \frac{F^2 p_s}{p_{s0}} [1.84 \cdot 10^{-11} (\frac{T}{T_0})^{1/2} + (\frac{T}{T_0})^{-5/2} (0.01278 \frac{e^{-2239.1/T}}{F_{r,O} + F^2/F_{r,O}} + 0.1068 \frac{e^{-3352/T}}{F_{r,N} + F^2/F_{r,N}})] \tag{D.1}$$

$$F_{r,O} = \frac{1}{p_{s0}} (24 + 4.04 \cdot 10^4 L \frac{0.02 + L}{0.391 + L}) \tag{D.2}$$

$$F_{r,N} = \frac{1}{p_{s0}} (\frac{T_0}{T})^{1/2} (9 + 280 L \cdot e^{-4.17[(\frac{T_0}{T})^{1/3} - 1]}) \tag{D.3}$$

$$L = p_{s0} \frac{L_r}{p_s} \frac{p_{sat}}{p_{s0}} \tag{D.4}$$

$$p_{sat} = p_{s0} \cdot 10^{-6.8346 (T_{01}/T)^{1.261} + 4.6151} \tag{D.5}$$